DISSERTATION

SIMULATION OF NANOSCALE PATTERNS YIELDED BY ION BOMBARDMENT OF SOLID SURFACES

Submitted by

Daniel A. Pearson

Department of Physics

In partial fulfillment of the requirements

For the Degree of Doctor of Philosophy

Colorado State University

Fort Collins, Colorado

Spring 2018

Doctoral Committee:

Advisor: Mark Bradley

Kristen Buchanan
Martin Gelfand
Patrick Shipman

ABSTRACT

SIMULATION OF NANOSCALE PATTERNS YIELDED BY ION BOMBARDMENT OF SOLID SURFACES

This thesis includes numerical investigations into two topics of self-organized topographies produced on solid surfaces that are bombarded with a broad ion beam. The first topic is the formation of terraces. When a surface is bombarded at relatively large angles of incidence, the surface often develops facets that are characterized by large regions of nearly constant gradient in height, which are called terraces. The second topic is related to the observation that when the surface of a nominally flat binary material is bombarded with a broad, normally-incident ion beam, disordered hexagonal arrays of nanodots can form. Shipman and Bradley have derived equations of motion that govern the coupled dynamics of the height and composition of such a surface [P. D. Shipman and R. M. Bradley, *Phys. Rev. B* **84**, 085420 (2011)]. We investigate the influence of initial conditions on the hexagonal order yielded by integration of those equations of motion.

In our work on terrace formation, we introduce a model that includes an improved approximation to the sputter yield and that produces a terraced surface morphology at long times for a wide range of parameter values. Numerical integrations of our equation of motion reveal that the terraces coarsen for a finite amount of time after which the coarsening is interrupted, just as observed experimentally. We also show that the terrace propagation direction can reverse as the amplitude of the surface disturbance grows. This highlights the important role higher order nonlinearities play in determining the propagation velocity at high fluences. We study the nanoscale terraced topographies that arise when a solid surface is bombarded with a broad ion beam that has a relatively high angle of incidence θ. Our simulations establish that the surfaces exhibit interrupted coarsening, i.e., the characteristic width and height of the surface disturbance grow for a time but ultimately asymptote to finite values as the fully terraced state develops. In addition, as θ is reduced, the

surface can undergo a transition from a terraced morphology that changes little with time as it propagates over the surface to an unterraced state that appears to exhibit spatiotemporal chaos. For different ranges of the parameters, our equation of motion produces terraced topographies that are remarkably similar to those seen in various experiments, including pyramidal structures that are elongated along the projected beam direction and isolated lenticular depressions.

For our study of the influence of prepatterning surfaces governed by the Bradley-Shipman equations, the initial conditions studied are hexagonal and sinusoidal templates, straight scratches and nominally flat surfaces. Our simulations indicate that each of the prepatterned surfaces can lead to marked improvements in the hexagonal order compared to what is obtained from the nominally flat surfaces. For the hexagonal and sinusoidal templates with amplitude approximately equal to one hundredth of the amplitude of the pattern obtained at late times, the greatest improvement in order is obtained if the initial wavelength is approximately equal to or double the linearly selected wavelength. Our simulations of sinusoidal templates demonstrate that increasing the amplitude of the template can improve the effectiveness of templates with longer wavelengths. Scratches enhance the hexagonal order in their vicinity if their width is close to or less than the linearly selected wavelength. Our results suggest that prepatterning a binary material can dramatically increase the hexagonal order achieved at large ion fluences.

ACKNOWLEDGEMENTS

I would like to thank Leif Anderson, who created and supported the previous LaTeX template for a number of years. I also thank my advisor Mark Bradley and all my committee members for their guidance and support.

DEDICATION

I would like to dedicate this thesis to my loving family.

TABLE OF CONTENTS

ABSTRACT ii
ACKNOWLEDGEMENTS iv
DEDICATION v
LIST OF FIGURES viii
GLOSSARY OF ACRONYMS xiv
LIST OF PUBLICATIONS xv

Chapter 1 Introduction 1
1.1 Definitions and the Physical Situation 3
1.2 Ion Bombardment of Elemental Materials 5
1.2.1 Experimental Results 5
1.2.2 Theory – Elemental Materials 13
1.3 Ion Bombardment of Binary Materials 22
1.3.1 Experimental Results 23
1.3.2 Theory – Binary Materials 24
1.4 Analytical Background 27
1.4.1 Linear Stability Analysis 27
1.4.2 Shock Waves 28
1.5 Numerical Methods 29
1.5.1 Numerical Integration 30
1.5.2 Quantifying Pattern Order 34

Chapter 2 Theory of Terracing of Ion Bombarded Solid Surfaces 37
2.1 Equation of Motion 38
2.1.1 Nonlinear Coefficients 43
2.2 Numerical Methods 45
2.2.1 Determination of the Ripple Propagation Velocity 47
2.3 Terracing Simulation Results: 1+1 dimensions 49
2.4 Terrace Slope Selection 52
2.5 Terracing Results: 2+1 dimensions 60
2.5.1 Parallel-Mode Terraces 61
2.5.2 Steady-state solutions 62
2.5.3 Comparison with the predictions of the one-dimensional theory 66
2.5.4 Elongated pyramidal structures 68
2.5.5 Lenticular Depressions 72
2.6 Discussion 74
2.7 Conclusions 76

Chapter 3 Patterning Surfaces Before Ion Sputtering can Yield Nanodot Arrays with Improved Hexagonal Order 79
3.1 Equation of Motion and Initial Conditions 80

3.2 Results 82
3.2.1 Nominally Flat Initial Conditions 83
3.2.2 Hexagonal templates 84
3.2.3 Sinusoidal templates – low amplitude templates 87
3.2.4 Sinusoidal templates – larger amplitude templates 89
3.2.5 Scratch prepatterns 92
3.3 Conclusions 95

Chapter 4 Summary 96

LIST OF FIGURES

1.1 An initially nominally flat surface is exposed to a broad ion beam at oblique incidence. 4

1.2 Graphite surfaces subjected to 5 keV Xenon ion bombardment. Left column (a)-(c): ion fluence of 3×10^{17} $\mathrm{ions/cm^2}$; incidence angle θ equal to (a) 30^{o}, (b) 60^{o} and (c) 70^{o}. Right column (d)-(f): incidence angle of 60^{o}; ion fluence of (d) 5×10^{16} $\mathrm{ions/cm^2}$, (e) 2×10^{18} $\mathrm{ions/cm^2}$ and (f) 5×10^{18} $\mathrm{ions/cm^2}$. Arrows show the ion beam direction. The height scale varies between panels. This is a figure from Ref. [1]. 7

1.3 A carbon surface was bombarded with 20 keV Ga^+ ions at oblique incidence and parallel-mode ripples were formed. The sequence of snapshots shows the surface at increasing (from left to right) times. This figure is from Ref. [2]. 7

1.4 A cross-sectional TEM image of the surface shown in Figure 1.3. The bright white layer at the surface is material that has been amorphized. This figure is from Ref. [2]. . 8

1.5 This figure from Alkemade, Ref. [3], for (a)-(j) and (l) shows SEM images at increasing times of a glass surface bombarded by a broad beam of 30 keV $\mathrm{Ga^+}$ ions. The region boxed in a purple rectangle in (k) is the magnified region shown in the other figures. The fluence in (a) is 21×10^{20} $\mathrm{ions/m^2}$, and the fluence increases by 5.2×10^{20} $\mathrm{ions/m^2}$ in each consecutive image. The direction of the ion flux is to the right. The red vertical lines are guides to the eye for studying the surface propagation direction. The green line in (e) can be ignored. 9

1.6 An idealized terraced surface with selected slopes m_+ and m_-. The angle of incidence of the impinging ions is θ and the height of the surface above the $x-y$ plane is denoted by h. 11

1.7 A result from Ref. [2]. A cross-sectional TEM image of a surface obtained by bombarding carbon at a high angle of incidence with 20 keV gallium ions. The bright white layer at the surface is material that has been amorphized. The dark layer is amorphous platinum that was deposited prior to sectioning in order to increase contrast. The arrow shows the direction of the ion beam. 11

1.8 AFM images of a silicon surface bombarded by 0.5 keV argon ions at an angle of incidence of 72.5^{o}. A surface shown at different fluences, given in the top left of each panel, in units of $\mathrm{ions/cm^2}$. The surface formed parallel-mode ripples at early times, and evolved into a terraced structure at late times. The red arrow indicates the ion beam direction projected onto the surface. The insets are autocorrelations of the surface. Note that the scale is 200 nm in (a) and (b), and 400 nm in (c)-(f). This figure is from Basu *et al.* in Ref. [4]. 12

1.9 A molecular dynamics simulation of an ion impact on a solid surface causing several surface atoms to be sputtered. The color shows the ratio of the atoms' kinetic energy to the average thermal energy per atom at the melting point. One of these sputtered atoms can be seen at the top of the middle-left image. The simulation was done by Gnaser *et al.* in Ref. [5]. 13

1.10 A focused ion beam with flux **J** is incident upon the surface $h(x, y, t)$ at point $\mathbf{r}'$. In the Sigmund model of sputtering, maximal power is deposited at a point in the solid that is a distance a along the beam direction from $\mathbf{r}'$. The point of maximal power deposition is indicated by the red dot. The power deposited in the solid decreases as the parallel and perpendicular distances ($d_\parallel$ and $d_\perp$) increase, and the contours of equal power deposition are ellipsoidal. 15
1.11 (a) A SEM image of a surface of initially nominally flat GaSb that evolved into an array of nanodots with a high degree of local hexagonal order after normal-incidence ion bombardment. (b) The autocorrelation of the surface. These results were published in 1999 by Facsko *et al.* in Ref. [6]. 23
1.12 AFM images (scan size 3 mm) of Ar^+ sputtered InP surfaces ($E_{\rm ion} = 500$ eV, $j_{\rm ion} =$ 150 mA/cm^2 , $t = 1200$ s) at an incidence angle of $10^{\rm o}$ (a), $30^{\rm o}$ (b), $70^{\rm o}$ (c), and $80^{\rm o}$ (d). This figure and caption are from Ref. [7]. 24
1.13 The parameter space is partitioned into three different regions based on the linear stability analysis. This figure is from Ref. [8]. 26
1.14 This plot shows the linear growth rate's dependence on ripple wave number in region I of the parameter space shown in Fig. 1.13. If b is slightly less than the threshold value b_T, then there is a narrow band wave vectors that are linearly unstable. If b exceeds b_T, then every mode is linearly damped, and the nominally flat surface will flatten. This figure is from Ref. [8]. 26
1.15 **(a)** A section of the simulation result shown in Fig. 3.2 with blue dots indicating the nanodot peaks. **(b)** Around each peak, a circle of radius $p = 5$ has been drawn. **(c)** The connectivity parameter p has increased to 10.5 and red edges have been placed between the centers of circles that enclose each other's centers. Only the circles that enclose each other's centers are shown for clarity. **(d)** When $p = 11$, there are four filled in triangles where three circles all enclose each other's centers. Only the circles related to the filled in faces are shown. **(e)** When $p = 12.5$, many faces have been filled in and holes have emerged. The 8 white polygonal regions with red edge boundaries are identified as holes at this value of p. **(f)** A plot of $p_{\rm end}$ versus $p_{\rm start}$ for the holes found by our persistent homology analysis of (a). The green (red) squares are holes that are present (absent) in (e), and the blue diagonal is the line $p_{\rm end} = p_{\rm start}$. A square's vertical distance above the blue line is the corresponding hole's persistence interval length. 36

2.1 A plot of $c_3(\theta)/\max(c_3)$ versus the angle of incidence θ for bombardment of silicon with a 1 keV Ar^+ ion beam. 45
2.2 The Galerkin coefficient magnitude $|a_m|$ versus the coefficient index m for a simulation of the equation of motion (2.11) with $\gamma = 0.7$ at time $t = 1000$. The data point for $m = 0$ has been omitted. 48
2.3 Plots of u versus x at the equally spaced times shown, produced by integrating the equation of motion (2.11). The time for each curve is to the right of the plots. (a) $\gamma = 0.3$. (b) $\gamma = 0.7$. 49
2.4 The slope distribution (normalized counts versus u_x) for a simulation with $\gamma = 0.7$ at time $t = 1000$. 50

2.5 Surface width σ versus time t for (a) a simulation with γ=0.3 and (b) a simulation with $\gamma = 0.7$. The inset in (b) is plotted on a semilog scale to exhibit the exponential growth of σ at the early times. 51
2.6 The shooting method result transformed back to the untransformed problem for $\gamma = 0.7$ (red) is superimposed upon the result obtained by integrating the equation of motion (2.11) with $\gamma = 0.7$ (blue). The green dots are the fixed points of the equivalent system of ODEs (2.42) transformed back for $\gamma = 0.7$. 57
2.7 The terrace slopes ϕ_{+1} and ϕ_{-1} plotted versus γ. The red squares are the results obtained by integrating the equation of motion (2.11). The blue curves are the predicted slopes obtained from Eq. (2.47). 58
2.8 The downward drift rate μ plotted versus γ. The red squares are the results obtained by integrating the equation of motion (2.11). The blue curve is the prediction obtained from Eq. (2.45). 58
2.9 The propagation velocity s plotted versus γ. The red squares are the results obtained by integrating the equation of motion (2.11). The blue curve is the prediction obtained from Eq. (2.38). 59
2.10 The surface height obtained from a simulation of Eq. (2.2) at times (a) $t = 1000$, (b) $t = 3000$ and (c) $t = 5000$. By the end of the simulation, parallel-mode terraces have developed, with slight bends in the terrace edges due to the presence of a transverse instability. The parameter values used were $\kappa_1 = -0.5$, $\kappa_2 = -0.1$, $\lambda_1 = 0.5$, $\lambda_2 = 0.5$, $B = 1$, $\gamma_1 = 1$ and $\gamma_2 = 0$. 62
2.11 A sequence of snapshots of a silicon surface observed by Datta *et al.* The surface was bombarded 60 keV Ar^+ ions at a 60^o angle of incidence. The black arrows indicate the ion beam direction projected onto the surface. Terraces with relatively little transverse variation develop at late times. The surface coarsens laterally and roughens as the terraces form. This figure is from Ref. [9]. 63
2.12 The mean curvature of a surface obtained from a simulation of Eq. (2.2) at time $t = 3000$. The figure shown is the mean curvature of the surface seen in Figure 2.10 (b). . . 64
2.13 The gradient distribution of the surface obtained from a simulation of Eq. (2.2) at time $t = 3000$. The figure shown was obtained from the surface seen in Fig. 2.10 (b). 64
2.14 The gradient distributions of three surfaces obtained from a simulation of Eq. (2.2) integrated up to time $t = 750$ with the solutions to Eq. (2.56) plotted as red curves. The parameter values used in the simulations were (a) $\kappa_1 = -0.5$, $\kappa_2 = -0.5$, $\lambda_1 = -0.5$, $\lambda_2 = -0.5$, $B = 1$, $\gamma_1 = 1$ and $\gamma_2 = 0$; (b) $\kappa_1 = -0.5$, $\kappa_2 = 0.5$, $\lambda_1 = -0.5$, $\lambda_2 = -0.5$, $B = 1$, $\gamma_1 = 1$ and $\gamma_2 = 0$; (c) $\kappa_1 = -0.5$, $\kappa_2 = 0.5$, $\lambda_1 = -0.5$, $\lambda_2 = -0.5$, $B = 1$, $\gamma_1 = 1$ and $\gamma_2 = -1$. 65
2.15 A line scan along the x axis slice of a surface with transverse smoothing at time $t = 2000$. Note that the vertical scale has been enlarged by a factor of 40 to make the pattern easily discernible; the magnitude of the surface slope nowhere exceeds 0.1. The parameter values used were $\kappa_1 = -0.5$, $\kappa_2 = 1$, $\lambda_1 = -5$, $\lambda_2 = -5$, $B = 1$, $\gamma_1 = 100$ and $\gamma_2 = 0$. 66

2.16 (a) Downward drift speeds μ, (b) selected slopes $\phi_\pm$ and (c) propagation velocities s. The data points are values obtained from simulations of Eq. (2.2). The red curves are predictions from the 1D theory: (a) μ as given by Eq. (2.45), (b) $\phi_\pm$ as given by Eq. (2.47) and (c) s as given by Eq. (2.38). The surfaces were simulated to time $t = 500$ and the parameter values used were $\kappa_1 = -0.5$, $\kappa_2 = 10$, $\lambda_1 = -0.5$, $\lambda_2 = -0.5$ and $\gamma_2 = 0$. 67
2.17 The surface width σ versus time obtained from a simulation of Eq. (2.2). The figure shown is produced from the same simulation that yielded Fig. 2.10. 68
2.18 SEM images of a silicon surface produced by Carter in Ref. [10] by bombarding silicon with 40 keV argon ions at an angle of incidence of 70^{o}. The surface shown on the right is a magnification of the surface on the left. The red arrows indicate the ion beam direction projected onto the surface. There are elongated pyramidal structures that are protruding out of the surface and facing towards the beam. The ends of the structures appear to have a tendency to line up. 69
2.19 A surface obtained by integrating Eq. (2.2) up to time $t = 1800$, starting from a low amplitude white noise initial condition. The surface is still evolving at the time shown. At early times, perpendicular-mode ripples formed. Later, these ripples evolved into the elongated pyramidal structures seen in the figure. The parameter values used were $\kappa_1 = 0$, $\kappa_2 = -0.6$, $B = 1$, $\lambda_1 = 0.5$, $\lambda_2 = 0.5$, $\gamma_1 = 1$ and $\gamma_2 = -3$. 70
2.20 The gradient distribution of the surface obtained from a simulation of Eq. (2.2), integrated up to time $t = 1800$. The figure was obtained from the surface seen in Fig. 2.19. 70
2.21 The mean curvature H of the surface shown in Fig. 2.19. Shocks that are elongated in the longitudinal direction are evident. 71
2.22 AFM images that show the evolution of a germanium surface bombarded by 100 keV kryton ions at an angle of incidence of 60^{o}, obtained in an experiment by Datta *et al*. The height scales are (d) 20.7 nm, (e) 315.7 nm, and (f) 2 nm. The top left of each image shows the 2D autocorrelations of the surface. The top right shows its 2D slope distributions. The direction of the incident beam projected onto the surface was from right to left, and so the ripples in the leftmost image are parallel-mode ripples. This figure is from Ref. [11]. 71
2.23 (a) A surface obtained by integrating Eq. (2.2) up to time $t = 150$, starting from a low amplitude white noise initial condition. Parallel-mode ripples are evident. (b) At time $t = 850$, the surface exhibits elongated pyramidal structures. The parameter values used in this simulation were $\kappa_1 = -0.5$, $\kappa_2 = -0.3$, $B = 1$, $\lambda_1 = -0.05$, $\lambda_2 = -0.5$, $\gamma_1 = 1$ and $\gamma_2 = -3$. 72
2.24 A silicon surface obtained in an experiment by Teichmann *et al.* after bombarding it with 1.2 keV xenons ions at an angle of incidence of 75^{o}. The value of z indicates the difference between the maximum and minimum values of the surface height. The darker color indicates lower surface heights. The ion fluence was 1.35×10^{19} ions/cm^2. The arrow indicates the direction of the ion beam projected onto the surface. This figure is from Ref. [12]. 73

2.25 (a) A surface obtained by integrating Eq. (2.2) up to time $t = 465$, starting from a low amplitude spatial white noise initial condition. A lenticular depression is shown, surrounded by a region of the surface that looks very much like what would be seen in simulations of the isotropic KS equation. (b) The mean curvature H of the surface in (a). The parameters were $\kappa_1 = -0.5$, $\kappa_2 = -0.5$, $B = 1$, $\lambda_1 = -0.5$, $\lambda_2 = -0.5$, $\gamma_1 = 0.11$ and $\gamma_2 = 0$. 73
2.26 An initial circular pit is etched and is shown in (a). After bombarding at normal incidence, the pit radius has increased but the slopes of the pit walls are unchanged, seen in (b). This experiment was carried out by Chen *et al.* , see Ref. [13]. 76

3.1 The height (left) and the magnitude of the Fourier transform (right) of a non-templated surface after integrating to time $t = 10^4$. White coloring indicates larger values and the black coloring indicates smaller values. 83
3.2 The height (left) and the magnitude of the Fourier transform (right) of a non-templated surface after integrating to time $t = 10^4$. 84
3.3 The height (left) and the magnitude of the Fourier transform (right) of a hexagonally templated surface after integrating to time $t = 10^4$. The initial wavelength was $\lambda_1 = 20 \simeq 2\lambda_T$. Typical patterns that form in experiments have dots that are about 50 nm in diameter; this template has height variations that would need to be about 100 nm in diameter for an ion beam experiment. 85
3.4 The height (left) and the magnitude of the Fourier transform (right) of a hexagonally templated surface after integrating to time $t = 10^4$. The initial wavelength was $\lambda_1 = 400/38 \simeq \lambda_T$. 85
3.5 The height (left) and the magnitude of the Fourier transform (right) of a hexagonally templated surface after integrating to time $t = 10^4$. The surface is very slowly evolving at the time shown. The initial wavelength was $\lambda_1 = 400/18 \simeq 22.2$. 86
3.6 The H_1 sum versus the ratio k_1/k_T for the hexagonal templates after integrating to time $t = 10^4$, averaged over 10 realizations. The two horizontal blue lines show the H_1 sum averaged over 10 non-templated initial surfaces after integrating to time $t = 10^4$, plus or minus the standard deviation. 87
3.7 The mean of the nearest-neighbor distribution $\Lambda(n)$ versus the ratio k_1/k_T for the hexagonal templates after integrating to time $t = 10^4$, averaged over 10 realizations. The two horizontal blue lines show the mean of $\Lambda(n)$ averaged over 10 non-templated initial surfaces after integrating to time $t = 10^4$, plus or minus the standard deviation. . 88
3.8 The variance of the nearest-neighbor distribution $\Lambda(n)$ versus the ratio k_1/k_T for the hexagonal templates after integrating to time $t = 10^4$, averaged over 10 realizations. The two horizontal blue lines show the variance of $\Lambda(n)$ averaged over 10 non-templated initial surfaces after integrating to time $t = 10^4$, plus or minus the standard deviation. 88
3.9 The surface height (left) and the magnitude of the Fourier transform (right) after integrating to time $t = 10^4$ for a sinusoidal template with $A_0 = 10^{-2}$ and $\lambda_2 = 20 \simeq 2\lambda_T$. . 89
3.10 The surface height (left) and the magnitude of the Fourier transform (right) after integrating to time $t = 10^4$ for a sinusoidal template with $A_0 = 10^{-2}$ and $\lambda_2 = 400/39 \simeq \lambda_T$. 90

3.11 The H_1 sum versus the ratio k_1/k_T for the sinusoidal templates with $A_0 = 10^{-2}$ after integrating to time $t = 10^4$, averaged over 150 realizations. The data point at $k_1/k_T = 0$ is from simulations with no templating. 90
3.12 The surface obtained after integrating to time $t = 10^4$ for a sinusoidal template with $A_0 = 1$ and $\lambda_2 = 40 \simeq 4\lambda_T$. 91
3.13 The variance of the nearest-neighbor distribution $\Lambda(n)$ versus the template amplitude A_0 for sinusoidal templates with $\lambda_2 \simeq 4\lambda_T$ after integrating to time $t = 10^4$, averaged over 10 realizations. 91
3.14 Surface height (left) and the magnitude of the Fourier transform (right) after integrating to time $t = 10^4$ with a scratch along $x = 0$ of width $2\sigma = 4$. 92
3.15 Surface height (left) and the magnitude of the Fourier transform (right) after integrating to time $t = 10^4$ with a scratch of width $2\sigma \simeq 13.86$. 93
3.16 Surface height (left) and the magnitude of the Fourier transform (right) after integrating to time $t = 10^4$ with a scratch of width $2\sigma \simeq 20.40$. 94
3.17 The H_1 sum per unit area versus strip width for the initial conditions with a scratch of width 4 (left) and with a scratch of width approximately $2\lambda_T$ (right) after integrating to time $t = 10^4$, averaged over 10 realizations. 94

GLOSSARY OF ACRONYMS

AFM: Atomic Force Microscope

AKS: Anisotropic Kuramoto-Sivashinsky

BH: Bradley-Harper

BS: Bradley-Shipman

c.c.: Complex Conjugate

CV: Carter-Vishnaykov

EOM: Equation Of Motion

eKS: Extended Kuramoto-Sivashinsky

ETD: Exponential Time Differencing

ETDRK4: Exponential Time Differencing with Fourth-order Runge-Kutta

HB: Harrison-Bradley

KS: Kuramoto-Sivashinsky

NND: Nearest-Neighbor Distribution

ODE: Ordinary Differential Equation

PDE: Partial Differential Equation

PB: Pearson-Bradley

RK: Runge-Kutta

RK1: First-order Runge-Kutta

RK4: Fourth-order Runge-Kutta

SEM: Scanning Electron Microscope

TEM: Transition Electron Microscopy

LIST OF PUBLICATIONS

D. A. Pearson and R. M. Bradley, "Theory of Terraced Topographies Produced by Oblique-Incidence Ion Bombardment of Solid Surfaces," *J. Phys.: Cond. Matt.* **27**, 015010 (2015). https://doi.org/10.1088/0953-8984/27/1/015010

D. A. Pearson, R. M. Bradley, F. C. Motta and P. D. Shipman, "Patterning Surfaces Before Ion Sputtering Can Yield Nanodot Arrays with Improved Hexagonal Order," *Phys. Rev. E* **92**, 062401 (2015). https://doi.org/10.1103/PhysRevE.92.062401

T. Basu, D. A. Pearson, R. M. Bradley and T. Som, "Temporal evolution of a silicon surface subject to low energy ion irradiation and concurrent sample rotation," *Applied Surface Science* **379**, 480-488 (2016). https://doi.org/10.1016/j.apsusc.2016.03.136

C. Strickland, D. A. Pearson and P. D. Shipman, "Formation of square lattices in coupled pattern-forming systems," *Biomath* **5** (2), 1612181 (2017).
http://dx.doi.org/10.11145/j.biomath.2016.12.181

M. P. Harrison, D. A. Pearson and R. M. Bradley, "Emergence and detailed structure of terraced surfaces produced by oblique-incidence ion sputtering," *Phys. Rev. E* **96**, 032804 (2017). https://doi.org/10.1103/PhysRevE.96.032804

F. C. Motta, R. Neville, P. D. Shipman, D. A. Pearson and R. Mark Bradley "Measures of Order for Nearly Hexagonal Lattices" (in review at Physica D)

Chapter 1

Introduction

When a surface is exposed to a broad ion beam of sufficient energy, it will erode due to a process called sputtering. An atom (or atoms) on the target surface is said to be sputtered when it is ejected from the surface due to the incident ions. The rate of erosion induced by sputtering is not uniform across the surface. In particular, the local erosion rate depends on the surface's slope, curvature, and higher spatial derivatives. The dependence of the erosion rate on the surface curvature can cause a flat surface to be unstable. When there is an instability, often the surface roughens without forming patterns – for example, the surface can form disordered mounds and depressions. However, it is possible for a variety of self-assembled nanoscale patterns to emerge. Examples include periodic height modulations or "ripples" [14] as well as nanodots arranged in hexagonal arrays of surprising regularity [6, 8, 15, 16]. This thesis primarily focuses on the study of the formation of facets, which we call terraces, and the control of hexagonal arrays of nanodots.

Apart from being interesting, ion bombardment has the potential to become a high-throughput, single-step method of mass producing large-area nanostructures with length scales beyond the limits of conventional optical lithography. In this introduction, we will focus on the potential applications that are the most relevant to the work that we discuss in this thesis. The first application we discuss is based on terrace formation. Harrison and Bradley (HB) have advanced a two-stage procedure for producing high efficiency blazed diffraction gratings that utilizes the facets that develop from bombardment with a broad ion beam at a relatively high angle of incidence [17]. In the first stage of their proposed fabrication method, conventional lithography is used to produce a periodic height modulation on the surface of the sample. The second stage consists of bombarding this prepatterned surface with a broad ion beam of noble gas ions at a high angle of incidence. HB's simulations strongly suggest that this serves to transform the initial pattern into the periodic sawtooth form characteristic of high quality blazed gratings if the ion beam and target material are selected appropriately. More recently, they have recently expanded upon this method by alternating

between a stage with concurrent deposition and ion bombardment and a stage with only deposition, leading to the formation of a multilayer blazed diffraction grating [18]. These multilayer blazed gratings could perform well in the extreme ultraviolet and soft X-ray regimes [18]. Additionally, Ou *et al.* have actually made blazed gratings using ion bombardment, using a different method that does not involve prepatterning the surface [19].

Another application is motivated by the experimental observation that it is possible for a hexagonally-ordered array of nanodots to form when a binary material is bombarded at normal incidence. According to the Bradley-Shipman (BS) model of this phenomenon, one of the atomic species will be concentrated preferentially on top of the nanodots, and the other in the depressions between them [8, 15, 16]. If the two atomic species have different magnetic properties and the order of the array is sufficient, the surface could be used for magnetic data storage. However, the degree of hexagonal order reached in these experiments typically is not sufficiently strong for this application; this motivated our group to seek a method to improve the quality of order, and our proposed method is discussed in this thesis. An experimental method that uses ion bombardment to produce an ordered array of magnetic nanodots was explored in [20, 21]. In these experiments, a magnetic film was embedded in a GaSb film so that the magnetic film was parallel to the surface. The GaSb surface was eroded by ion bombardment until the surface was part way through the magnetic film. Furthermore, Facsko *et al.* have produced hexagonal arrays of semiconductor quantum dots on GaSb by normal incidence ion bombardment [6].

This thesis is organized as follows. Background material is introduced in the remainder of this chapter, which is subdivided into the following sections. We begin in Section 1.1 with a basic overview of a typical ion bombardment experiment, so that we can define terms and the coordinate system that we use to describe the physical situation. In Section 1.2, we explore experiments and theory for elemental materials bombarded by a broad ion beam. This includes a discussion of the linear Bradley-Harper (BH) theory, which is essential for understanding the onset of pattern formation, and then the Kuramoto-Sivashinsky (KS) equation is discussed. The KS equation is obtained by including the lowest order nonlinear terms in the linear BH theory. These nonlinear

terms control the exponential growth of the linearly unstable modes. Next, in Section 1.3, experiments on binary materials that produce nanodots arranged in a hexagonal array are introduced, along with the Bradley-Shipman theory, which can explain the formation of said hexagonal arrays of nanodots. We review linear stability analysis and shock waves in Section 1.4. In Section 1.5, we discuss some standard numerical approaches to integration of differential equations and quantifying pattern order, which concludes the background introductory material. We then present our theory of terrace formation in Chapter 2, which is modeled by an equation of motion that includes cubic nonlinearities in addition to the usual KS quadratic nonlinear terms. In Chapter 3, we present our work demonstrating that according to the BS theory, the degree of order of the hexagonal nanodot arrays can be improved by appropriately prepatterning the surface. Finally, in Chapter 4, we wrap up with a summary of the main conclusions of this thesis.

1.1 Definitions and the Physical Situation

In the experiments that we consider, a solid surface that is bombarded by a broad ion beam. Typically, the solid surface is initially flat, but there have been experiments in which prepatterned samples were used as well; in this section, we focus on the case in which the target material's surface is initially flat. The ion beams are often comprised of noble gas ions, since they have low chemical reactivity. Let the $x-y$ plane be set to coincide the unperturbed initial flat surface; the z axis is perpendicular to the unperturbed surface (see Fig. 1.1). The surface will be represented by a height function $h = h(x, y, t)$, *i.e.*, its height above each point in the $x-y$ plane. Furthermore, in the experiments we consider in this thesis, the crystal structure near the surface of the solid is continually disrupted by the ion bombardment. Since the surfaces are amorphous, the symmetries of the surface topographies that form are dictated by the direction of the ion beam, not the crystalline structure of the bulk material. If the ion beam is normally incident on the surface, there is azimuthal symmetry. However, if the ion beam is obliquely incident on the surface, the azimuthal symmetry is broken. In this case, we will choose the positive x direction to point antiparallel to the direction of the ion beam projected onto the $x-y$ plane. Thus, the x direction will be called the

longitudinal direction, and the y direction will be called the transverse direction. In this thesis, we will only consider stationary surfaces. We define $\nabla \equiv \hat{\mathbf{x}}\frac{\partial}{\partial x} + \hat{\mathbf{y}}\frac{\partial}{\partial y}$ and use this notation throughout this thesis. Let $\hat{\mathbf{e}}$ be the unit vector whose direction is opposite of the ion flux direction. The angle between $\hat{\mathbf{e}}$ and $\hat{\mathbf{z}}$ is defined to be the angle of incidence, which we denote by θ. If the ion beam is normally incident, then $\theta = 0$. If θ is nonzero, then the angle of incidence is oblique; a near grazing angle of incidence corresponds to θ near $\pm 90^{\circ}$. Note that θ differs from the local angle of incidence, which is the angle between $\hat{\mathbf{e}}$ and $\hat{\mathbf{n}}$, where $\hat{\mathbf{n}}$ is the position-dependent unit surface normal vector. A depiction of an initially nominally flat surface that is exposed to a broad ion beam at an oblique angle of incidence is shown in Fig. 1.1 along with the coordinate system described in this paragraph. When ripples form in experiments, their wave vector is typically either mostly

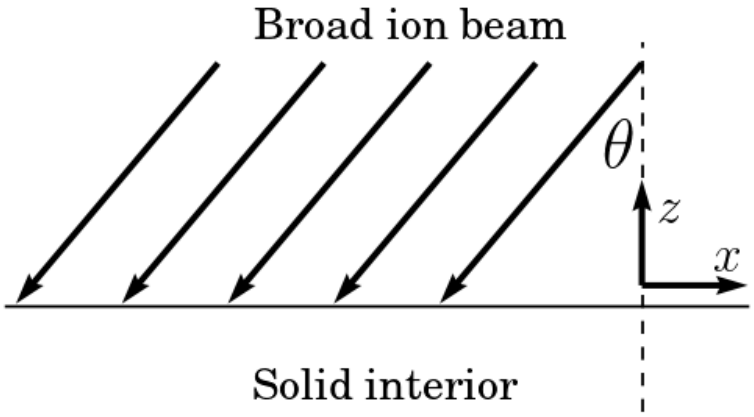

Figure 1.1: An initially nominally flat surface is exposed to a broad ion beam at oblique incidence.

parallel or perpendicular to the ion beam direction projected onto the solid surface. We distinguish between these two orientations by referring to them as parallel mode and perpendicular-mode ripples, respectively.

In analysis of ion bombarded surfaces, it is often advantageous to consider the dynamics of a surface that depends on only one spatial variable and one time variable; that is $h = h(x, t)$. We will refer to such a system as 1+1 dimensional, in contrast to a system in 2+1 dimensions in which $h = h(x, y, t)$. A 1+1 dimensional equation of motion can still make accurate predictions for

a surface in 2+1 dimensions if there is sufficient smoothing in the transverse direction. We will demonstrate this in the context of terrace formation in Section 2.

1.2 Ion Bombardment of Elemental Materials

This section begins with various experimental results on ion bombardment of elemental materials, which can lead to the formation of ripple patterns and terraces. Then we presents key aspects of the Sigmund model of sputtering, followed by an overview of how Bradley and Harper used the Sigmund model of sputtering to explain the formation of the ripples seen in experiments. We will also discuss the Carter-Vishnaykov (CV) effect, which can lead to smoothing at small angles of incidence and to ripple pattern formation at sufficiently large angles of incidence. Next, we introduce the Kuramoto-Sivashinsky equation, which is obtained by adding the lowest order nonlinearities to the linear BH theory. Finally, we discuss an extension of the Kuramoto-Sivashinsky equation that can yield hexagonally ordered arrays of nanodots, for appropriately chosen parameter values.

1.2.1 Experimental Results

Often, exposing a nominally flat solid surface of an elemental material to a broad ion beam simply causes it to flatten further [22]. This can be useful in some situations, but it is not the focus of this work. We will focus on situations in which the initial nominally flat surface is unstable.

Ripples

Ripples are the most common nanoscale patterns seen on solid surfaces that are ion bombarded at oblique angles of incidence. Observations of ripple formation date back to 1962 [23]. Figure 1.2 shows surfaces produced by 5 keV Xenon ion bombardment of highly oriented graphite surfaces at different angles of incidence and ion fluences; these experiments were carried out by Habenicht *et al.* in 1999 [1]. The black arrow in the figure shows the direction of the ion beam projected onto the surface. For the $\theta = 30^{\circ}$ and $\theta = 60^{\circ}$ cases, Habenicht *et al.* observed parallel-mode ripples. At the larger angle of incidence $\theta = 70^{\circ}$, however, they observed perpendicular-mode ripples. This switch of selected ripple orientation can be understood within the BH theory, which is discussed in

Section 1.2.2. Another experimental result showing parallel-mode ripples is in Figure 1.3, which is a result from Adams *et al.* in 2002 [2]. In their experiment, Adams *et al.* bombarded a carbon surface with 20 keV Ga^+ ions. Time increases from left to right in the sequence of images. The white arrow in the figure is the ion beam direction projected onto the surface. An important feature in the right-most image is that at multiple places in the pattern, ripple crests terminate and the ripple troughs merge together. These structures are a type of defect called dislocations. Defects and disorder are commonplace in patterns produced by ion bombardment, and are the main obstacles to most applications. Figure 1.4 shows a cross-section with $y = \text{const}$ of a surface that is similar to the right-most image shown in Figure 1.3. The bright white layer of material that is concentrated at the surface has been amorphized by the incident ions. This demonstrates that the underlying crystal structure did not play a significant role in the formation of the ripples.

In our discussion of Bradley-Harper theory in Section 1.2.2, we will see that the linear theory predicts that if parallel-mode ripples develop, then they propagate in the direction opposite to the incoming ions; that is, they propagate towards the beam source. Alkemade tested this aspect of BH theory by bombarding a SiO_2 surface with a broad beam of 30 keV gallium ions; his result from Ref. [3] is shown in Fig. 1.5. The direction of the ion beam flux projected onto the surface is to the right. In the first few panels, the ripples are still forming, and it is difficult to discern any propagation of the ripples. In the last few panels, however, there is a distinct propagation to the right. This means the ripples propagated away from the beam source, i.e., opposite the direction that was predicted by the linear BH theory. We believe that the apparent discrepancy is not due to a flaw in linear BH theory, but rather that the surface is no longer in the linear regime in snapshots shown in those panels. Indeed, the surface topography in those panels exhibits step-like faceted structures that we call terraces. In the section on our theory of terracing, it is demonstrated that nonlinear effects can cause the observed propagation direction to be the opposite of that predicted by linear BH theory. More experimentally produced terraced structures are shown in the next section.

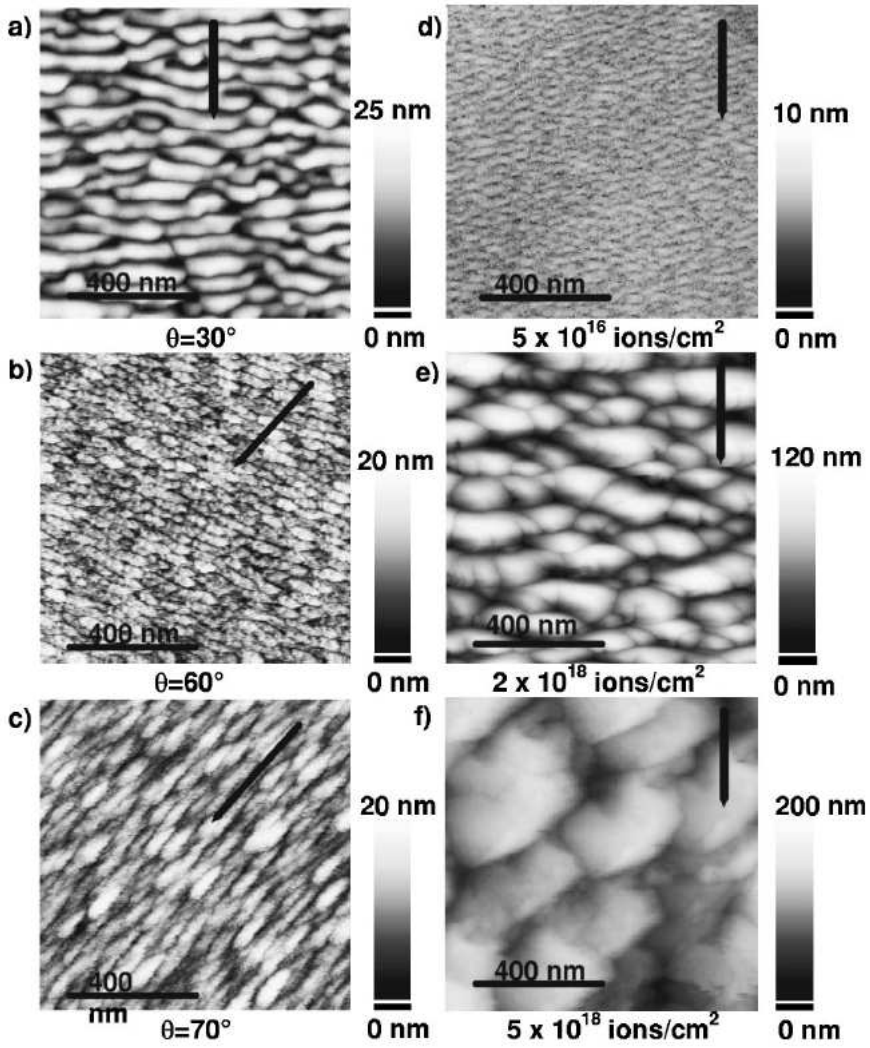

Figure 1.2: Graphite surfaces subjected to 5 keV Xenon ion bombardment. Left column (a)-(c): ion fluence of 3×10^{17} ions/cm^2; incidence angle θ equal to (a) 30°, (b) 60° and (c) 70°. Right column (d)-(f): incidence angle of 60°; ion fluence of (d) 5×10^{16} ions/cm^2, (e) 2×10^{18} ions/cm^2 and (f) 5×10^{18} ions/cm^2. Arrows show the ion beam direction. The height scale varies between panels. This is a figure from Ref. [1].

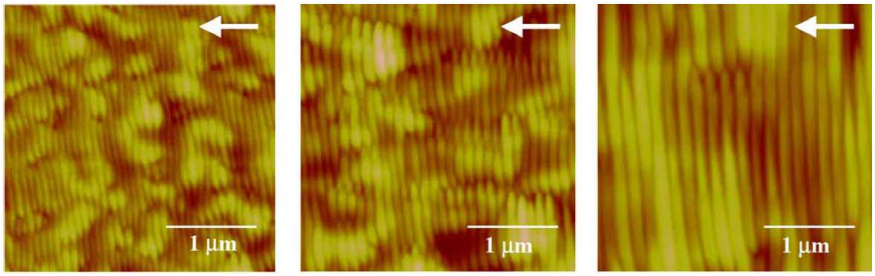

Figure 1.3: A carbon surface was bombarded with 20 keV Ga^+ ions at oblique incidence and parallel-mode ripples were formed. The sequence of snapshots shows the surface at increasing (from left to right) times. This figure is from Ref. [2].

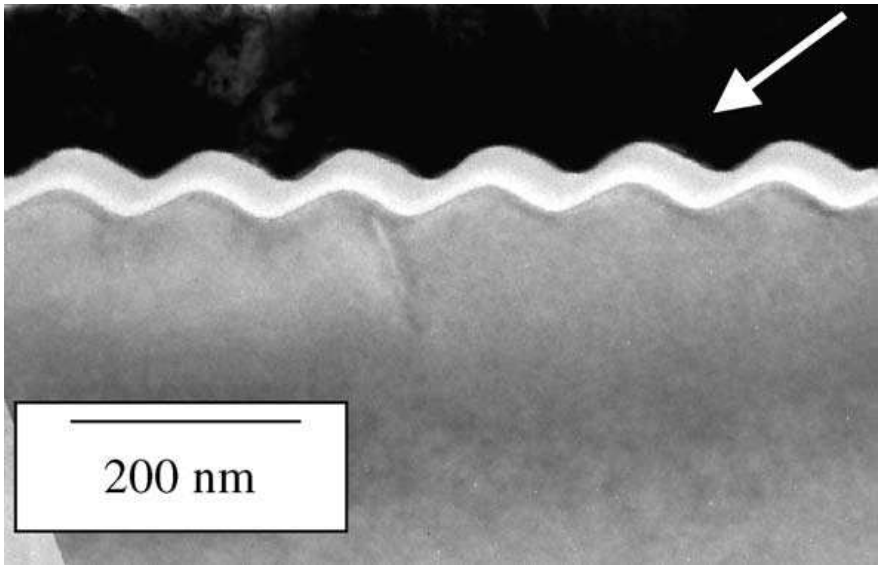

Figure 1.4: A cross-sectional TEM image of the surface shown in Figure 1.3. The bright white layer at the surface is material that has been amorphized. This figure is from Ref. [2].

Terraces

In the last section, it was shown that when a nominally flat solid surface is bombarded with a broad ion beam at oblique incidence, nanoscale ripples often develop on the surface. It is frequently observed in experiments that at the late stages of its time evolution, the surface develops a terraced form [2, 4, 9, 10, 24–31]. We now clarify the meaning of a terraced surface. A height profile of a terraced surface taken along the projected ion direction is not sinusoidal (see Figure 1.6). Instead, as we trace along the height profile, the surface slope is nearly equal to a constant value m_+ for a long spatial interval. At some point, the slope changes rapidly, and then is nearly equal to a constant negative value m_- for a long interval. The slope once again changes rapidly at some point, and then is approximately equal to m_+. The height profile continues in this fashion, and so takes on an irregular sawtooth form. The two sides of a "tooth" have the slopes m_+ and m_-. These slopes have different magnitudes, and so the teeth are asymmetric.

Images of terraced surfaces formed in experiments can be seen in Figs. 1.7 and 1.8. The surface in Fig. 1.7 was obtained by Adams *et al.* by bombarding carbon at a large angle of incidence by 20 keV gallium ions, and shows the asymmetric sawtooth shape of the surface in the xz cross section [2]. The images shown in Fig. 1.8 were produced by Basu *et al.* by exposing a silicon surface

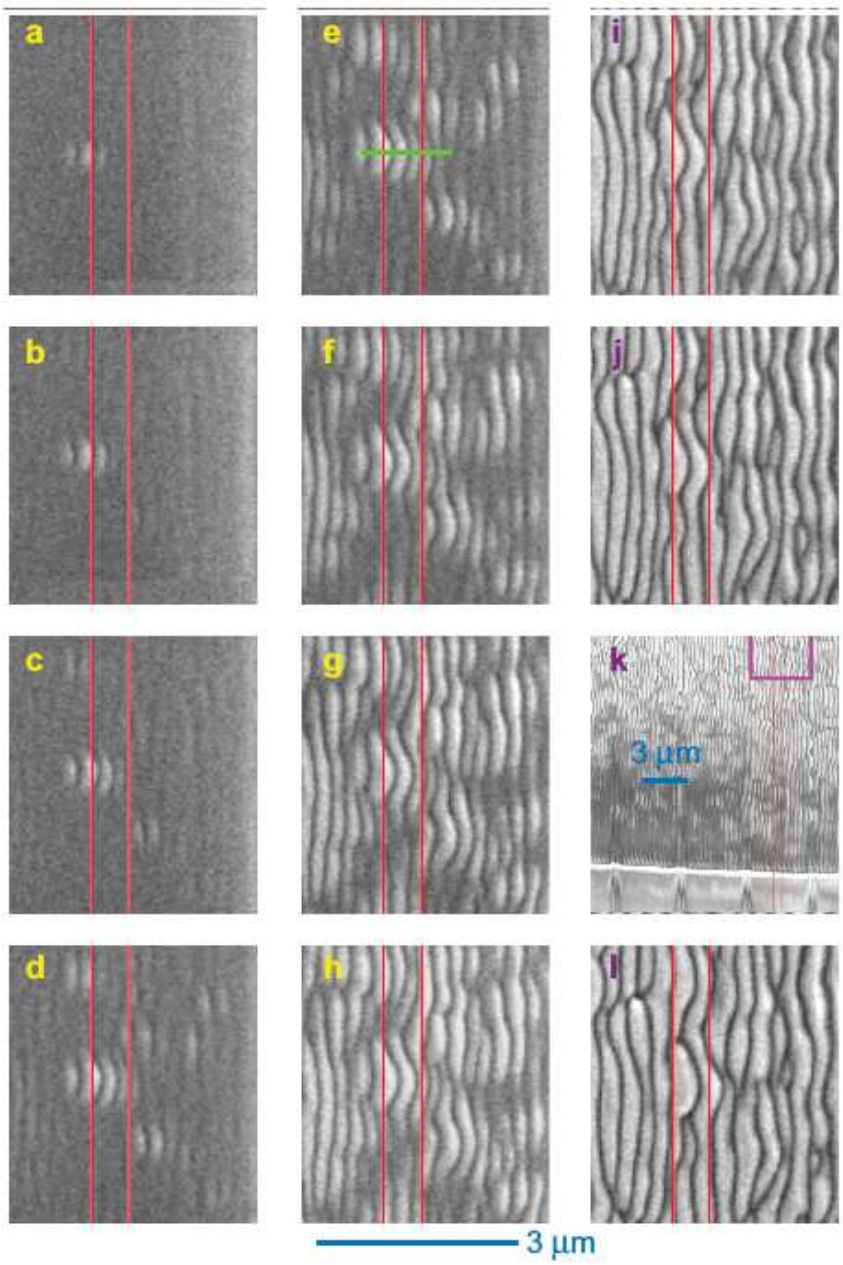

Figure 1.5: This figure from Alkemade, Ref. [3], for (a)-(j) and (l) shows SEM images at increasing times of a glass surface bombarded by a broad beam of 30 keV Ga^+ ions. The region boxed in a purple rectangle in (k) is the magnified region shown in the other figures. The fluence in (a) is 21×10^{20} ions/m^2, and the fluence increases by 5.2×10^{20} ions/m^2 in each consecutive image. The direction of the ion flux is to the right. The red vertical lines are guides to the eye for studying the surface propagation direction. The green line in (e) can be ignored.

bombarded by 0.5 keV argon ions at an angle of incidence of 72.5$^{\rm o}$ [4]. The numbers in the top left indicate the ion fluence in units of ions/cm^2, and the insets are autocorrelations of the surface. The surface forms parallel-mode ripples at early times and then develops terraces at late times. Terraces form most commonly when the ion beam is close to grazing incidence; however, they have been observed even when the angle of incidence has been as small as $\theta = 45^{\rm o}$ [10, 27]. For example, Wei *et al.* demonstrated this in their experiment in which they bombarded pyrochlore with 30 keV Ga^+ ions. In their experiments, the terraces had one side perpendicular to the ion beam and the other parallel to it. This phenomenon has been observed in multiple experiments in which terraces were formed by ion bombardment. Another experiment exhibiting terraces with one side perpendicular to the ion beam and other other parallel was carried out by Adams *et al.* [2]. They bombarded carbon with 20 keV Ga^+ ions over a range of incidence angles $\theta = 0 - 80^{\rm o}$. They found that the terraces formed for sufficiently high angles of incidence, specifically $\theta > 70^{\rm o}$. However, there are also experiments in which the terraces do not have one side perpendicular and the other side parallel to the ion beam. An example of this is Vollner *et al.'s* experimental work. They exposed fused silica surfaces with ripple prepatterns to 2 keV Ar^+ ions. The terraced surfaces that formed had local ion incidence angle distributions that were not peaked at $0^{\rm o}$ and $90^{\rm o}$. Vollner *et al.* showed that, in their experiment, sputtering was the dominant physical mechanism. Later we will discuss the theory Pearson and Bradley introduced that yields terrace formation [32]; this theory is consistent with the observation that sputtering can lead to terrace formation in experiments carried out at high angles of incidence.

If the target is crystalline and remains so when it is bombarded, the faces of the terraces may coincide with low index crystal facets. Under these circumstances, at least part of the driving force for terrace formation must come from the tendency to minimize the surface free energy. Terraced surfaces can develop, however, on the surfaces of amorphous materials or on materials with a surface layer that has been amorphorized by ion bombardment [2, 4, 9, 10, 25, 26, 29–31]. In these cases, the appearance of a terraced ripple structure at the late stages of ion erosion cannot be attributed to surface faceting. Moreover, the anisotropic KS equation does not yield terraced

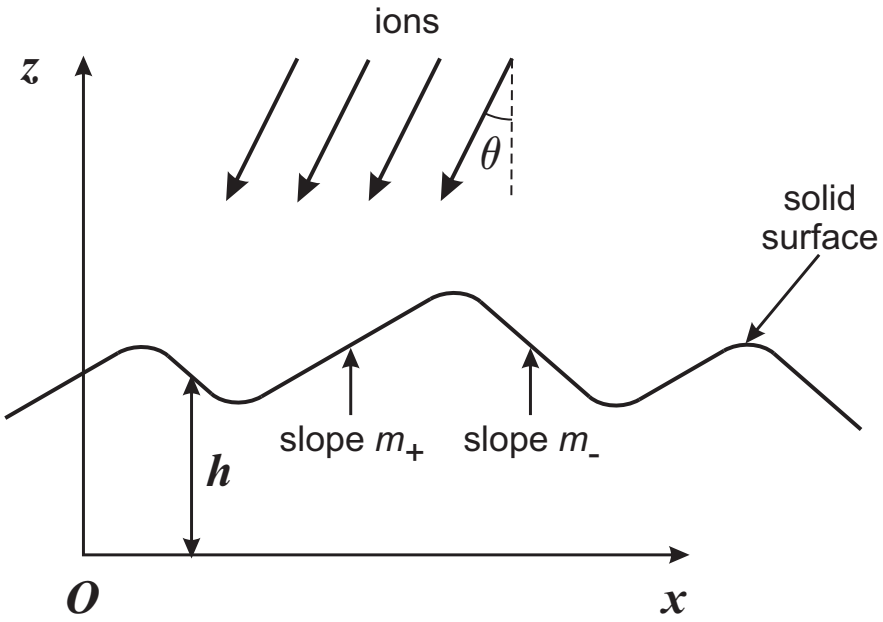

Figure 1.6: An idealized terraced surface with selected slopes m_+ and m_-. The angle of incidence of the impinging ions is θ and the height of the surface above the $x - y$ plane is denoted by h.

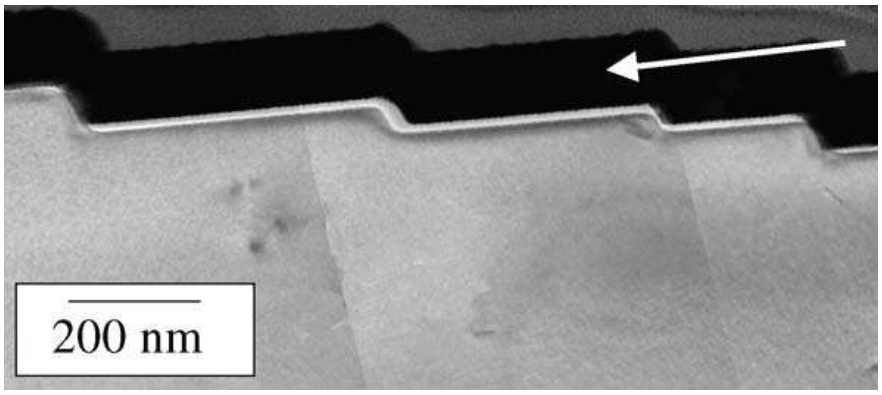

Figure 1.7: A result from Ref. [2]. A cross-sectional TEM image of a surface obtained by bombarding carbon at a high angle of incidence with 20 keV gallium ions. The bright white layer at the surface is material that has been amorphized. The dark layer is amorphous platinum that was deposited prior to sectioning in order to increase contrast. The arrow shows the direction of the ion beam.

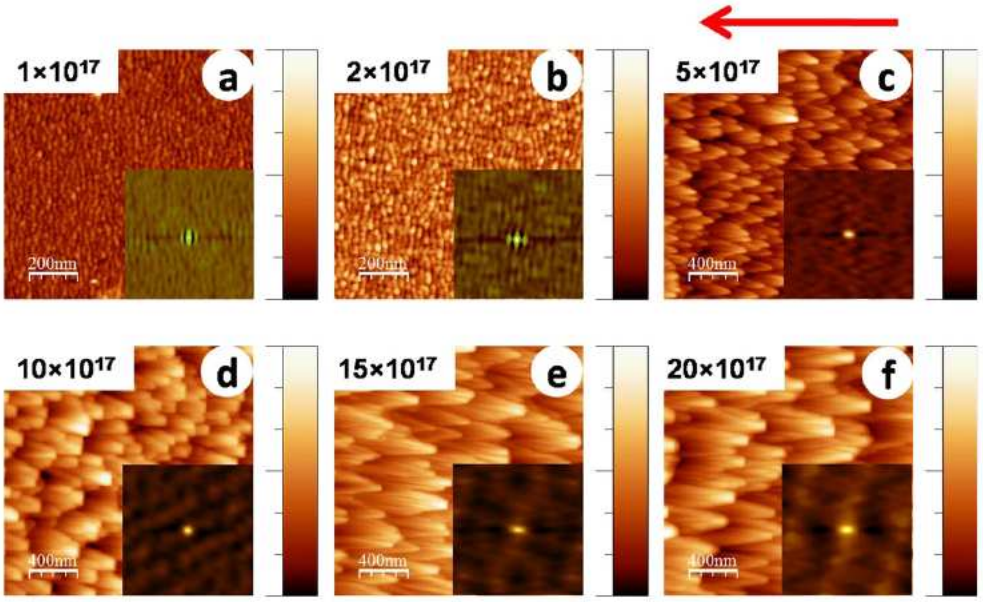

Figure 1.8: AFM images of a silicon surface bombarded by 0.5 keV argon ions at an angle of incidence of 72.5°. A surface shown at different fluences, given in the top left of each panel, in units of $\mathrm{ions/cm^2}$. The surface formed parallel-mode ripples at early times, and evolved into a terraced structure at late times. The red arrow indicates the ion beam direction projected onto the surface. The insets are autocorrelations of the surface. Note that the scale is 200 nm in (a) and (b), and 400 nm in (c)-(f). This figure is from Basu *et al.* in Ref. [4].

surfaces. Two questions therefore present themselves: Why do terraced topographies form when the surface of the target is not crystalline? How are the slopes m_+ and m_- selected by the system?

In this thesis, we will study an equation of motion for the surface of an ion-bombarded elemental material that differs from the usual KS equation by the inclusion of a cubic nonlinearity. Our results establish that this term has a crucial influence on the dynamics — it can lead to the formation of a terraced topography that coarsens with time, in accord with experimental observations [2, 4, 9, 25–31]. The rapid variation in the slope in a spatial region connecting the selected slopes is due to the formation of a so-called undercompressive shock. Finally, we show that the cubic nonlinearity can lead to a reversal of the ripple propagation velocity as the ripple amplitude grows. This could explain why the ripples were observed to move in the direction opposite to that predicted by the linear Bradley-Harper theory in most experiments [3, 5, 27, 33–36].

1.2.2 Theory – Elemental Materials

Sigmund Theory of Sputtering

When an ion is incident on a solid, the ion itself can strike an atom at the surface and so eject it from the solid. However, the process that leads to an atom (or atoms) sputtering off the surface can be more complicated. With sufficient energy, the incident ion can penetrate some distance into the solid and collide with interior atoms that then recoil. Those recoiling atoms can then strike other atoms, and the process repeats resulting in a collision cascade. Meanwhile the ion continues to strike additional atoms. Ultimately one or more of the atoms in the collision cascade may strike atoms at the surface with sufficient energy to eject them from the surface. This complicated process can be simulated using molecular dynamics. A sequence of images obtained from a molecular dynamics simulation of an ion striking a solid surface that was computed by Gnaser *et al.* is shown in Fig. 1.9 [5].

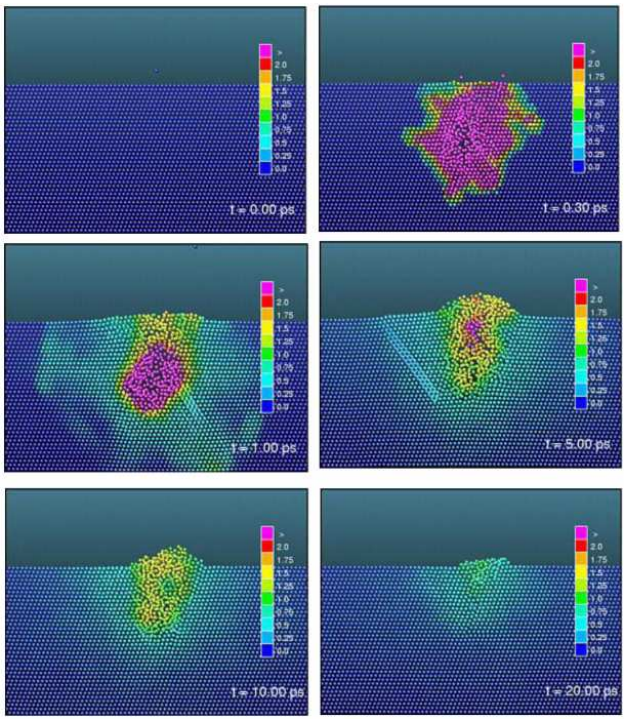

Figure 1.9: A molecular dynamics simulation of an ion impact on a solid surface causing several surface atoms to be sputtered. The color shows the ratio of the atoms' kinetic energy to the average thermal energy per atom at the melting point. One of these sputtered atoms can be seen at the top of the middle-left image. The simulation was done by Gnaser *et al.* in Ref. [5].

When there is a sufficiently large flux of ions striking the surface, the detailed process by which the sputtering occurs is not needed to obtain good statistical approximations to the physics of sputtering. This idea is used in the Sigmund model of sputtering. In the Sigmund model, the ion flux striking the surface at position $\mathbf{r}'$ (see Figure 1.10) deposits maximal power at a point that is a distance a along the beam direction from $\mathbf{r}'$, and the deposited energy decreases away from that point according to Equation (1.1), which gives the power per unit volume deposited at $\mathbf{r}$ due to ions striking at $\mathbf{r}'$,

$$P(\mathbf{r}, \mathbf{r}', t) = P_0 \exp\left(-\frac{d_\parallel^2}{2\alpha^2} - \frac{d_\perp^2}{2\beta^2}\right), \tag{1.1}$$

where $d_\parallel$ is the magnitude of the component of the displacement $(\mathbf{r} - \mathbf{r}')$ that is parallel to the ion direction and is $d_\parallel$ is the magnitude of the perpendicular component. The parameters α and β quantify how quickly the deposited power falls off. Eq. (1.1) is grounded in analytical work by Sigmund on the transport equation that describes the collision cascades [37]. It is clear from the functional form of the power distribution that the contours of equal energy deposition are ellipsoidal. The other key aspect of the Sigmund model is that the rate of erosion at a point on the surface is assumed to be directly proportional to the power per unit volume deposited there. Hobler *et. al.* tested the validity of the Sigmund model using Monte Carlo simulations of ion impacts on Si at with incidence angles from perpendicular to grazing [38]. They found that for Ar and Xe ions at 2 and 20 keV and nongrazing incidence, the Sigmund model's predictions are within a factor of 2 of the Monte Carlo results. The Sigmund model was found to be a poor approximation if the angle of incidence was near grazing or if the ion energy was too high. This occurs because the assumptions that the number of sputtered atoms is proportional to the power deposited per unit volume and that the distribution of power deposited is independent of the surface shape are both invalid under these conditions [38].

Bradley-Harper Theory

The Bradley-Harper theory is a continuum model that applies to elemental materials bombarded by a broad ion beam [33]. It takes into account two physical effects: sputtering and surface

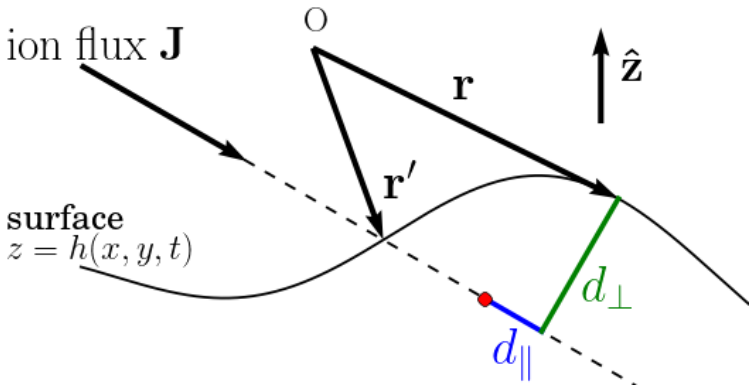

Figure 1.10: A focused ion beam with flux **J** is incident upon the surface $h(x, y, t)$ at point $\mathbf{r}'$. In the Sigmund model of sputtering, maximal power is deposited at a point in the solid that is a distance a along the beam direction from $\mathbf{r}'$. The point of maximal power deposition is indicated by the red dot. The power deposited in the solid decreases as the parallel and perpendicular distances ($d_{\parallel}$ and $d_{\perp}$) increase, and the contours of equal power deposition are ellipsoidal.

self-diffusion. While these are not the only effects present, BH took them to be the most important. Sputtering leads to the onset of pattern formation, as will be shown in this section. Surface self-diffusion is a smoothing process that is necessary for the theory to be well-posed. Specifically, it damps short wavelength modes and leads to a finite selected wave number for the ripple pattern.

The BH theory uses the Sigmund model of sputtering and from it develops an equation of motion (EOM) for an initially nominally flat bombarded surface [33]. The linear EOM that BH obtained is

$$\frac{\partial h}{\partial t} = -v_0 + v_0' \frac{\partial h}{\partial x} + \kappa_1 \frac{\partial^2 h}{\partial x^2} + \kappa_2 \frac{\partial^2 h}{\partial y^2} - B\nabla^2\nabla^2 h. \tag{1.2}$$

The first term on the right-hand side, $-v_0$, is the erosion rate of a completely flat surface. The second term, $v_0' \frac{\partial h}{\partial x}$, is the contribution to the erosion rate at linear order that arises if the surface is sloped. The coefficients κ_1 and κ_2 describe the curvature dependence of the sputter yield. Ripples develop from a nominally flat surface if and only if at least one of them is negative. Prior attempts to explain the formation of ripples in these systems neglected the curvature dependence of the sputter yield, and so were unsuccessful in explaining the onset of pattern formation [39]. The last term, $-B\nabla^2\nabla^2 h$, accounts for surface self-diffusion that is taken be thermally-activated in the BH theory [33].

According to the BH analysis, κ_2 is always negative and for angles of incidence less than some critical value, κ_1 is also negative. Thus, in the linear BH theory, the nominally flat surface is always unstable. If $\kappa_1 < \kappa_2$, then the BH theory predicts that the observed ripples will be parallel-mode ripples. Parallel-mode ripples that are observed in experiments do propagate, which coincides with the prediction of the BH theory [3, 33, 34]. If $\kappa_2 < \kappa_1$, then the BH theory predicts that the observed ripples will be perpendicular-mode ripples. The BH theory predicts that the perpendicular-mode ripples will be stationary, which is clear from symmetry. Furthermore, experiments show that the crossover from parallel-mode ripples to perpendicular-mode ripples occurs at a critical angle of incidence, and this coincides with the predictions of the linear BH theory as well [1, 33]. The BH theory also predicts the wavelength of the observed ripples and the order of magnitude obtained is in reasonable agreement with experiment [33].

Carter-Vishnaykov effect

Sputtering is not the only physical mechanism that can produce an instability required for the formation of ripple patterns. Another is mass redistribution, also called the Carter-Vishnaykov effect. This effect refers to the incident ions imparting momentum to the atoms near the surface, causing them to move. The CV effect, unlike sputtering, conserves the mass of the target material, hence the alternate term mass redistribution. However, the CV effect cannot produce an instability in the transverse direction and so perpendicular-mode ripples cannot arise due to this effect. Since perpendicular-mode ripples are observed experimentally, it is clear that sputtering is a stronger effect in those systems for the angles of incidence for which perpendicular-mode ripples are observed. On the other hand, the BH theory predicts that a nominally flat surface is unstable for all angles of incidence θ. However, in experiments with small θ, the surface often smooths. The reason for this discrepancy is that the BH theory only takes into account two physical mechanisms: sputtering and surface self-diffusion. We will now derive a simple model for the CV effect and perform a linear stability analysis on it to show that the CV effect leads to smoothing at small angles of incidence.

The unit normal to the unperturbed surface (which coincides with the $x-y$ plane) is simply $\hat{\mathbf{z}}$. Perturbing the perfectly flat surface yields a position dependent surface normal vector given by

$$\hat{\mathbf{n}} \equiv \frac{\hat{\mathbf{z}} - \nabla h}{\sqrt{1 + h_x^2 + h_y^2}}. \tag{1.3}$$

We denote the incident ion flux by $\vec{\mathbf{J}}$; its direction is given by

$$\hat{\mathbf{J}} = (-\sin\theta)\,\hat{\mathbf{x}} + (-\cos\theta)\,\hat{\mathbf{z}}. \tag{1.4}$$

The CV effect produces a flux of atoms within a thin surface layer. To find this flux, first we calculate the tangential component of the force, $\mathrm{d}\vec{\mathbf{F}}_{\parallel}$ experienced by an infinitesimal surface area element $\hat{\mathbf{n}}\mathrm{d}A$:

$$\begin{aligned} \mathrm{d}\vec{\mathbf{F}}_{\parallel} &= \mathrm{d}\vec{\mathbf{F}} - \mathrm{d}\vec{\mathbf{F}}_{\perp} \\ &= \vec{\mathbf{J}} \cdot \hat{\mathbf{n}}\mathrm{d}A\left[\vec{\mathbf{p}} - (\vec{\mathbf{p}} \cdot \hat{\mathbf{n}})\,\hat{\mathbf{n}}\right], \end{aligned} \tag{1.5}$$

where $\vec{\mathbf{p}}$ is the incident ion momentum, $\mathrm{d}\vec{\mathbf{F}}$ is the force experienced by $\hat{\mathbf{n}}\mathrm{d}A$, and $\mathrm{d}\vec{\mathbf{F}}_{\perp}$ is the perpendicular component of the force experienced by $\hat{\mathbf{n}}\mathrm{d}A$. Now, we use $\vec{\mathbf{p}} = p\hat{\mathbf{J}}$ and divide Eq. (1.5) by $\mathrm{d}A$ to obtain the tangential force per unit area, denoted by $\vec{\tau}_{\parallel}$ and given by

$$\vec{\tau}_{\parallel} = pJ\left(\hat{\mathbf{J}} \cdot \hat{\mathbf{n}}\right)\left[\hat{\mathbf{J}} - \left(\hat{\mathbf{J}} \cdot \hat{\mathbf{n}}\right)\hat{\mathbf{n}}\right]. \tag{1.6}$$

Next, we combine Eqs. (1.3) and (1.4) with Eq. (1.6). Since the goal is to perform a linear stability analysis, we will drop all nonlinear terms that arise in this derivation. To linear order, we find that

$$\tau_{\parallel} = -pJ\left\{\left[\frac{\sin(2\theta)}{2} + \cos(2\theta)h_x\right]\hat{\mathbf{x}} + \left[\cos^2(\theta)h_y\right]\hat{\mathbf{y}} + \left[\frac{\sin(2\theta)}{2}h_x\right]\hat{\mathbf{z}}\right\}. \tag{1.7}$$

Since the tangential force per unit area $\tau_{\parallel}$ is nonzero for a perturbed surface, the incident ions cause an atomic surface flux, which we denote by $\vec{\mathbf{J}}_S$. We assume that $\vec{\mathbf{J}}_S$ is proportional to $\tau_{\parallel}$ and choose

the constant of proportionality to be μ/p, where $\mu > 0$ is a dimensionless constant. Thus, we find that

$$\vec{\mathbf{J}}_S = -\mu J \left\{ \left[\frac{\sin(2\theta)}{2} + \cos(2\theta) h_x \right] \hat{\mathbf{x}} + \left[\cos^2(\theta) h_y \right] \hat{\mathbf{y}} + \left[\frac{\sin(2\theta)}{2} h_x \right] \hat{\mathbf{z}} \right\}. \tag{1.8}$$

Let Ω be the atomic volume of the target; i.e., $\Omega = 1/n$, where n is the number density of the atoms in the solid. When an incident ion causes a surface atom to move on the surface, a volume of Ω is evacuated from surface at the atom's original location. Therefore, the dynamics of the surface due solely to the CV effect are governed by

$$h_t = -\Omega \vec{\nabla} \cdot \vec{\mathbf{J}}_S, \tag{1.9}$$

where the subscript t on h denotes partial differentiation with respect to t. Note that in the CV model, the surface atoms only move – they are not ejected. Furthermore, implantation of incident ions in the surface is considered a negligible effect and is not included in the CV model (or the BH model). Thus, in the CV model we expect the total mass of the surface to be conserved, which is consistent with Eq. (1.9). After combining Eqs. (1.8) and (1.9), we obtain

$$h_t = \Omega \mu J \left[\cos(2\theta) h_{xx} + (\cos^2\theta) h_{yy} \right], \tag{1.10}$$

where the subscripts x and y on h denote partial differentiation. Note that for $\theta = 0$, Eq. (1.10) reduces to the diffusion equation. Now, we consider the evolution of a single arbitrary Fourier mode in the linearized CV model. The single mode is given by

$$h(\vec{\mathbf{x}}, t) = A \mathrm{e}^{Rt} \mathrm{e}^{\mathrm{i}\left(\vec{\mathbf{k}} \cdot \vec{\mathbf{x}} - \omega t\right)}, \tag{1.11}$$

where $R = R(\vec{\mathbf{k}})$ is the real-valued growth rate of the mode with wave vector $\vec{\mathbf{k}} = k_x \hat{\mathbf{x}} + k_y \hat{\mathbf{y}}$, and ω is its angular frequency. Inserting the ansatz Eq. (1.11) into the linearized CV equation of motion (1.10), we find that $\omega = 0$ and

$$R(\vec{\mathbf{k}}) = -\Omega\mu J\left[\cos(2\theta)k_x^2 + (\cos^2\theta)k_y^2\right]. \tag{1.12}$$

This growth rate is negative for $\theta < 45^{\circ}$, which in particular implies that the CV effect is smoothing for normal incidence bombardment. If the angle of incidence exceeds 45°, the CV effect will cause parallel-mode ripples to grow exponentially. Since $\omega = 0$, the surface ripples do not propagate in the linearized CV theory, even for oblique angles of incidence. This fact may seem odd for $\theta \neq 0$ since the incident ions carry a nonzero $x-\text{component}$ of momentum, and intuitively one would expect as a consequence that the surface ripples would propagate in the same direction. However, the analysis we performed only applies if the surface perturbation is sufficiently small in amplitude – for larger amplitudes, the ripples can propagate. If $\theta > 45^{\circ}$, the fastest growing mode has $|k_x| = \infty$ according to Eq. (1.12). This corresponds to a zero wavelength mode, which would imply that the observed wavelength would be on the cutoff length scale of the continuum approximation, *i.e.*, the spacing of the surface atoms. Since the wavelength of ripples observed in experiments is several orders of magnitude larger than the atomic spacing, an additional smoothing term must be included, as was the case with the BH theory. After including surface self-diffusion in the CV model, Eq. (1.10) is replaced by

$$h_t = \Omega\mu J\left[\cos(2\theta)h_{xx} + (\cos^2\theta)h_{yy}\right] - B\nabla^2\nabla^2 h, \tag{1.13}$$

and the growth rate is then

$$R(\vec{\mathbf{k}}) = -\Omega\mu J\left[\cos(2\theta)k_x^2 + (\cos^2\theta)k_y^2\right] - Bk^4. \tag{1.14}$$

If $\theta > 45^{\circ}$, then this growth rate is maximal for the mode with $\vec{\mathbf{k}} = \vec{\mathbf{k}}_c$, where

$$\vec{\mathbf{k}}_c = \pm\sqrt{\frac{\mu\Omega J\left|\cos(2\theta)\right|}{2B}}\hat{\mathbf{x}}. \tag{1.15}$$

Thus, in this simple model of the CV effect, the observed ripple orientation will always be parallel to the ion flux projected onto the surface, and so it cannot explain the appearance of perpendicular-mode ripples that occur in experiments.

Kuramoto-Sivashinsky equation

The linear BH EOM (1.2) is only valid for sufficiently early times during the bombardment. Once ripples of sufficiently large amplitudes form, the nonlinearities contribute significantly to the surface dynamics. For example, they prevent the formation of arbitrarily large ripple amplitudes. We first consider the equation of motion for normal-incidence ion bombardment of an elemental target that is obtained by appending the lowest order nonlinear dependence of the erosion rate on surface slope to the linear Bradley-Harper (BH) equation [22, 40]. The equation obtained is

$$\frac{\partial h}{\partial t} = -v_0 - A\nabla^2 h - B\nabla^2\nabla^2 h + \lambda\left|\nabla h\right|^2, \tag{1.16}$$

where $A = -\kappa_1 = -\kappa_2$ is positive. The term $-v_0$ can be eliminated by letting $u(x,t) = h(x,t) + v_0 t$. This results in the dimensional form of the isotropic Kuramoto-Sivashinsky (KS) equation,

$$\frac{\partial u}{\partial t} = -A\nabla^2 u - B\nabla^2\nabla^2 u + \lambda\left|\nabla u\right|^2. \tag{1.17}$$

By rescaling u, x, y and t, Eq. (1.17) can be reduced to a dimensionless one that involves no free parameters. These rescalings are given by

$$\tilde{u} = \frac{\lambda}{A}u, \tag{1.18}$$

$$\tilde{x} = \sqrt{\frac{A}{B}}x, \tag{1.19}$$

$$\tilde{y} = \sqrt{\frac{A}{B}}y \tag{1.20}$$

and

$$\tilde{t} = \frac{A^2}{B} t. \tag{1.21}$$

Inserting Eqs. (1.18)-(1.21) and dropping the tildes yields the dimensionless isotropic KS equation,

$$\frac{\partial u}{\partial t} = -\nabla^2 u - \nabla^2 \nabla^2 u + |\nabla u|^2 . \tag{1.22}$$

Note that it is not necessary to study a form of Eq. (1.22) with the quadratic nonlinearity subtracted instead of added, because the solutions of the two equations are related by $u \to -u$. The isotropic KS equation has been studied extensively, partly because it causes a low amplitude white noise initial condition to spontaneously evolve into spatiotemporal chaos [22, 40]. The KS equation has been used to deduce scaling properties of ion bombarded surfaces [22]. The KS equation yields dynamics akin to those seen in the experiments that produce disordered mounds. The surface governed by the KS equation has no substantial hexagonal order, which can be verified by the methods discussed in Section 1.5.2, where we describe a quantitative method of characterizing hexagonal order.

If the angle of incidence is oblique, then the isotropic KS equation is not valid, since the rotational symmetry is broken; i.e., the x and y directions are distinguishable. Thus, for systems bombarded at oblique incidence, the isotropic KS equation is replaced by the anisotropic Kuramoto-Sivashinsky (AKS) equation. The AKS equation is

$$\frac{\partial u}{\partial t} = \alpha \frac{\partial u}{\partial x} + \kappa_1 \frac{\partial^2 u}{\partial x^2} + \kappa_2 \frac{\partial^2 u}{\partial y^2} - B \nabla^2 \nabla^2 u + \lambda_1 \left(\frac{\partial u}{\partial x} \right)^2 + \lambda_2 \left(\frac{\partial u}{\partial y} \right)^2 , \tag{1.23}$$

where we will assume that κ_1 and/or κ_2 is negative so that there is a surface instability. The term $\alpha \frac{\partial u}{\partial x}$ can be eliminated by by setting $\tilde{x} \equiv x + \alpha t$ and then dropping the tildes. Rescaling cannot be used to reduce Eq. (1.23) to an EOM with no free parameters; however, it could be used to eliminate up to three parameters. Note that since B is a scalar in Eq. (1.23), we have assumed that the surface self-diffusion is isotropic. It is of course possible to generalize the model to one with anisotropic surface self-diffusion, but this would also increase the complexity of the

model by increasing the number of free parameters. Furthermore, a scalar value for B is a good approximation under appropriate conditions: for example, if the dominant physical mechanism that contributes to B is thermally activated surface self-diffusion [41].

Extended Kuramoto-Sivashinsky equation

Castro *et al*. developed a theory that in addition to sputtering and surface self-diffusion also includes a mobile surface layer [42–44, 44]. The equation of motion they obtained adds a second nonlinear term to the KS equation:

$$\frac{\partial u}{\partial t} = -\nu\nabla^2 u - \kappa\nabla^2\nabla^2 u + \lambda_1 \left|\nabla u\right|^2 - \lambda_2\nabla^2 \left|\nabla u\right|^2 . \tag{1.24}$$

Here $\nu > 0$, $\kappa > 0$, λ_1 and λ_2 are constants that depend on the properties of the ion beam and target material. The signs of λ_1 and λ_2 must be the same to prevent the uncontrolled growth of cancellation modes [44]. Eq. (1.24) can be rescaled so that u, x, y and t are dimensionless to give

$$\frac{\partial u}{\partial t} = -\nabla^2 u - \nabla^2\nabla^2 u + \left|\nabla u\right|^2 - r\nabla^2 \left|\nabla u\right|^2 , \tag{1.25}$$

where $r > 0$ is a constant and equals

$$r = \frac{\nu\lambda_2}{\kappa\lambda_1}. \tag{1.26}$$

We will refer to Eq. (1.25) as the extended Kuramoto-Sivashinsky equation (eKS equation). Castro *et al.* found that if r is appropriately chosen, then Eq. (1.25) yields a surface with short-range hexagonal order if the initial condition is low amplitude spatial white noise [42–44].

1.3 Ion Bombardment of Binary Materials

We have seen in the previous section that ion bombardment of a nominally flat elemental surface can lead to the formation of ripple and terraced topographies. In this section, we discuss pattern formation on the surfaces of materials composed of two elements.

1.3.1 Experimental Results

The formation of nanodots arranged in hexagonal array was first observed by Facsko *et al.*, and the results were published in *Science* [6]. In their experiment, they bombarded GaSb at normal incidence with 0.42 keV Ar^+ ions. After 40 seconds of exposure, nanodots with an average diameter of 18 nm formed, and their number density was 4×10^{17} dots/cm^2. After 200 seconds of bombardment, the average diameter of the nanodots had increased to 34 nm. At 400 seconds of exposure, the average dot diameter saturated at the value of 50 nm, and the dot diameter was approximately equal to the dot spacing. The pattern did not change appreciably after the pattern at 400 seconds was reached [6]. We show a SEM result from Ref. [6] in Figure 1.11.

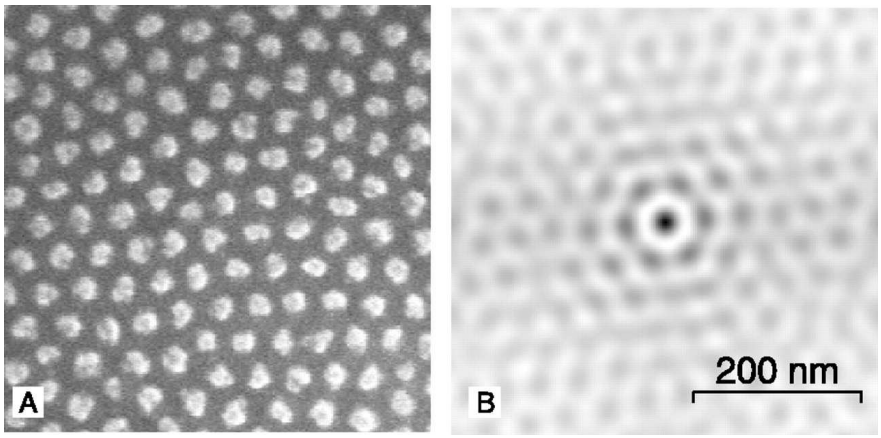

Figure 1.11: (a) A SEM image of a surface of initially nominally flat GaSb that evolved into an array of nanodots with a high degree of local hexagonal order after normal-incidence ion bombardment. (b) The autocorrelation of the surface. These results were published in 1999 by Facsko *et al.* in Ref. [6].

Another experiment in which hexagonally ordered nanodots were formed was carried out by Frost *et al.* in Ref. [7]. In this experiment, InP surfaces were rotated with concurrent 0.5 keV Ar^+ ion bombardment at oblique incidence. Some of their results are shown in Figure 1.12; this figure shows surfaces obtained at four different angles of incidence.

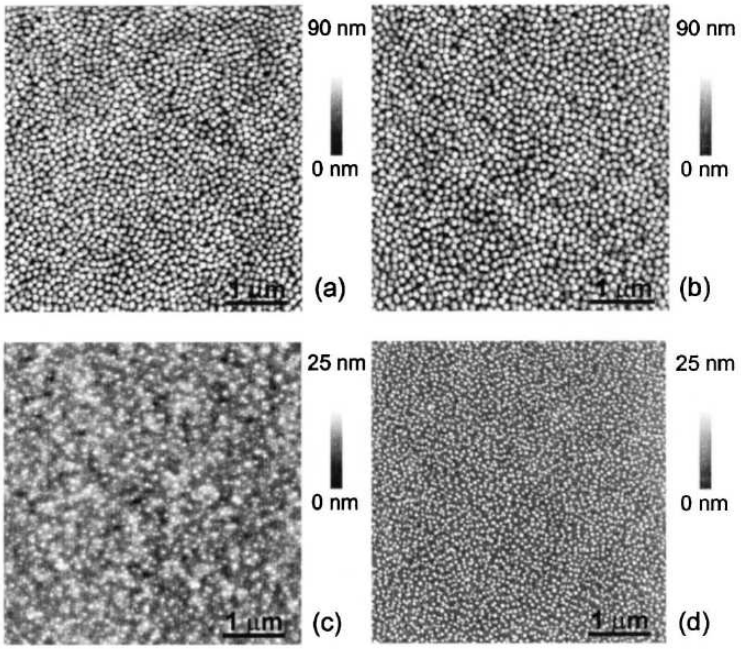

Figure 1.12: AFM images (scan size 3 mm) of Ar^+ sputtered InP surfaces ($E_{\rm ion} = 500$ eV, $j_{\rm ion} = 150$ mA/cm^2 , $t = 1200$ s) at an incidence angle of $10^{\rm o}$ (a), $30^{\rm o}$ (b), $70^{\rm o}$ (c), and $80^{\rm o}$ (d). This figure and caption are from Ref. [7].

1.3.2 Theory – Binary Materials

Bradley-Shipman Theory

Bradley and Shipman have developed a continuum model for normal-incidence ion bombardment of a solid composed of two atomic species, which we will call the BS theory [8, 15, 16]. In their model, it is assumed that one of the atomic species is sputtered more easily than the other, which we will refer to as preferential sputtering. An essential aspect of the BS theory is the coupling of the surface composition to the surface height, which was an idea first studied by Shenoy, Chan, and Chason [45]. The BS theory is also relevant to experiments in which the target material is elemental, and the ion beam implants a second non-volatile ion species into the material while eroding it; however, this idea will not be explored further in this thesis. In the BS theory, under appropriate experimental conditions, there can be a narrow band of linearly unstable wave vectors. Since there are also quadratic nonlinearities in the equation of motion they found to govern the surfaces, hexagonal pattern formation can occur and can be understood using standard pattern formation theory [46, 47]. When the initial surface is nominally flat, the hexagonal ordering will

be local only, due to the isotropic nature of the governing equation of motion and the initial condition. In other words, the surface will develop distinct regions of hexagonal order with different orientations. The BS equations of motion are

$$\frac{\partial u}{\partial t} = \phi - \nabla^2 u - \nabla^2 \nabla^2 u + \lambda \left(\nabla u\right)^2 \tag{1.27}$$

and

$$\frac{\partial \phi}{\partial t} = -a\phi + b\nabla^2 u + c\nabla^2 \phi + \nu\phi^2 + \eta\phi^3, \tag{1.28}$$

where ϕ is the deviation of the composition from its steady-state value, and λ, a, b, c, ν and η are real constants that depend on the properties of the target material and the ion beam [8, 15, 16]. Note that Eq. (1.27) is the same as the KS equation, except for the first term on the right hand side, which couples the dynamics to the surface composition and arises from preferential sputtering. The terms on the right hand side of Eq. (1.28) that are proportional to powers of ϕ also arise from sputtering. The $c\nabla^2\phi$ term is due to surface diffusion. The CV effect is the physical origin of the term $b\nabla^2 u$, and this term is responsible for a surprising result within the BS theory: the elemental species that is more easily sputtered actually ends up concentrated at the top of the nanodots. This occurs because the preferentially sputtered species is influenced less by the CV effect, and the combination of sputtering and mass redistribution are necessary for formation of hexagonal arrays of nanodots [8, 15, 16]. Bradley and Shipman performed a linear stability analysis on the BS equations (1.27) and (1.28) in Ref. [8]. They presented the region of the (a,b,c) parameter space that results in a linearly unstable surface, first partitioning the (a,c) space into three regions, and then they provided the conditions on b in each of those regions that lead to an instability. The three regions of the (a,c) parameter space are depicted in Fig. 1.13. In region I, the threshold value of b for an instability is denoted by b_T. If b is slightly less than b_T in region I, then there exists a narrow band of linearly selected wave vectors, which is shown in Fig. 1.14. The combination of the narrow band of linearly selected wave vectors with the quadratic nonlinearity in Eq. (1.28) can lead to the formation of hexagonally arranged nanodots. This was analytically demonstrated using

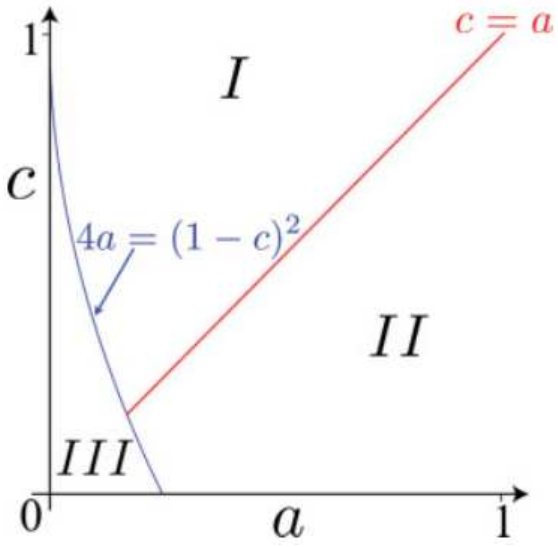

Figure 1.13: The parameter space is partitioned into three different regions based on the linear stability analysis. This figure is from Ref. [8].

amplitude equations obtained from a multiple scales analysis and numerically verified by direct integration of Eqs. (1.27) and (1.28) [8, 15, 16].

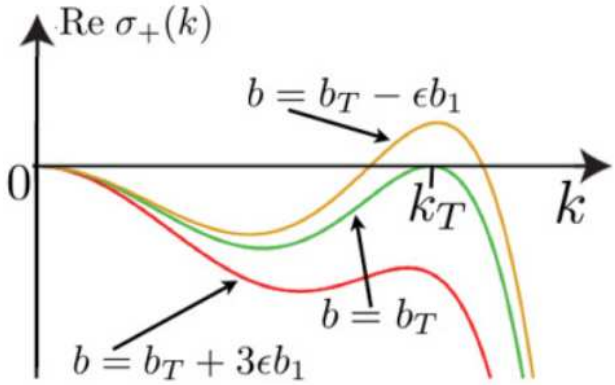

Figure 1.14: This plot shows the linear growth rate's dependence on ripple wave number in region I of the parameter space shown in Fig. 1.13. If b is slightly less than the threshold value b_T, then there is a narrow band wave vectors that are linearly unstable. If b exceeds b_T, then every mode is linearly damped, and the nominally flat surface will flatten. This figure is from Ref. [8].

Motta, Bradley, and Shipman extended the BS theory to the case where the angle of incidence can be oblique [48]. In the theory they derived, they showed that well-ordered ripples formed for a range of parameter values. This is in accord with an experimental work in which well-ordered

ripple patterns on SiC after oblique incidence ion bombardment [49]. They also demonstrated that defects in the surface tend to occur where the surface is low. This phenomenon is observable in our simulations of the BS equations in this work as well.

1.4 Analytical Background

1.4.1 Linear Stability Analysis

In order to determine whether a nominally flat surface is stable or unstable, one performs a linear stability analysis. Although the governing equation of motion is nonlinear, at sufficiently early times, the surface dynamics is approximated well by the linearized equation. The deviation of surface height from its unperturbed steady-state value is represented by a function $u = u(x, y, t)$, and since it is nominally flat initially, $u_0 \equiv u(x, y, 0)$ satisfies $|u_0| \ll 1$ for all x and y. The linear stability analysis determines the growth rates and propagation velocities of the Fourier modes so one can predict how u will evolve at early times. In particular, the mode with the largest growth rate will be the one observed. To demonstrate this, a linear stability analysis will be performed on the AKS equation of motion, Equation (1.23). Linearizing the AKS equation of motion about the uniform solution, which describes a surface that is perfectly flat, one obtains

$$\frac{\partial u}{\partial t} = \alpha \frac{\partial u}{\partial x} + \kappa_1 \frac{\partial^2 u}{\partial x^2} + \kappa_2 \frac{\partial^2 u}{\partial y^2} - B\nabla^2\nabla^2 u., \tag{1.29}$$

which is BH equation (1.2) written in terms of $u = h + v_0 t$ and with $v_0' = \alpha$. Now, we let

$$u = \exp(Rt) \exp[\mathrm{i}(k_1 x + k_2 y - \omega t)], \tag{1.30}$$

where R is the rate of growth of the Fourier mode's amplitude and ω is the angular frequency. Inserting Eq. (1.30) into Eq. (1.29), one finds that

$$R = -(\kappa_1 k_1^2 + \kappa_2 k_2^2) - B(k_1^2 + k_2^2)^2 \tag{1.31}$$

and

$$\omega = -v_0' k_1. \tag{1.32}$$

Thus, if $\kappa_1 < \kappa_2$ and $\kappa_1 < 0$, the growth rate is maximized for the selected wave vector

$$(k_1, k_2) = \left(\pm\sqrt{\frac{|\kappa_1|}{2B}}, 0 \right) \tag{1.33}$$

and these parallel-mode ripples would propagate with velocity $-\alpha$ in the x-direction. If $\kappa_2 < \kappa_1$ and $\kappa_2 < 0$, the growth rate is maximized for the selected wave vector

$$(k_1, k_2) = \left(0, \pm\sqrt{\frac{|\kappa_2|}{2B}} \right) \tag{1.34}$$

and these perpendicular-mode ripples would not propagate. If both κ_1 and κ_2 are positive, the surface is stable and ripples do not form.

1.4.2 Shock Waves

In Section 2.4, we will demonstrate that the terrace formation observed in our simulations is closely related to the formation of undercompressive shock waves. For convenience and clarity, some essential background on shocks is included in this section. Comprehensive treatments of this topic may be found in Refs. [50] and [51].

Consider a partial differential equation of the form

$$\rho_t + \partial_x F(\rho) = \nu D(\rho_{xx}, \rho_{xxxx}), \tag{1.35}$$

where $\rho = \rho(x, t)$, $\nu > 0$ is a constant and the functions F and D are given. In the $\nu \to 0$ limit, equation (1.35) reduces to

$$\rho_t + \partial_x F(\rho) = 0, \tag{1.36}$$

which is a conservation law for the quantity ρ. The flux of ρ is clearly $F(\rho)$. Equation (1.36) may also be written

$$\rho_t + F'(\rho)\rho_x = 0, \tag{1.37}$$

which shows that the advection velocity of a point with $\rho = \rho_0$ is $F'(\rho_0)$.

Suppose that there is a traveling wave solution to (1.35) of the form $\rho(x,t) = q(x - Ut)$ with $q(\tau) \to q_\pm$ for $\tau \to \pm\infty$, where U, q_+ and q_- are constants. If in the limit that ν tends to zero, $q(\tau)$ tends to q_- for all $\tau < 0$ and if $q(\tau)$ tends to q_+ for all $\tau > 0$, then $\rho(x,t) = q(x - Ut)$ is called a shock wave. Thus, the solution develops a step discontinuity in the $\nu \to 0$ limit if it is a shock. For $\nu > 0$, on the other hand, the term $\nu D(\rho_{xx}, \rho_{xxxx})$ on the right-hand side of (1.35) prevents the formation of a discontinuity and yields an interface of nonzero width between the regions in which ρ is very nearly equal to q_+ and q_-.

The propagation velocity of a shock is given by the Rankine-Hugoniot condition

$$U = \frac{F(q_+) - F(q_-)}{q_+ - q_-}. \tag{1.38}$$

Most shocks that occur in physical situations are compressive shocks; these satisfy the Lax entropy condition

$$F'(q_+) < U < F'(q_-). \tag{1.39}$$

However, shocks that violate this condition do exist and are called undercompressive shocks [51]. For a given value of q_-, an undercompressive shock may exist for a few special values of q_+ or for none at all. Undercompressive shocks can occur only if the flux F is not a convex function of ρ [51].

1.5 Numerical Methods

We now turn our attention to the various numerical methods used throughout this work. These include numerical integration techniques and methods of quantifying pattern order.

1.5.1 Numerical Integration

Galerkin Method with VODE Integration

For reasons of computational speed, we only use the Galerkin method with VODE integration when the surface depends one spatial independent variable, and so we restrict our attention to one space and one time dimension in this section. We assume a finite spatial domain and impose periodic boundary conditions in order to model the nearly infinitely-extended domain. As is well known, the Fourier representation of the surface allows one to obtain exact solutions to the linearized equation of motion. One can also attempt to solve a nonlinear PDE with Fourier analysis; the difficulty, however, is that the rate of growth (or decay) of a given mode k_g directly depends on all modes k_i and k_j such that $k_i + k_j = k_g$. Thus, in order to find the exact solutions to nonlinear equations, one would have to solve infinitely many coupled nonlinear ordinary differential equations (ODEs). Since this is not feasible, we instead find approximate solutions by truncating the Fourier expansion after a certain wave number. This wave number is chosen so that the amplitudes of the dropped modes are small enough that they do not contribute appreciably to the dynamics of the surface. Inserting the truncated expansion into the equation of motion will yield a finite system of coupled ordinary differential equations, which may be numerically integrated using any one of a variety of standard integration routines. The integration method we chose to use to integrate the system of ODEs is called VODE [52].

Exponential Time Differencing

Our primary tool for numerically integrating equations of motion is a fourth-order Runge-Kutta Exponential Time Differencing (ETD) routine. This routine was originated by Cox and Matthews [53], and improved by Kassam and Trefethen [54]. The main advantage of this method over the Galerkin method with VODE integration is speed. The idea behind ETD is as follows. Consider an equation of motion of the form

$$u_t = \mathbf{L}u + \mathbf{N}(u), \tag{1.40}$$

where $u = u(x, y, t)$ describes the surface topography, $\mathbf{L}$ is a linear differential operator and $\mathbf{N}(u)$ is the nonlinear part of the equation. Multiply both sides by the integrating factor $e^{-\mathbf{L}t}$ to get

$$e^{-\mathbf{L}t}u_t - e^{-\mathbf{L}t}\mathbf{L}u = e^{-\mathbf{L}t}\mathbf{N}(u), \tag{1.41}$$

which is simply

$$\partial_t e^{-\mathbf{L}t}u = e^{-\mathbf{L}t}\mathbf{N}(u). \tag{1.42}$$

Integrating over one time step, the duration of which we denote by Δ, one obtains the exact equation

$$u_{n+1} = e^{\mathbf{L}\Delta}u_n + e^{\mathbf{L}\Delta}\int_0^{\Delta} e^{-\mathbf{L}\tau}\mathbf{N}(u(t_n + \tau))\mathrm{d}\tau, \tag{1.43}$$

where u_n is the surface at time step n, and t_n is the time at step n [53]. This integral is then evaluated numerically with a fourth-order Runge-Kutta method. Therefore, we can obtain the surface at time step $n + 1$ from the surface at step n. We elaborate on how this is done in the next section.

The Runge-Kutta Method

We now discuss how the Runge-Kutta (RK) method is a can be applied to solving initial value problem (IVP) ODEs; this will clarify how RK can be used to approximate the exact formula Eq. (1.43). The first order Runge-Kutta (RK1) method is a synonym for the forward Euler method, and so we will first discuss Euler's method then generalize the idea to higher order Runge-Kutta schemes. The RK1 method is the most direct way of numerically solving the IVP for a system of first-order ODEs; note, however, that it can also be applied to IVPs of higher order because an ODE of order p is equivalent to a system of p first-order ODES [55]. Consider the following system of ODEs

$$\frac{\mathrm{d}\vec{y}}{\mathrm{d}t} = \vec{F}\left[t, \vec{y}\,(t)\right], \tag{1.44}$$

where we have chosen to use vector notation to write our system compactly. Suppose we know the value of $\vec{y}$ at some time t_n and want to determine its value at a later time t_{n+1}, where m is an

integer. Then from Eq. (1.44) we have that

$$\vec{y}_{n+1} = \vec{y}_n + \int_{t_n}^{t_{n+1}} \vec{F}\left[t, \vec{y}\,(t)\right] \mathrm{d}t, \tag{1.45}$$

where $\vec{y}_{n+1} \equiv \vec{y}\,(t_{n+1})$ and $\vec{y}_n \equiv \vec{y}\,(t_n)$. A direct implementation of Eq. (1.45) is not possible, since the integral depends on the values of $\vec{y}$ for times greater than t_n, and we only know the values of t_n and $\vec{y}_n$. Instead, the integral must be approximated using only the known data t_n and $\vec{y}_n$. We define $\Delta \equiv t_{n+1} - t_n$. By choosing a sufficiently small Δ and if $\vec{F}$ is sufficiently smooth, then $\vec{F}$ will not change much as the integral in Eq. (1.45) is performed, and so

$$\vec{y}_{n+1} \simeq \vec{y}_n + \vec{F}\left(t_n, \vec{y}_n\right) \Delta, \tag{1.46}$$

which is the formula used to compute one step of the RK1 method. After this step is performed, the value of $\vec{y}_{n+1}$ has been determined, and clearly t_{n+1} is also known. Thus, Eq. (1.46) can be applied iteratively to generate a sequence of values $\{\vec{y}_p\}$ for integers $p \geq m$. The sequence $\{\vec{y}_p\}$ is a discrete approximation to the exact solution $\vec{y}$ that satisfies Eq. (1.44) and depends on the continuous variable t. The reason the RK1 method is called first order is the error accumulated over multiple iterations is of order Δ. The RK1 method is also a one step method because each iteration only requires one evaluation of $\vec{F}$. Higher order RK methods use a weighted average of evaluations of $\vec{F}$ to obtain a better approximation. In general, the number of steps required to obtain a given order of accuracy is greater than or equal to order of accuracy. The RK4 method is unique in that it is the highest order method for which the number of steps equals the order. Thus, the RK4 method is a good balance between speed and accuracy. The most common implementation of RK4 is given by

$$\vec{y}_{n+1} \simeq \vec{y}_n + \tfrac{1}{6}\left(\vec{F}_1 + 2\vec{F}_2 + 2\vec{F}_3 + \vec{F}_4\right) \Delta, \tag{1.47}$$

where

$$\vec{F}_1 \equiv \vec{F}\left(t_n, \vec{y}_n\right), \tag{1.48}$$

$$\vec{F}_2 \equiv \vec{F}\left(t_n + \tfrac{1}{2}\Delta, \vec{y}_n + \tfrac{1}{2}\vec{F}_1\right), \tag{1.49}$$

$$\vec{F}_3 \equiv \vec{F}\left(t_n + \tfrac{1}{2}\Delta, \vec{y}_n + \tfrac{1}{2}\vec{F}_2\right), \tag{1.50}$$

$$\vec{F}_4 \equiv \vec{F}\left(t_n + \Delta, \vec{y}_n + \vec{F}_3\right). \tag{1.51}$$

Now we return to our discussion of Eq. (1.43). Using a Fourier Series representation for u, Eq. (1.43) becomes a system of equations that is similar to Eq. (1.45), except with additional exponential factors multiplying the terms on the right hand side. As a consequence, the usual RK4 method given by Eq. (1.47) cannot be used directly. Cox and Matthews derived a RK4 method for Eq. (1.43), which is given by

$$\begin{aligned} u_{n+1} = {} & \mathrm{e}^{\mathbf{L}/\Delta} + \Delta^{-2}\mathbf{L}^{-3}\{[-4 - \mathbf{L}\Delta + \mathrm{e}^{\mathbf{L}\Delta}(4 - 3\mathbf{L}\Delta + \mathbf{L}^2\Delta^2)]\mathbf{N}(u_n, t_n) \\ & + 2[2 + \mathbf{L}\Delta + \mathrm{e}^{\mathbf{L}\Delta}(-2 + \mathbf{L}\Delta)](\mathbf{N}(A_n, t_n + \Delta/2) + \mathbf{N}(B_n, t_n + \Delta/2)) \\ & + [-4 - 3\mathbf{L}\Delta - \mathbf{L}^2\Delta^2 + \mathrm{e}^{\mathbf{L}\Delta}(4 - \mathbf{L}\Delta)]\mathbf{N}(C_n, t_n + h)\}, \end{aligned} \tag{1.52}$$

where

$$A_n \equiv \mathrm{e}^{\mathbf{L}\Delta/2}u_n + \mathbf{L}^{-1}(\mathrm{e}^{\mathbf{L}\Delta/2} - \mathbf{I})\mathbf{N}(u_n, t_n), \tag{1.53}$$

$$B_n \equiv \mathrm{e}^{\mathbf{L}\Delta/2}u_n + \mathbf{L}^{-1}(\mathrm{e}^{\mathbf{L}\Delta/2} - \mathbf{I})\mathbf{N}(A_n, t_n + \Delta/2), \tag{1.54}$$

$$C_n \equiv \mathrm{e}^{\mathbf{L}\Delta/2}A_n + \mathbf{L}^{-1}(\mathrm{e}^{\mathbf{L}\Delta/2} - \mathbf{I})(2\mathbf{N}(B_n, t_n + \Delta/2) - \mathbf{N}(u_n, t_n)), \tag{1.55}$$

and where $\mathbf{I}$ is the identity matrix [53]. The terms in the square brackets of Eq. (1.52) suffer from numeric instability [53, 54]. Kassam and Trefethen modified the way in which these terms are evaluated and thereby improved the stability of the algorithm. We followed the approach of Kassam and Trefethen in our use of the ETDRK4 method in the simulations presented in this thesis. Their paper Ref. [54] is a good reference for further reading.

1.5.2 Quantifying Pattern Order

Persistent Homology

In this subsection, we describe a method of quantifying hexagonal order that is based on a topological data analysis technique known as persistent homology [56]. A brief overview of our method is given in this subsection; for details and the larger mathematical context, see Ref. [57].

To quantify the hexagonal order in a pattern of nanodots, we start by obtaining a discrete set of points from a surface pattern by recording the (x, y) coordinates of each nanodot peak, as in Fig. 1.15(a). As in Fig. 1.15(b), a circle of radius p is drawn around each of these points. The radius p is called the connectivity parameter; it will be increased from 0 to some maximum value. Clearly, for sufficiently large p, some of the circles will enclose each other's centers. For every two circles that enclose each other's centers, we connect the corresponding center points by an edge, as shown in Fig. 1.15(c). Every time three circles enclose each other's centers, we fill in the triangle that has the centers of the circles as its vertices (Fig. 1.15(d)), yielding a face. Finally, for a given value of p, a hole is identified whenever edges form the boundary of an unfilled region. For example, Fig. 1.15(e) shows 8 holes for $p = 12.5$. Note that hole $\#5$ corresponds to the largest defect seen in Fig. 1.15(a).

A hole's persistence interval length equals $p_{\text{end}} - p_{\text{start}}$, where p_{start} is the p value at which the hole forms, and p_{end} is the p value at which the hole gets filled in and ceases to exist. Summing up the lengths of all the persistence intervals gives a nonnegative number that we will call the H_1 sum.

There are multiple open-source software packages capable of computing persistence intervals for a set of discrete points. We used the R software package called *phom* in our analysis [58].

In Fig. 1.15(f), each hole *phom* identified in Fig. 1.15(a) is represented by a square. The coordinates of the square are the values of p_{start} and p_{end} for the hole in question. The persistence interval lengths are the vertical distances of the squares above the blue line. The 8 green squares are those with $p_{\text{start}} \leq 12.5 \leq p_{\text{end}}$ and so can be seen in Fig. 1.15(e); the red squares are holes not seen in Fig. 1.15(e).

Since a perfect hexagonal array of points is composed of equilateral triangles, every time three edges form a triangle, the corresponding three circles will enclose each other's centers, and therefore every triangle will be filled in at the same value of p. Thus, a persistent homology computation of a perfectly ordered hexagonal array of points will find no holes for any value of p, and so the H_1 sum will be zero. Whenever there is a vacancy or another type of defect in the hexagonal lattice, the persistent homology analysis will reveal the presence of one or more holes. Therefore, we can quantify the amount of disorder in an imperfect hexagonal array of points using the H_1 sum: The smaller the H_1 sum, the better the hexagonal order.

Nearest-Neighbor Distribution

A second approach we will use to quantify hexagonal order involves computing the number of nearest neighbors each nanodot has. As in the persistent homology approach, we first identify the nanodot peaks and obtain the (x, y) coordinates of these peaks. Let m be the number of points obtained and call the points $\boldsymbol{q}_i$ for $i = 1, ..., m$. From this set of points, we construct the Voronoi tessellation — this partitions the plane in way such that each $\boldsymbol{q}_i$ lies within the polygon consisting of all points closer to $\boldsymbol{q}_i$ than to any $\boldsymbol{q}_j$ with $j \neq i$. The number of polygons in the tessellation with n sides will be denoted by $\Lambda(n)$. Thus, $\Lambda(n)$ is the number of points $\boldsymbol{q}_i$ with n nearest neighbors and will be referred to as the nearest-neighbor distribution. For a perfectly hexagonal lattice, the mean and variance of the nearest-neighbor distribution are exactly six and zero, respectively. Thus, to quantify hexagonal order, we will compute the mean and variance of $\Lambda(n)$ and compare them to these numbers.

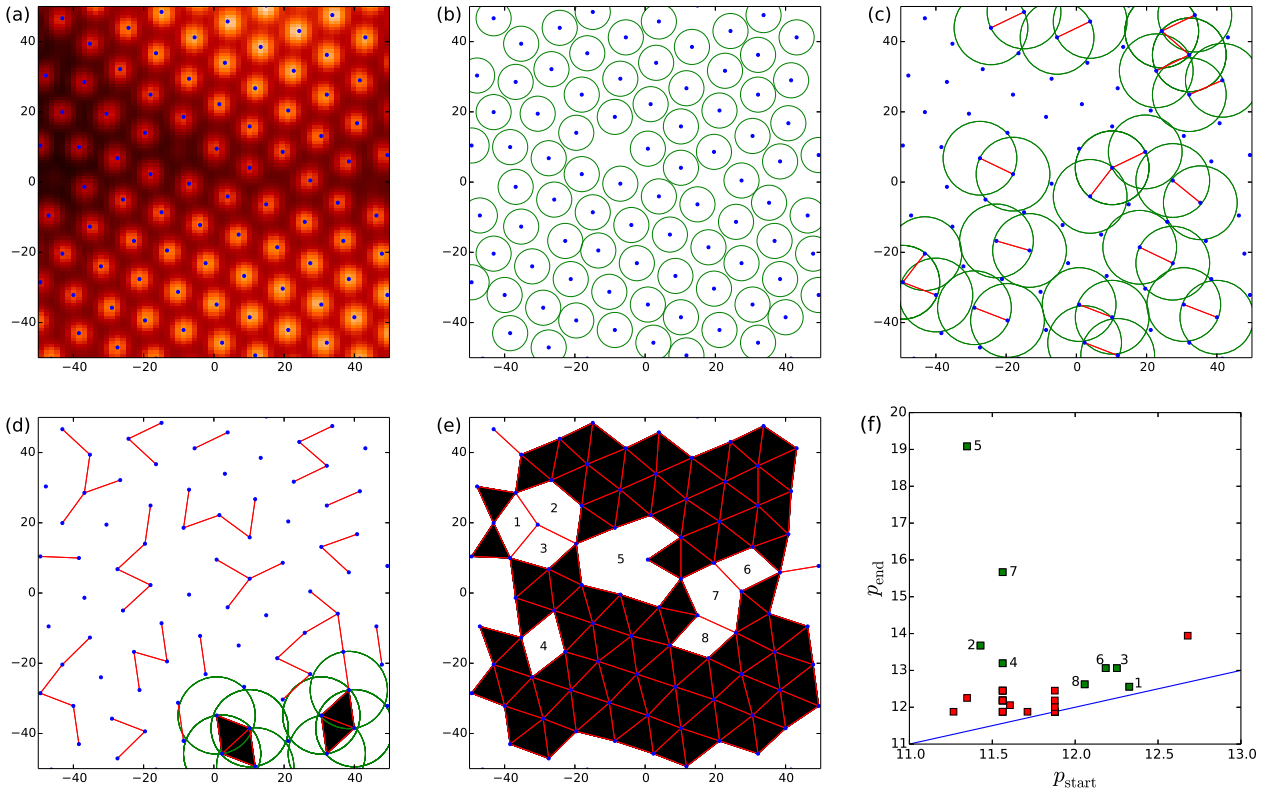

Figure 1.15: **(a)** A section of the simulation result shown in Fig. 3.2 with blue dots indicating the nanodot peaks. **(b)** Around each peak, a circle of radius $p = 5$ has been drawn. **(c)** The connectivity parameter p has increased to 10.5 and red edges have been placed between the centers of circles that enclose each other's centers. Only the circles that enclose each other's centers are shown for clarity. **(d)** When $p = 11$, there are four filled in triangles where three circles all enclose each other's centers. Only the circles related to the filled in faces are shown. **(e)** When $p = 12.5$, many faces have been filled in and holes have emerged. The 8 white polygonal regions with red edge boundaries are identified as holes at this value of p. **(f)** A plot of p_{end} versus p_{start} for the holes found by our persistent homology analysis of (a). The green (red) squares are holes that are present (absent) in (e), and the blue diagonal is the line $p_{\mathrm{end}} = p_{\mathrm{start}}$. A square's vertical distance above the blue line is the corresponding hole's persistence interval length.

Chapter 2

Theory of Terracing of Ion Bombarded Solid Surfaces

Consider a nominally flat elemental solid surface that is bombarded with a broad ion beam at an oblique angle of incidence. If there is an instability, then at early times the surface is governed by the linear BH equation of motion to a good approximation, and ripples form with amplitude that grows exponentially in time. However, nonlinear effects must be taken into account once the ripple amplitude has become sufficiently large. The lowest order nonlinearities are quadratic and come from the angular dependence of the sputter yield [22, 40]. When these terms are included, the equation of motion for the surface becomes the anisotropic Kuramoto-Sivashinsky (KS) equation that was discussed in Section 1.2.2. This equation yields disordered ripples whose amplitude saturates at sufficiently long times.

The anisotropic KS equation does not produce terraced topographies. However, Pearson and Bradley (PB) recently introduced a model that includes a better approximation to the sputter yield than the one that is used in deriving the KS equation [32]. This more refined approximation yields a cubic nonlinearity that does not appear in the KS equation. Numerical integrations of the PB equation of motion reveal that the cubic term can have a profound effect on the dynamics — it can lead to the formation of a terraced topography that coarsens with time, in accord with experimental observations [2, 4, 9–12, 24–28, 30, 59]. The regions in which the surface slope changes rapidly are undercompressive shocks [51].

We next study an equation of motion that generalizes the PB equation to the case in which the surface height can vary in both the transverse and longitudinal directions. This extended equation of motion produces terraced ripple morphologies that undergo interrupted coarsening, just as the PB equation does. For different ranges of the parameters, it yields other topographies that are remarkably similar to those seen in experiments. For example, for a certain range of the parameters,

the extended equation of motion produces pyramidal structures that protrude from the surface and that are elongated in the projected ion beam direction. Analogous topographies were observed by Carter *et al.* when they bombarded a silicon sample with a 40 keV argon ion beam with a 70° angle of incidence [10]. Teichmann *et al.*, on the other hand, bombarded silicon with xenon ions that had an energy of 1.2 keV and a 75° angle of incidence [12]. The isolated lens-shaped depressions they observed are very similar to structures found in numerical integrations of our extended equation of motion.

2.1 Equation of Motion

Consider an initial surface that is perturbed slightly from a completely flat state. We define the $x-y$ plane so that the unperturbed surface lies in it. Furthermore, we orient the x axis so that the ion beam direction lies in the positive quadrant of the $x-z$ plane. The angle of incidence θ is the angle that the ion beam makes with the z axis. We will confine our attention to the case in which the target is an elemental material and the beam consists of noble gas ions. We will assume that the target material is amorphous or that a surface layer is amorphized by the impacting ions.

Let $h(x,y,t)$ be the height of the surface above the point (x,y) in the $x-y$ plane at time t. The most widely used equation of motion for the solid surface is

$$h_t = -v_0 + \alpha h_x + \kappa_1 h_{xx} + \kappa_2 h_{yy} - B\nabla^2\nabla^2 h + \lambda_1 h_x^2 + \lambda_2 h_y^2, \tag{2.1}$$

where the coefficients v_0, α, κ_1, κ_2, B, λ_1 and λ_2 depend on the ion species, energy and angle of incidence and on the choice of target material [14, 22, 40]. The term $-v_0$ accounts for the erosion that would be experienced by a perfectly flat surface. We eliminate this term by working in terms of the deviation of surface height from its unperturbed steady state value; that is, we let $u(x,y,t) \equiv h + v_0 t$. The only effect on the dynamics produced by including the term αu_x in Eq. (2.1) is to cause surface features to propagate laterally at a constant velocity of $-\alpha$. Therefore, we can eliminate this term by transforming to a frame of reference that propagates at velocity $-\alpha$

with respect to the lab frame. This is done formally by setting $\tilde{x} \equiv x + \alpha t$ and then dropping the tildes. We will assume that κ_1 and/or κ_2 is negative, so that a flat initial surface is unstable. The equation of motion (2.1) is reduced to the AKS equation (1.23) in this way.

The AKS equation generates ripples with an exponentially growing amplitude at early times. Since the linearized form of the AKS equation is the BH equation, we know from the linear stability analysis performed in Section 1.4 that if $\kappa_1 < \kappa_2$, then the observed pattern at early times is propagating parallel-mode ripples. Conversely, if $\kappa_2 < \kappa_1$, then the observed pattern at early times is stationary perpendicular-mode ripples.

We will assume that $\lambda_1 \lambda_2 > 0$ so that unphysical cancellation modes in which the ripple amplitude grows without limit do not occur [60]. The quadratic nonlinearities in Eq. (1.23) then eventually control the exponential growth, the ripple amplitude saturates, and the surface exhibits spatiotemporal chaos [22]. At any instant during the chaotic behavior, the surface is statistically invariant under the two transformations $x \to -x$ and $y \to -y$. Additionally, the surface does not coarsen according to this model. These observations are significant because experiments carried out at high angles of incidence produce terraced topographies that are not statistically invariant under the transformation $x \to -x$ and that coarsen [2, 4, 9–12, 24–28, 30, 59]. Since the AKS equation fails to reproduce these two important effects, it is insufficient to model the dynamics produced in these experiments.

In this thesis, we investigate the effects of augmenting Eq. (1.23) with cubic nonlinear terms proportional to u_x^3 and $u_x u_y^2$. This yields the EOM

$$u_t = \kappa_1 u_{xx} + \kappa_2 u_{yy} - B\nabla^2\nabla^2 u + \lambda_1 u_x^2 + \lambda_2 u_y^2 + \gamma_1 u_x^3 + \gamma_2 u_x u_y^2. \tag{2.2}$$

The cubic terms in Eq. (2.2) result from expanding the rate the surface recedes to third order in u_x and u_y; as such, Eq. (2.2) applies only so long as the surface slope remains small. Equation (2.2) represents an improvement on the AKS equation (1.23) since only terms of second order in the slope are retained in the derivation of the latter equation.

When an elemental material is bombarded by a beam of noble gas ions, a number of physical effects can influence the surface dynamics. These effects are sputtering, momentum transfer from the incident ions to atoms near the solid surface [61–63], surface diffusion, ion-induced surface viscous flow [64] and ion implantation [65]. The cubic terms in the equation of motion (2.2) do not conserve mass, but momentum transfer, surface diffusion and ion-induced surface viscous flow all do. These effects therefore cannot contribute to the coefficients of the cubic nonlinearities γ_1 and γ_2. This means that sputtering and ion implantation are the only physical effects that can contribute to γ_1 and γ_2. In Ref. 21, Pearson and Bradley found the contribution of sputtering to γ_1, but they did not consider the contribution of ion implantation.

Note that the terms u_x^3 and $u_x u_y^2$ are unchanged by the transformations $y \to -y$ and $u \to u + \text{const.}$, as they must be. However, they are not invariant under the transformation $x \to -x$, and so Eq. (2.2) does not in general produce surface morphologies that are statistically invariant under this transformation. As we shall see, Eq. (2.2) reproduces many features that are observed in experiments in which elemental materials are bombarded with noble gas ions at relatively high angles of incidence, including terraced topographies that are not invariant under the transformation $x \to -x$.

Equation (2.2) reduces to the PB equation of motion if u does not depend on the transverse coordinate y [32]. It has already been studied by Harrison and Bradley for the case in which the initial surface has a periodic height modulation [18]. In this thesis, we will study the complex and intriguing behavior predicted by Eq. (2.2) when the initial surface is nominally flat.

Consider a term in an equation of motion for the surface height u of the form

$$\prod_{j=1}^{n} (\partial_x^{p_j} u)^{q_j} \,, \tag{2.3}$$

where n is a natural number, and p_j and q_j are natural numbers for all $j \in \{1, ..., n\}$. We define the order of the term in Eq. (2.3) to be the integer given by

$$\max p_j + \sum_{j=1}^{n} q_j. \tag{2.4}$$

Equation (2.2) does not include all terms that are of lower order than u_x^3 and $u_x u_y^2$ and that are invariant under the transformations $y \to -y$ and $u \to u + \text{const}$. In particular, it does not include the terms u_x, u_{xxx}, u_{xyy}, $u_x u_{xx}$ and $u_x u_{yy}$. As we have already mentioned, the term proportional to u_x can be eliminated from the EOM by a Galilean transformation and so it is unnecessary to include it. The influence of a term proportional to u_{xxx} has already been investigated in one dimension (1D): it produces a propagating train of solitons if its coefficient is sufficiently large [66]. Soliton trains are not observed in experiments and we are focused on the formation of terraces, and so we will omit the term u_{xxx} in this work. The effect of a term proportional to $u_x u_{xx}$ has been studied in 1D, and it was found that its inclusion leads to the formation of unphysical singularities in finite time [67]. A detailed investigation of the effects of adding the terms u_{xyy} and $u_x u_{yy}$ to the EOM is left for future study.

Castro *et al.* and Muñoz-García *et al.* have demonstrated that adding a term

$$\sum_{i=1}^{2} \sum_{j=1}^{2} K_{i,j} \frac{\partial^2}{\partial x_i^2} \left(\frac{\partial u}{\partial x_j} \right)^2 \tag{2.5}$$

to the AKS equation leads to interrupted coarsening [42–44]. The equation that they obtained for bombardment at normal incidence was discussed in the extended Kuramoto-Sivashinsky part of Section 1.2.2. They have also shown that this term can arise as a result of mass redistribution near the surface of the solid and have given explicit expressions for the parameters $K_{i,j}$. This term will be omitted from our EOM because its effects are already well understood and because it is expected to play a less prominent role in the dynamics for high angles of ion incidence. In addition, it does not break the $x \to -x$ symmetry and so cannot produce asymmetric terraced topographies. Finally, as we shall see, Eq. (2.2) produces interrupted coarsening even though it does not include a term of the form (2.5).

Eq. (2.2) does not take shadowing of the incident ions into account. Shadowing occurs if the surface slope u_x exceeds $\cot\theta$ at any point on the surface. If the nonlinearities do not adequately control the amplitude of the pattern and shadowing does occur, the equation of motion (2.2) no longer applies. In these circumstances, Eq. (2.2) is valid only for sufficiently early times. The same is true of the widely employed AKS equation (1.23), however.

It is important to note that shadowing need not occur even at long times. Indeed, in the careful experiments of Engler *et al.* [59], shadowing did not occur, and nevertheless terracing was observed. Our equation of motion (2.2) applies in just these circumstances. From a mathematical standpoint, shadowing does not occur if the coefficients of the nonlinear terms (λ_1, λ_2, γ_1 and γ_2) are sufficiently large in magnitude.

In order to study Eq. (2.2), we integrated it numerically using the fourth-order Runge-Kutta exponential time-differencing method of Cox and Matthews that was discussed in Section 1.5, starting with small amplitude white noise as the initial condition [53, 54]. This method uses periodic boundary conditions, which best approximate the physical system that is effectively infinitely extended. The linear terms were computed exactly in Fourier space, while the nonlinear terms were evaluated approximately in real space using finite differencing. The finite differences were central differences accurate to second order in the grid spacing. In the case of our simulations in two dimensions (2D), this means that the partial derivative $\frac{\partial u}{\partial x}(x,y)$ was approximated by

$$\frac{u(x+\Delta x,y)-u(x-\Delta x,y)}{2\Delta x}, \tag{2.6}$$

where Δx is the grid spacing. The time step used was Δt was 0.0025 in the 2D simulations, which was sufficiently small to avoid numerical blow up in any of our simulations.

The 2+1 dimensional equation of motion, Eq. (2.2), involves seven parameters, and so it is difficult to characterize the dynamics of the solutions in a simple way. In order to reduce the number of parameters, we begin by considering the evolution of a surface with no transverse variations, $u = u(x,t)$. The 1+1 dimensional EOM is

$$u_t = \kappa u_{xx} - B u_{xxxx} + \frac{1}{2} c_2 u_x^2 + \frac{1}{6} c_3 u_x^3, \tag{2.7}$$

where the we have set $\kappa_1 \equiv \kappa$, $c_2 \equiv 2\lambda_1$ and $c_3 \equiv 6\gamma_1$, because this will result in simpler expressions for formulas that involve these quantities. The coefficients c_2 and c_3 depend on θ and the material parameters in a manner that we will discuss in the following subsection.

Equation (2.7) may be simplified by introducing the dimensionless variables

$$\bar{u} \equiv \frac{c_2}{\kappa} u, \tag{2.8}$$

$$\bar{x} \equiv \operatorname{sgn}(c_3) \sqrt{\frac{|\kappa|}{B}} x, \tag{2.9}$$

and

$$\bar{t} \equiv \frac{\kappa^2}{B} t. \tag{2.10}$$

After dropping the bars, the equation of motion becomes

$$u_t = -u_{xx} - u_{xxxx} - \frac{1}{2} u_x^2 + \frac{1}{6} \gamma u_x^3, \tag{2.11}$$

where

$$\gamma \equiv \frac{|c_3 \kappa^{3/2}|}{c_2^2 \sqrt{B}} \tag{2.12}$$

is a non-negative, dimensionless parameter.

2.1.1 Nonlinear Coefficients

In order to obtain the coefficients c_2 and c_3, it is sufficient to consider the time evolution of a planar surface with small slope h_x. The local angle of incidence θ_{local} is the angle between the vector $\hat{\mathbf{e}}$ and the surface normal $\hat{\mathbf{n}} \equiv (\hat{\mathbf{z}} - h_x \hat{\mathbf{x}})/\sqrt{1 + h_x^2}$; thus,

$$\cos\theta_{\text{local}} = \hat{\mathbf{n}} \cdot \hat{\mathbf{e}} = \frac{\cos\theta - h_x \sin\theta}{\sqrt{1 + h_x^2}}. \tag{2.13}$$

Expanding $\theta_{\rm local}$ to cubic order in h_x, we obtain

$$\theta_{\rm local} \cong \theta + h_x - \frac{1}{3}h_x^3. \tag{2.14}$$

The rate of erosion due to sputtering is

$$\begin{aligned} h_t &= -\Omega J\sqrt{1+h_x^2}Y(\theta_{\rm local})\cos(\theta_{\rm local}) \\ &= -\Omega J(\cos\theta - h_x\sin\theta)Y(\theta_{\rm local}), \end{aligned} \tag{2.15}$$

where Ω is the atomic volume and we remind the reader that J is the incident ion flux. Expanding to third order in h_x, we find that

$$h_t \cong -v_0 - Ah_x + \frac{c_2}{2}h_x^2 + \frac{c_3}{6}h_x^3, \tag{2.16}$$

where the coefficients are given by

$$v_0 = \Omega J Y(\theta)\cos\theta, \tag{2.17}$$

$$A = \Omega J\left[Y'(\theta)\cos\theta - Y(\theta)\sin\theta\right] = v_0'(\theta), \tag{2.18}$$

$$c_2 = \Omega J\left[2Y'(\theta)\sin\theta - Y''(\theta)\cos\theta\right], \tag{2.19}$$

$$\begin{aligned} c_3 &= \Omega J\left\{3Y''(\theta)\sin\theta + [2Y'(\theta) - Y'''(\theta)]\cos\theta\right\} \\ &= c_2'(\theta), \end{aligned} \tag{2.20}$$

and the primes denote differentiation with respect to θ. Interestingly, $c_3(\theta)$ is exactly the first derivative of c_2 with respect to θ.

To get an idea of how c_3 depends on θ, let us consider the erosion of a silicon sample by a beam of $1\,{\rm keV}$ Ar^+ ions. Following Madi *et al.* [68], we employ the Yamamura-corrected sputter yield $Y(\theta) \equiv Y_0\sec^f(\theta)\exp\left(-\Sigma(\sec\theta - 1)\right)$, where $Y_0 \equiv 0.93$, $\Sigma \equiv f\cos\theta_{\rm opt}$, $\theta_{\rm opt} \cong 1.21$, $f \equiv 1.85[1 + 1.25(1-\xi)/\xi]$, $\xi \equiv 1 - \sqrt{E_{\rm th}/E}$, $E_{\rm th} \equiv 33\,{\rm eV}$, and $E \equiv 1\,{\rm keV}$. (The Yamamura

correction ensures that the sputter yield decreases at sufficiently high angles of incidence, as observed experimentally.) A plot of c_3 versus θ is shown in Figure 2.1. Notice that the magnitude of c_3 is largest when the ion beam is near grazing incidence and so the cubic nonlinearity takes on its most important role in that regime. This regime is also the one in which terracing is most commonly observed in experiments.

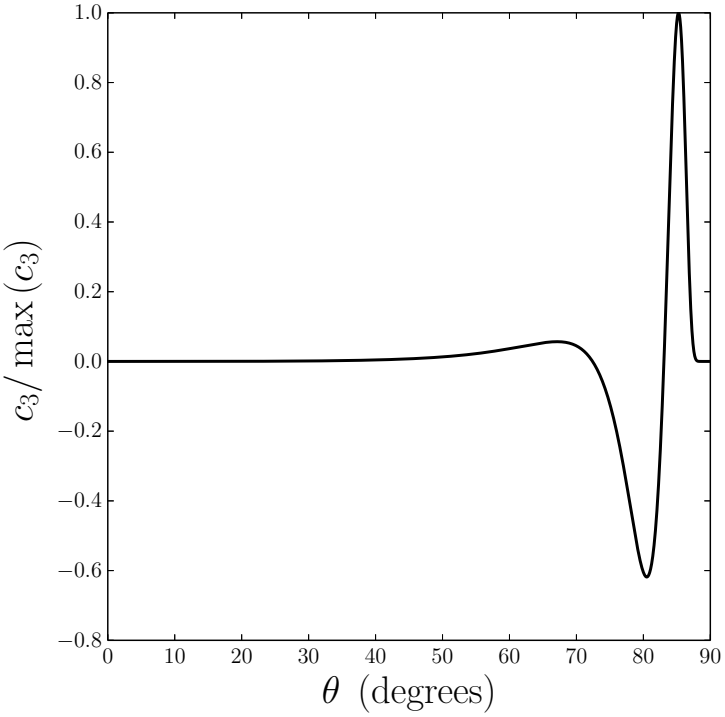

Figure 2.1: A plot of $c_3(\theta)/\max(c_3)$ versus the angle of incidence θ for bombardment of silicon with a 1 keV Ar^+ ion beam.

2.2 Numerical Methods

The surface is taken to be initially flat with small amplitude Gaussian white noise, and periodic boundary conditions are assumed to reduce finite size effects. Since the solutions are then spatially periodic, a natural approach to integrating (2.11) is the Galerkin method with complex exponentials as the basis functions [69]. On the domain $-L \leq x \leq L$, define

$$\phi_n(x) \equiv \exp\left(\frac{\mathrm{i}\pi n x}{L}\right), \tag{2.21}$$

where n is an arbitrary integer. The exact solution to the equation of motion (2.11) with periodic boundary conditions can be written

$$u(x,t) = \sum_{n=-\infty}^{\infty} a_n(t)\phi_n(x), \tag{2.22}$$

where the time-dependent Galerkin coefficients $a_n(t)$ are determined as follows. First, we insert Eq. (2.22) into the equation of motion (2.11). Next, we use the orthogonality of the basis functions to simplify the resulting equation; multiplying both sides by ϕ_m^* and then integrating over the domain $-L \leq x \leq L$ yields

$$\begin{aligned}\frac{\mathrm{d}a_m}{\mathrm{d}t} &= \left[\left(\frac{\pi m}{L}\right)^2 - \left(\frac{\pi m}{L}\right)^4\right] a_m \\ &\quad + \frac{1}{2}\left(\frac{\pi}{L}\right)^2 \sum_{j,n=-\infty}^{\infty} jn a_j a_n \delta_{j+n,m} \\ &\quad - \mathrm{i}\frac{\gamma}{6}\left(\frac{\pi}{L}\right)^3 \sum_{j,\ell,n=-\infty}^{\infty} j\ell n a_j a_\ell a_n \delta_{j+\ell+n,m}.\end{aligned} \tag{2.23}$$

Solving Eq. (2.23) would determine the time evolution of the values of the Galerkin coefficients $a_n(t)$ exactly. However, since we cannot solve this system of infinitely many coupled ODEs, we must truncate the sum in Eq. (2.22). The truncated sum

$$u(x,t) \cong \sum_{n=-N}^{N} a_n(t)\phi_n(x). \tag{2.24}$$

has $2N+1$ terms and yields an approximation to the exact solution. Using the truncated sum Eq. (2.24) and eliminating all Kronecker deltas appearing in Eq. (2.23), we obtain the system of ODEs that we will solve numerically:

$$\begin{aligned}\frac{\mathrm{d}a_m}{\mathrm{d}t} \;\cong\; & \left[\left(\frac{\pi m}{L}\right)^2 - \left(\frac{\pi m}{L}\right)^4\right] a_m \\ & + \frac{1}{2}\left(\frac{\pi}{L}\right)^2 \sum_{n=-N}^{N} n(m-n) a_n a_{m-n} \\ & - \mathrm{i}\frac{\gamma}{6}\left(\frac{\pi}{L}\right)^3 \sum_{j,n=-N}^{N} jn(m-j-n) a_j a_n a_{m-j-n},\end{aligned} \tag{2.25}$$

where $m \in \{-N, -N+1, ..., N-1, N\}$ and $a_n = 0$ for $|n| > N$. A variable-coefficient ordinary differential equation solver was implemented with Python to integrate these ODEs. In all simulations shown in this work, a half interval length of $L = 250$ is used so that the wavelength λ_c selected by linear stability analysis of equation of motion (2.11) is small compared to the domain length. Since $\lambda_c = 2\sqrt{2}\pi$, about 56 selected wavelengths are expected to be seen during the linear regime of the evolution of the surface height. This means that a reasonable physical scale for L is about several hundred nanometers. Furthermore, in the simulations we used $N = 1000$ to ensure there was a sufficient number of Galerkin coefficients to obtain accurate solutions. Figure 2.2 confirms the validity of using the truncated sum with $N = 1000$ in our numerical method because the Galerkin coefficients' magnitudes decrease roughly exponentially as the Galerkin index m increases.

2.2.1 Determination of the Ripple Propagation Velocity

The method we used to calculate the ripple propagation velocity from our numerical results is conceptually simple: determine the spatial translation Δx that minimizes the difference between the height functions of two consecutive time steps t_1 and t_2. Once Δx has been found, the propagation velocity s is determined by

$$s = \frac{\Delta x}{\Delta t}, \tag{2.26}$$

where $\Delta t \equiv t_2 - t_1$ is the time interval between consecutive time steps. Consider the Galerkin expansion of the height $u(x,t)$ on the domain $-L \leq x \leq L$ at a particular time step t_1,

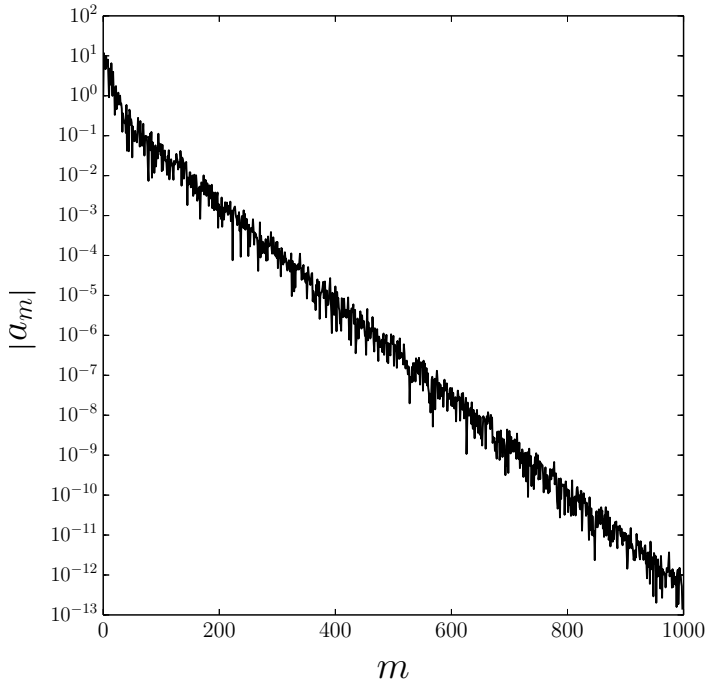

Figure 2.2: The Galerkin coefficient magnitude $|a_m|$ versus the coefficient index m for a simulation of the equation of motion (2.11) with $\gamma = 0.7$ at time $t = 1000$. The data point for $m = 0$ has been omitted.

$$u_1 \equiv u(x, t_1) \equiv \sum_{n=-N}^{N} a_n(t_1) \mathrm{e}^{\mathrm{i}\pi n x/L} \tag{2.27}$$

and the expansion of $u(x + \Delta x, t)$ at the following time step $t_2 = t_1 + \Delta t$,

$$u_2 \equiv u(x + \Delta x, t_2) \equiv \sum_{n=-N}^{N} a_n(t_2) \mathrm{e}^{\mathrm{i}\pi n(x+\Delta x)/L}. \tag{2.28}$$

Since u_1 and u_2 are both real, the difference between u_1 and u_2 is minimized when

$$M(\Delta x) \equiv \int_{-L}^{L} (u_2 - u_1)^2 \, \mathrm{d}x \tag{2.29}$$

is minimized with respect to Δx. Inserting the Galerkin expansions of u_1 and u_2 into Eq. (2.29) and carrying out the integral yields

$$M(\Delta x) = 2L \sum_{n=-N}^{N} \{|a_n(t_1)|^2 + |a_n(t_2)|^2 - [a_{-n}(t_1)\, a_n(t_2)\, \mathrm{e}^{\mathrm{i}\pi n \Delta x/L} + \text{c.c.}]\}, \tag{2.30}$$

where "c.c." is an abbreviation for complex conjugate. Thus, using the Galerkin coefficients found by numerically integrating the equation of motion (2.11) and a minimizing algorithm, we can determine the propagation velocity s of the surface ripple.

2.3 Terracing Simulation Results: 1+1 dimensions

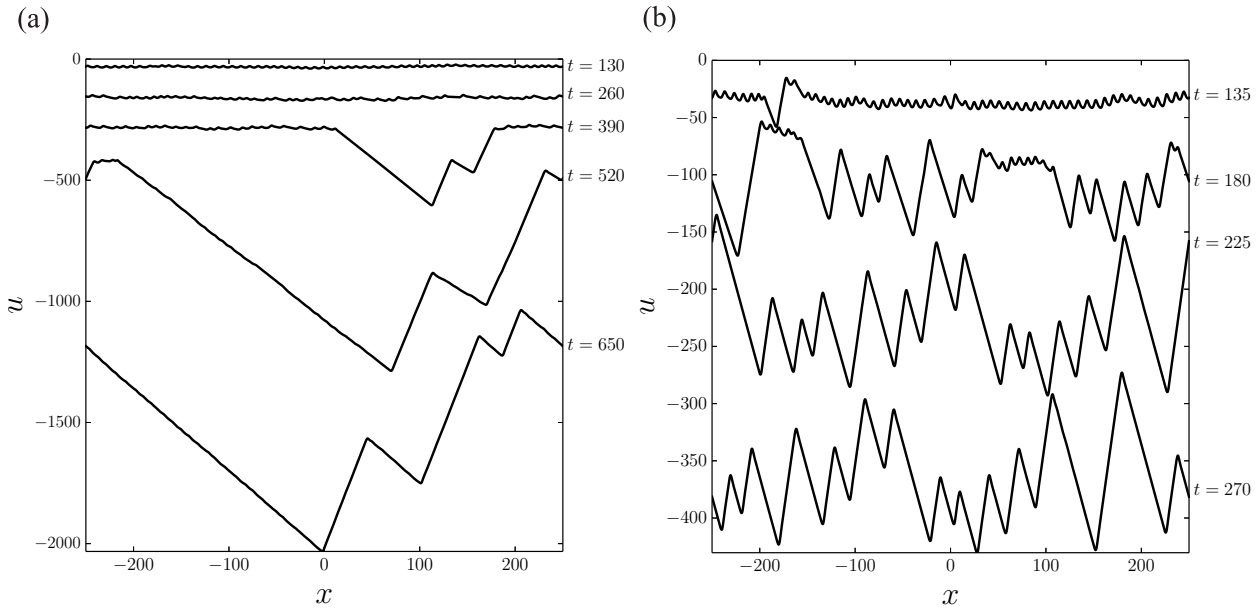

Figure 2.3: Plots of u versus x at the equally spaced times shown, produced by integrating the equation of motion (2.11). The time for each curve is to the right of the plots. (a) $\gamma = 0.3$. (b) $\gamma = 0.7$.

In this section, we will discuss the results of numerical integrations of Eq. (2.11) with an emphasis on the development of terraced surfaces. Additional numerical results — including our results on the ripple propagation velocity — will be given in Section 2.4 once we have developed the analytical results needed to understand them.

The results of two numerical integrations of the equation of motion (2.11) with differing values of γ and a nominally flat initial condition are shown in Figure 2.3. For both $\gamma = 0.3$ and $\gamma = 0.7$, a terraced topography develops in which two selected slopes are readily apparent. Figure 2.4, which

shows the distribution of slopes obtained for a simulation with $\gamma = 0.7$, has two sharp peaks by time $t = 1000$. Figure 2.3 demonstrates that the selected slopes depend on γ.

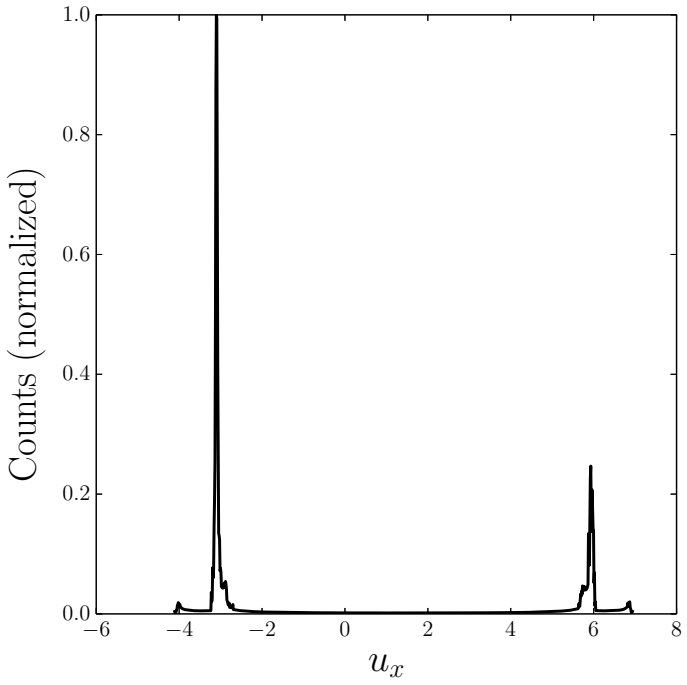

Figure 2.4: The slope distribution (normalized counts versus u_x) for a simulation with $\gamma = 0.7$ at time $t = 1000$.

All the simulations we carried out with $\gamma \geq 0.28$ yielded terraced topographies by the time $t = 10^3$. These terraced structures slowly coarsened with time and propagated to the left. In contrast, for smaller values of γ, the behavior we observed was “KS-like" in that the ripple amplitude saturated, selected slopes did not develop, the surface appeared to exhibit spatiotemporal chaos, and the characteristic length scale did not increase appreciably. For small values of γ, we cannot analytically rule out a crossover to a terraced topography at long times. A simulation with $\gamma = 0.26$ did not produce any terraces after integrating to time $t = 4 \times 10^4$, however.

We define the surface width

$$\sigma(t) \equiv \sqrt{\langle u^2(t) \rangle - \langle u(t) \rangle^2}, \tag{2.31}$$

to be the root-mean-square deviation of u from its spatial average, where $\langle f(t) \rangle$ denotes the spatial average of the function $f = f(x,t)$ at time t. Naturally, for all values of γ, the time evolution begins with a linear regime, during which the surface width σ increases exponentially with time. The time dependence of σ is shown in Figure 2.5 for the simulations with $\gamma = 0.3$ and $\gamma = 0.7$. The exponential growth of $\sigma(t)$ at times less than about 100 is evident in the inset of Figure 2.5(b).

When the ripple amplitude becomes comparable to the wavelength, nonlinear effects begin to play an important role in the dynamics. In our simulations with γ values between roughly 0.28 and 0.5, we observed a period of KS-like behavior after the linear regime. During this time interval, the surface width was approximately constant; this behavior occurred between about $t = 100$ and $t = 300$ in the simulation shown in Figure 2.5(a). Terrace formation then sets in. For γ values greater than about unity, on the other hand, the system seems to make the transition from the linear to the terrace forming regime directly, without passing through an intermediate KS-like regime. Once terraces have formed, they undergo interrupted coarsening: the surface width σ grows in a roughly linear fashion for some time and then levels off.

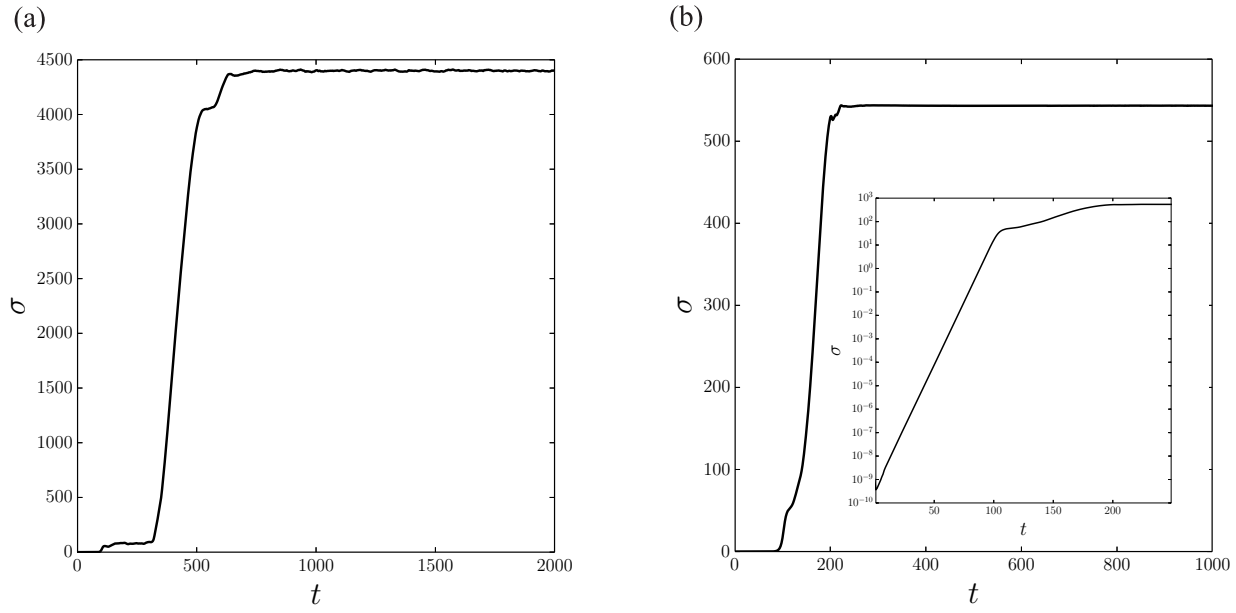

Figure 2.5: Surface width σ versus time t for (a) a simulation with γ=0.3 and (b) a simulation with $\gamma = 0.7$. The inset in (b) is plotted on a semilog scale to exhibit the exponential growth of σ at the early times.

2.4 Terrace Slope Selection

In this section, we will apply two transformations in order to reduce the equation of motion (2.11) to an equation with no free parameters. Ultimately, these transformations will allow us to predict the behavior of the surface at late times.

First, by using an appropriate invertible point transformation, the quadratic nonlinearity can be removed from Eq. (2.11), yielding a simpler equation of motion. Henceforth, we will refer to Eq. (2.11) as the untransformed equation of motion and $u = u(x,t)$ as the untransformed height. Let

$$P(x,t) \equiv \sqrt{\frac{\gamma}{6}} \left[u(x,t) - \frac{1}{\gamma}\, x + \frac{1}{3\gamma^2}\, t \right] \tag{2.32}$$

be the transformed height corresponding to $u(x,t)$. Applying the transformation given by Eq. (2.32) to the untransformed equation of motion (2.11) yields

$$P_t = -P_{xx} - P_{xxxx} + P_x^3 - \frac{1}{2\gamma} P_x. \tag{2.33}$$

The term proportional to P_x can be eliminated by transforming to a moving frame of reference. Let $\tilde{x} \equiv x - t/(2\gamma)$ and $\tilde{t} \equiv t$. Equation (2.33) then reduces to a partial differential equation with no quadratic nonlinearity and with no free parameters:

$$P_{\tilde{t}} = -P_{\tilde{x}\tilde{x}} - P_{\tilde{x}\tilde{x}\tilde{x}\tilde{x}} + P_{\tilde{x}}^3 \tag{2.34}$$

or, equivalently,

$$p_{\tilde{t}} = -p_{\tilde{x}\tilde{x}} - p_{\tilde{x}\tilde{x}\tilde{x}\tilde{x}} + \partial_{\tilde{x}} p^3, \tag{2.35}$$

where $p(\tilde{x},\tilde{t}) \equiv P_x(\tilde{x},\tilde{t})$ will be called the transformed slope.

Motivated by the appearance of traveling wave solutions in the simulation results at late times, we seek solutions for which the untransformed height takes the form

$$u(x,t) = w(x - st) - \mu t, \tag{2.36}$$

where s is the propagation velocity in the x direction and μ is the downward drift speed. The corresponding ansatz for the transformed slope is

$$p(\tilde{x}, \tilde{t}) = q(\tau), \tag{2.37}$$

where $q(\tau) \equiv \sqrt{\gamma/6}\,[\phi(\tau) - 1/\gamma]$, $\tau \equiv \tilde{x} - s_{\rm tr}\,\tilde{t}$, $\phi(\tau) \equiv w'(\tau)$ is the untransformed slope, and $s_{\rm tr}$ satisfies

$$s = s_{\rm tr} + \frac{1}{2\gamma}. \tag{2.38}$$

A solution for the transformed slope of the form given by Eq. (2.37) is a traveling wave that has the propagation velocity $s_{\rm tr}$ in the moving frame of reference.

Inserting the ansatz (2.37) into the transformed equation of motion (2.35) and integrating once yields the following ODE:

$$q''' = -q' + q^3 + s_{\rm tr}\,q + \mu_{\rm tr}. \tag{2.39}$$

Here the primes indicate differentiation with respect to τ and $\mu_{\rm tr}$ is a constant of integration. We will seek shock wave solutions to Eq. (2.35); i.e., we will look for solutions to Eq. (2.39) that asymptote to constants as $\tau \to \pm\infty$. If $q(\tau) \to q_\pm$ as $\tau \to \pm\infty$, then Eq. (2.39) shows that q_+ and q_- must be roots of the cubic

$$q^3 + s_{\rm tr}\,q + \mu_{\rm tr} = 0. \tag{2.40}$$

Clearly, if Eq. (2.35) has the solution $p(\tilde{x}, \tilde{t})$, then $-p(\tilde{x}, \tilde{t})$ is a solution as well. As a consequence, if $q(\tau)$ is a solution of Eq. (2.39), then $-q(\tau)$ must be also be a solution to this equation. This leads us to the conclusion that

$$\mu_{\rm tr} = 0. \tag{2.41}$$

The roots of the cubic Eq. (2.40) are therefore $q_{-1} \equiv -\sqrt{-s_{\rm tr}}$, $q_0 \equiv 0$, and $q_{+1} \equiv +\sqrt{-s_{\rm tr}}$. Any shock wave solution $q(\tau)$ must asymptote to one of these transformed slopes as $\tau \to -\infty$ and to a different one as $\tau \to +\infty$. Because q is real, this is only possible if $s_{\rm tr}$ is negative. We will assume that this is the case in what follows. The validity of this assumption is supported by our numerical

integrations of the equation of motion (2.11), which yield negative values of s. Equation (2.38) shows that the corresponding values of $s_{\rm tr}$ are negative as well.

Equation (2.39) can be recast as a system of three first order ODEs by setting $X_1 \equiv q(\tau)$, $X_2 \equiv q'(\tau)$, and $X_3 \equiv q''(\tau)$. Recalling that $\mu_{\rm tr} = 0$, we obtain

$$\begin{aligned} X_1' &= X_2 \\ X_2' &= X_3 \\ X_3' &= -X_2 + X_1^3 + s_{\rm tr}\, X_1. \end{aligned} \tag{2.42}$$

Let $\mathbf{X} \equiv (X_1, X_2, X_3)$ be a point in the phase space with coordinates X_1, X_2 and X_3. The system of ODES (2.42) has the three fixed points $\mathbf{X}_{-1} \equiv (q_{-1}, 0, 0)$, $\mathbf{X}_0 \equiv (q_0, 0, 0)$, and $\mathbf{X}_{+1} \equiv (q_{+1}, 0, 0)$ with the transformed slope values q_{-1}, q_0 and q_{+1}, respectively. In this formulation, a shock wave is represented by a trajectory in the three dimensional phase space that begins at one of the fixed points at $\tau = -\infty$ and that asymptotes to a different fixed point at $\tau = +\infty$. Such a trajectory is known as a heteroclinic orbit.

In the heteroclinic orbit, as τ is increased from $-\infty$, the phase point $\mathbf{X}(\tau)$ at first moves very slowly away from the initial fixed point $\mathbf{X}_-$. Its motion then accelerates for a time before an increasingly slow approach to the final fixed point $\mathbf{X}_+$ sets in. The q values associated with the fixed points $\mathbf{X}_+$ and $\mathbf{X}_-$ are the selected slopes for the transformed equation of motion (2.35). These must be transformed back to the untransformed problem using Eq. (2.32) to obtain the selected slopes for the equation of motion (2.11) that governs the behavior of the solid surface.

We may readily take the results of a numerical integration of Eq. (2.11) and compute $P(x,t)$ using Eq. (2.32). When the resulting $P(x,t)$ is plotted as a function of x for long times t and for $\gamma > 0.28$, a sawtooth form with *symmetric* teeth is obtained. This indicates that the selected values of the transformed slopes are $\pm\sqrt{|s_{\rm tr}|}$. As a consequence, the heteroclinic orbits are trajectories from $\mathbf{X}_{-1}$ to $\mathbf{X}_{+1}$ and vice versa. A trajectory from $\mathbf{X}_{-1}$ to $\mathbf{X}_{+1}$ and back again is called a heteroclinic cycle.

The fact that only two selected slopes appear in our simulations strongly suggests that there is a single allowed value of $s_{\rm tr}$. If this is so, then there is a heteroclinic cycle that passes through both $\mathbf{X}_{-1}$ and $\mathbf{X}_{+1}$ for this particular value of $s_{\rm tr}$ and for no others.

Repeating our traveling wave analysis on the untransformed equation of motion (2.11), we obtain a system of three ODEs with three fixed points. The slopes ϕ associated with these fixed points satisfy the cubic

$$\gamma\phi^3 - 3\phi^2 + 6s\phi + 6\mu = 0. \tag{2.43}$$

Equation (2.32) shows that the untransformed slope corresponding to $q_0 = 0$ is $\phi_0 = 1/\gamma$. This value of ϕ must be a solution of Eq. (2.43). As a consequence, the untransformed downward drift rate and propagation velocity are related by

$$\mu = \frac{1}{3\gamma^2} - \frac{s}{\gamma}. \tag{2.44}$$

Using Eq. (2.38), the downward drift speed can be written in terms of the transformed propagation velocity as

$$\mu = -\frac{1}{6\gamma^2} - \frac{s_{\rm tr}}{\gamma}. \tag{2.45}$$

Differentiating Eq. (2.32) with respect to x, we find that

$$\phi = \frac{1}{\gamma} + \sqrt{\frac{6}{\gamma}}p. \tag{2.46}$$

The roots of the cubic in Eq. (2.43) are obtained by setting p equal to q_{-1}, q_0 and q_{+1} in this result. Explicitly, the roots are

$$\phi_{\pm 1} = \frac{1}{\gamma} \pm \sqrt{\frac{6\,|s_{\rm tr}|}{\gamma}} \tag{2.47}$$

and

$$\phi_0 = \frac{1}{\gamma}. \tag{2.48}$$

Note that ϕ_{+1} and ϕ_{-1} are the selected slopes for the untransformed problem.

Equations (2.38), (2.45) and (2.47) show that once we have determined the value of $s_{\rm tr}$, we will have the shock propagation velocity s, the downward drift rate μ, and the selected slopes ϕ_{+1} and ϕ_{-1}. Moreover, we will have these quantities for all positive values of γ. Accordingly, we will now turn to the task of computing $s_{\rm tr}$.

We used the shooting method to find an approximate value of $s_{\rm tr}$. In particular, we integrated the system of ODEs given by Eq. (2.42) numerically for varying values of $s_{\rm tr}$ with an initial condition displaced from $\mathbf{X}_{-1}$ by a small distance in the direction along the unstable eigenvector of the linearized flow near that fixed point. We found a single value of $s_{\rm tr}$ that yielded a trajectory that passed close to $\mathbf{X}_{+1}$, in accord with what we expected based on our numerical integrations of the untransformed equation of motion (2.11). The value of $s_{\rm tr}$ that we adopted as our estimate is

$$s_{\rm tr} \approx -2.387\,962\,295\,205. \tag{2.49}$$

This value produced a trajectory that came within a distance of 5.11×10^{-3} of the point $\mathbf{X}_{+1}$. Our predictions for the terrace properties given by Eqs. (2.38), (2.45) and (2.47) are not highly sensitive to the value of $s_{\rm tr}$; however, the trajectory obtained by integrating Eq. (2.42) is sensitive to its value. The approximate heteroclinic trajectory yielded by the shooting method was transformed back to the untransformed problem for the case $\gamma = 0.7$ and is plotted in Figure 2.6. Also shown is the result obtained by numerical integration of the equation of motion (2.11) with $\gamma = 0.7$. The agreement between the two results is very good.

Now that we have found the approximate value of $s_{\rm tr}$, we can determine the shock propagation velocity s, the downward drift velocity μ, and the selected slopes ϕ_{+1} and ϕ_{-1} for the untransformed equation of motion (2.11). We will compare the values yielded by Eqs. (2.38), (2.45) and (2.47) to results obtained by direct numerical integration of Eq. (2.11) for a range of γ values.

In order to estimate ϕ_{+1} for a simulation with particular value of γ, we first take the solution at time $t = 1000$ and calculate the slope u_x at 10^4 equally spaced position points. We then average over all slopes satisfying $\max(u_x)/2 < u_x < \max(u_x)$ to yield our estimate of ϕ_{+1}. The same approach is used to estimate ϕ_{-1}, except that the slopes must satisfy $\min(u_x) < u_x < \min(u_x)/2$

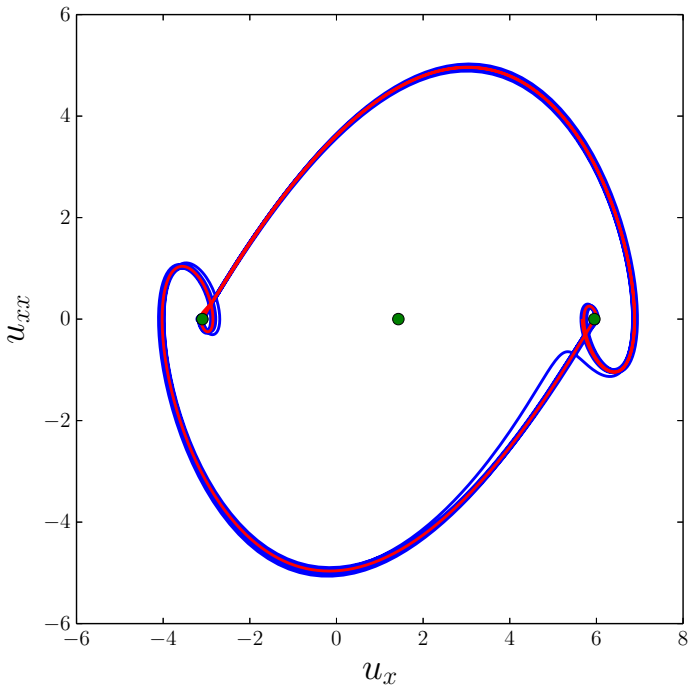

Figure 2.6: The shooting method result transformed back to the untransformed problem for $\gamma = 0.7$ (red) is superimposed upon the result obtained by integrating the equation of motion (2.11) with $\gamma = 0.7$ (blue). The green dots are the fixed points of the equivalent system of ODEs (2.42) transformed back for $\gamma = 0.7$.

in that case. These estimates tend to underestimate the magnitude of the selected slopes $\phi_{\pm 1}$. As shown in Figure 2.7, the selected slopes predicted by Eq. (2.47) are in very good agreement with the estimates obtained from numerical integrations of Eq. (2.11).

The downward drift rate μ is plotted versus γ in Figure 2.8. Since the Galerkin coefficient $a_0(t)$ is the spatial average value of $u(x,t)$, μ was obtained from our simulation results using a linear fit to the form $a_0(t) = -\mu t$ at late times. The agreement with the prediction from Eq. (2.45) is excellent.

A plot of the propagation velocity s versus γ is shown in Figure 2.9. The propagation velocities obtained from numerical simulations of the equation of motion (2.11) were determined using the method described in Section 1.4.2. The results are very close to the values predicted by Eq. (2.38).

In this paragraph, we will use ideas and notation introduced in Section 1.4.2. To see that the shock waves in our model are undercompressive, we note that Eq. (2.35) has the form Eq. (1.35) with the flux $F(p) = -p^3$. For a shock with $q_- = q_{-1} = -\sqrt{|s_{\rm tr}|}$ and $q_+ = q_{+1} = +\sqrt{|s_{\rm tr}|}$,

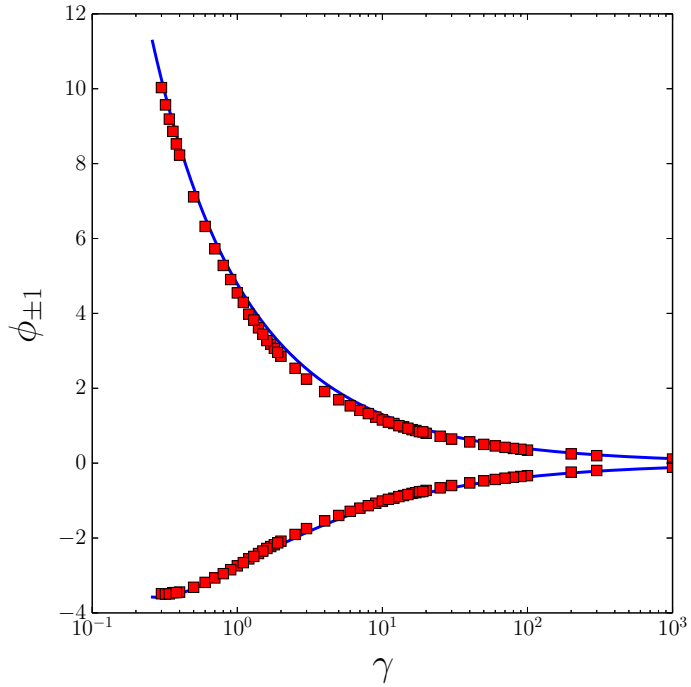

Figure 2.7: The terrace slopes ϕ_{+1} and ϕ_{-1} plotted versus γ. The red squares are the results obtained by integrating the equation of motion (2.11). The blue curves are the predicted slopes obtained from Eq. (2.47).

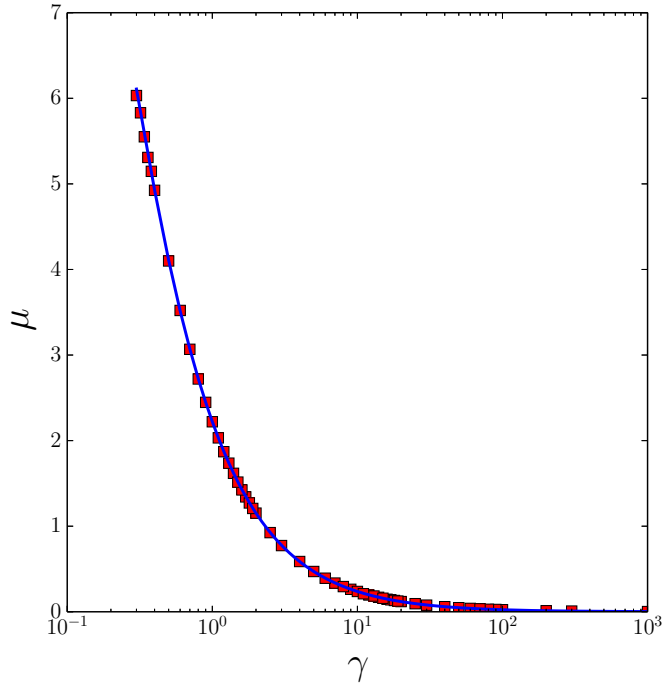

Figure 2.8: The downward drift rate μ plotted versus γ. The red squares are the results obtained by integrating the equation of motion (2.11). The blue curve is the prediction obtained from Eq. (2.45).

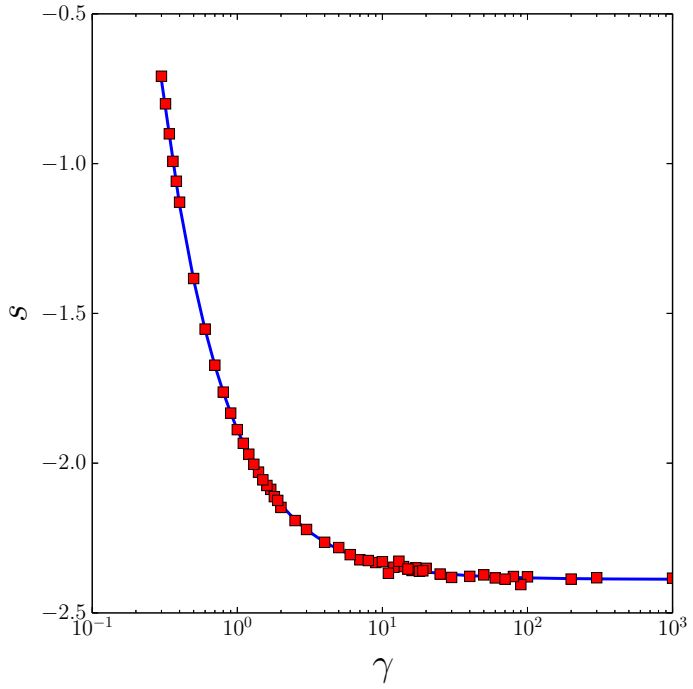

Figure 2.9: The propagation velocity s plotted versus γ. The red squares are the results obtained by integrating the equation of motion (2.11). The blue curve is the prediction obtained from Eq. (2.38).

Eq. (1.38) gives $U = s_{\rm tr}$. Since this is the velocity of the shock, the Rankine-Hugoniot condition is satisfied. However, $F'(q_-) = F'(q_+) = 3s_{\rm tr}$ and so the Lax entropy condition Eq. (1.39) is not satisfied. By definition, therefore, the shock is undercompressive. In the same way, a shock with $q_- = q_{+1} = +\sqrt{|s_{\rm tr}|}$ and $q_+ = q_{-1} = -\sqrt{|s_{\rm tr}|}$ satisfies the Rankine-Hugoniot condition, violates Eq. (1.39) and is undercompressive.

The 1+1 D equation of motion that applies to the original physical problem in the lab frame of reference is

$$h_t = -v_0 - Ah_x + \kappa h_{xx} - Bh_{xxxx} + \frac{1}{2}c_2 h_x^2 + \frac{1}{6}c_3 h_x^3. \tag{2.50}$$

The selected slopes will be denoted by $m_{\pm 1}$ and are given by

$$m_{\pm 1} = -\mathrm{sgn}(c_3)\frac{|\kappa|^{3/2}}{c_2 B^{1/2}}\left(\frac{1}{\gamma} \pm \sqrt{\frac{6\,|s_{\rm tr}|}{\gamma}}\right), \tag{2.51}$$

where γ was defined in Eq. (2.12) and our approximate result for $s_{\rm tr}$ appears in Eq. (2.49). The shock propagation velocity S, on the other hand, is

$$S = A + \mathrm{sgn}(c_3)\frac{|\kappa|^{3/2}}{B^{1/2}}\left(s_{\rm tr} + \frac{1}{2\gamma}\right). \tag{2.52}$$

The net rate of erosion will be defined to be $d\langle h(t)\rangle/dt$ and will be denoted by v. For long times t it is given by

$$v = v_0 + \frac{\kappa^3}{c_2 B}\left(\frac{s_{\rm tr}}{\gamma} + \frac{1}{6\gamma^2}\right). \tag{2.53}$$

The result Eq. (2.52) is particularly interesting. For θ less than a critical value θ_1, the propagation velocity for low amplitude ripples A is positive, which means that the ripples propagate into the ion beam. Let us assume that $\theta < \theta_1$. Equation (2.52) gives the propagation velocity at long times when the surface has a well-developed terrace morphology. It is important to note that S can be *negative*. In particular, this occurs if

$$\frac{B^{1/2}A}{|\kappa|^{3/2}} < \mathrm{sgn}(c_3)\left(|s_{\rm tr}| - \frac{1}{2\gamma}\right). \tag{2.54}$$

If A is positive and S is negative, the linearized theory initially applies and the surface ripple propagates into the ion beam. However, as the ripple amplitude grows, the importance of the cubic nonlinearity increases and the ripple velocity begins to decline. At long times, the surface develops terraces that propagate in the negative x direction, *away* from the ion beam. The propagation direction therefore reverses as time passes [44].

2.5 Terracing Results: 2+1 dimensions

So far, we have studied the solutions to Eq. (2.2) for the special case in which u is independent of the transverse coordinate y, i.e., the 1D case. We will now explore the behavior predicted by Eq. (2.2) when u depends on x, y and t. We will refer to this as the 2D case.

In Section 2.3, we demonstrated that including the cubic nonlinearity u_x^3 in the EOM can lead to terrace formation in 1D, but the question of whether this also holds true in 2D was not addressed. In this section, we present simulation results in 2D that display topographies that are terraced analogs of parallel-mode ripples. In addition, we find that inclusion of the cubic nonlinearities u_x^3 and $u_x u_y^2$ in the EOM can yield surface morphologies that resemble those observed in various experiments. Among these are elongated pyramidal structures [10, 11] and lenticular depressions [12]. We also compare the predictions from the 1D theory with our simulations in 2D when there is smoothing in the transverse direction and find that key predictions from 1D carry over to 2D.

2.5.1 Parallel-Mode Terraces

The most significant effect of including the cubic nonlinearity u_x^3 in the EOM (2.2) is that it can lead to the formation of a terraced topography. The results of a simulation in 2D are shown in Fig. 2.10. The topographies that develop are quite similar to those found in an experiment in which a silicon sample was irradiated with a 60 keV Ar^+ ion beam with a 60° angle of incidence (see Fig. 2.11). In both the experiments and the simulations, terraces develop that resemble parallel-mode ripples, except that the regions between the crests and troughs have nearly constant slope. We call these structures *parallel-mode terraces*, in analogy with parallel-mode ripples. Figure 2.12 shows the mean curvature, which we shall denote by H, for the surface in Figure 2.10 (b); the distinctive nearly vertical dark and light lines are undercompressive shocks that are associated with terrace formation. In between these shocks is a complicated cellular structure of small scale ripples. Small scale ripples are ubiquitous in simulations with $\kappa_1 < 0$ and $\kappa_2 < 0$ once terraces have formed.

From Fig. 2.13 we see that the gradient distribution for Fig. 2.10 (b) (i.e., a 2D histogram of u_x and u_y values) has two preferred values for u_x: this confirms that the surface is indeed terraced. The spread in u_y occurs because of the transverse instability; if κ_2 were positive instead of negative, the gradient distribution would be strongly peaked in the transverse direction at long times.

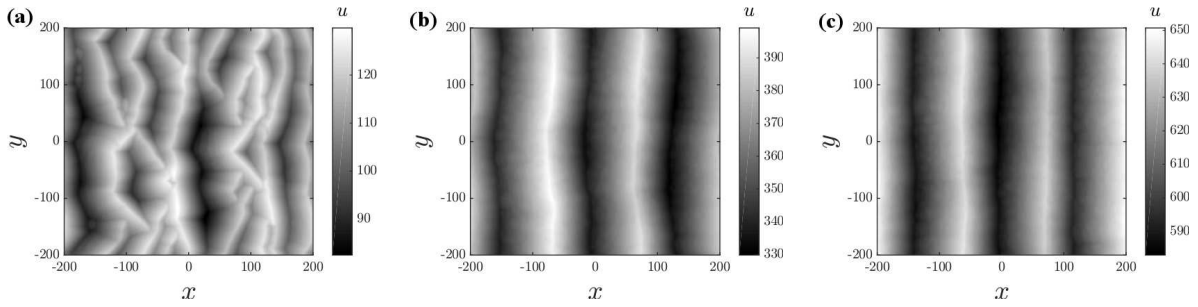

Figure 2.10: The surface height obtained from a simulation of Eq. (2.2) at times (a) $t = 1000$, (b) $t = 3000$ and (c) $t = 5000$. By the end of the simulation, parallel-mode terraces have developed, with slight bends in the terrace edges due to the presence of a transverse instability. The parameter values used were $\kappa_1 = -0.5$, $\kappa_2 = -0.1$, $\lambda_1 = 0.5$, $\lambda_2 = 0.5$, $B = 1$, $\gamma_1 = 1$ and $\gamma_2 = 0$.

2.5.2 Steady-state solutions

In the 1D theory, the terraced solutions are traveling waves that propagate and descend at a constant rate. We assume the same to be true of the terraced solutions to Eq. (2.2). Thus, we seek solutions to Eq. (2.2) of the form $u(x, y, t) = f(x - st, y) - \mu t$, where f is a function that gives the shape of the traveling wave, s is the lateral propagation velocity and μ is the downward drift speed. This yields the following time-independent partial differential equation:

$$\kappa_1 f_{xx} + \kappa_2 f_{yy} - B\nabla^2\nabla^2 f + \lambda_1 f_x^2 + \lambda_2 f_y^2 + \gamma_1 f_x^3 + \gamma_2 f_x f_y^2 + s f_x + \mu = 0. \tag{2.55}$$

Since a terraced surface is dominated by regions of constant slope, we seek solutions in which the surface is flat, i.e., in which $u_{xx} = u_{xy} = u_{yy}$. Thus, we expect that the terraced surfaces' gradient distributions are most heavily weighted at the values of (f_x, f_y) satisfying the algebraic equation

$$\lambda_1 f_x^2 + \lambda_2 f_y^2 + \gamma_1 f_x^3 + \gamma_2 f_x f_y^2 + s f_x + \mu = 0. \tag{2.56}$$

The set of points (f_x, f_y) satisfying Eq. (2.56) is the union of up to three nonintersecting curves. The gradient distributions are concentrated close to two subsets of these curves, as shown in Fig. 2.14 for three different sets of parameter values. This is in direct analogy with the 1D case in

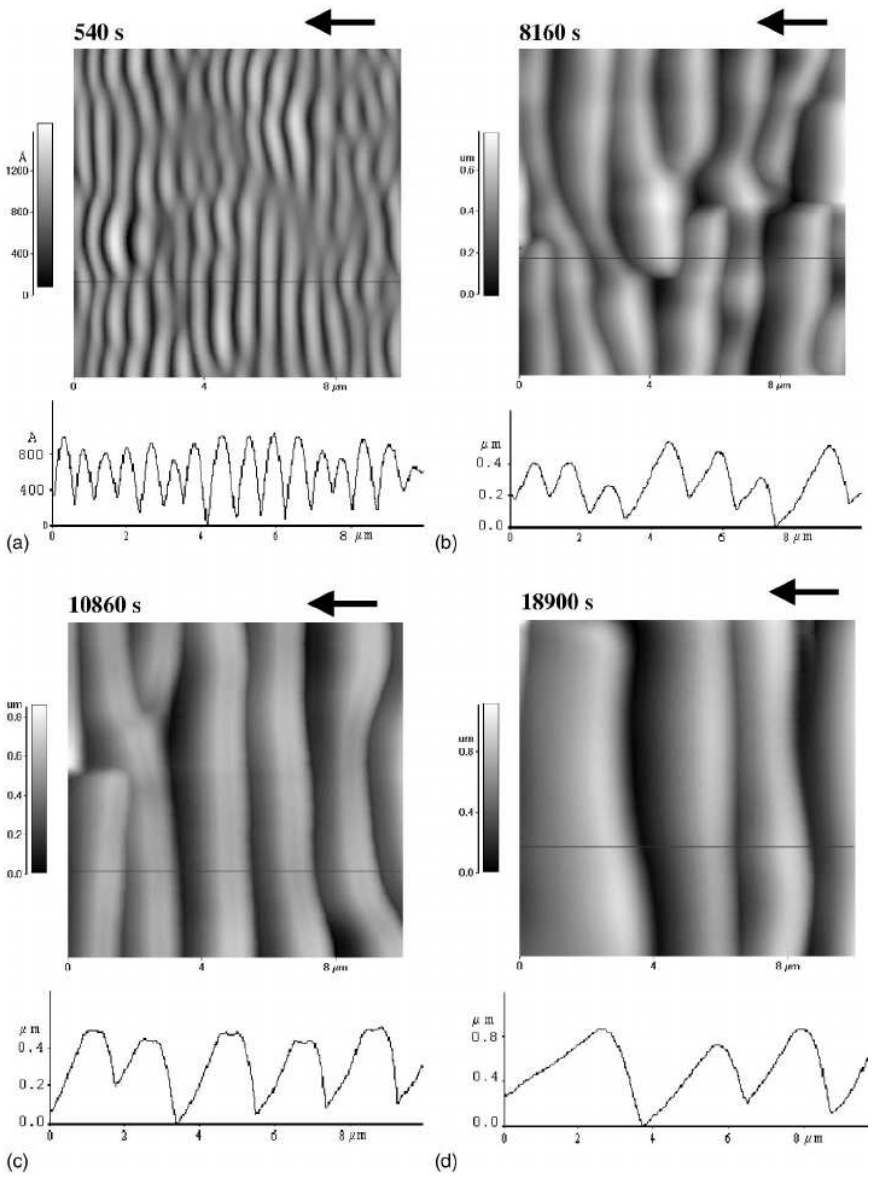

Figure 2.11: A sequence of snapshots of a silicon surface observed by Datta *et al.* The surface was bombarded 60 keV Ar^+ ions at a 60^o angle of incidence. The black arrows indicate the ion beam direction projected onto the surface. Terraces with relatively little transverse variation develop at late times. The surface coarsens laterally and roughens as the terraces form. This figure is from Ref. [9].

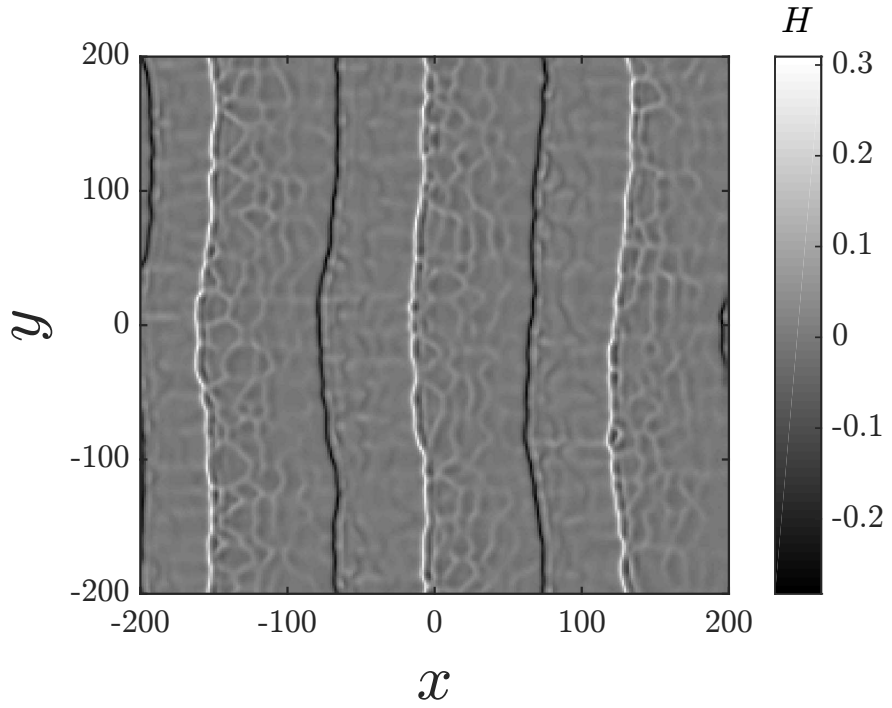

Figure 2.12: The mean curvature of a surface obtained from a simulation of Eq. (2.2) at time $t = 3000$. The figure shown is the mean curvature of the surface seen in Figure 2.10 (b).

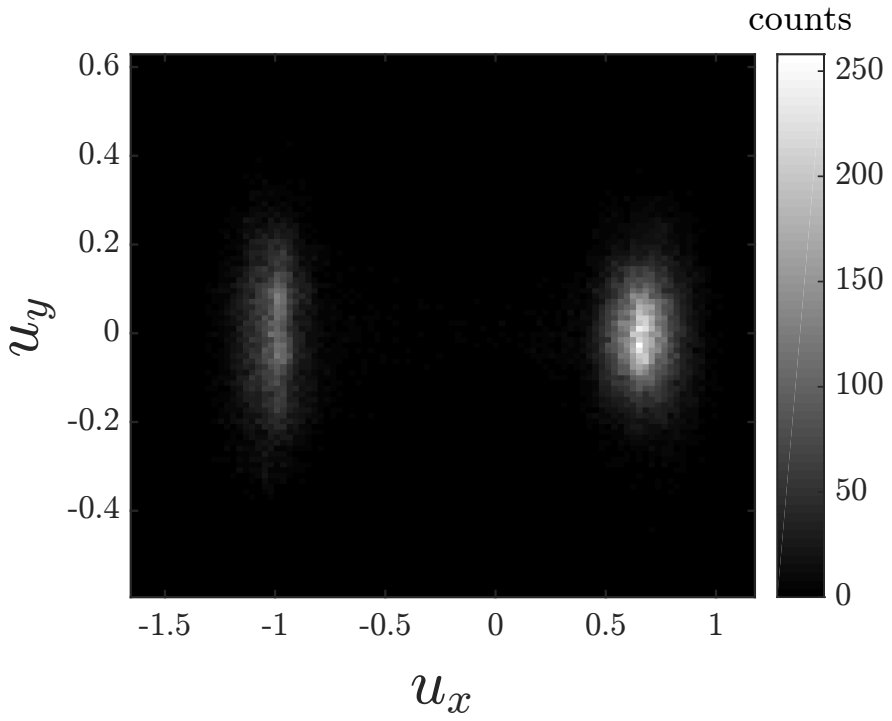

Figure 2.13: The gradient distribution of the surface obtained from a simulation of Eq. (2.2) at time $t = 3000$. The figure shown was obtained from the surface seen in Fig. 2.10 (b).

which there are only two selected slopes even though there are three zeros for the cubic equation that yields the selected slopes [32].

Simulations of Eq. (2.2) with different values of κ_1 and κ_2 (and with all other coefficients held fixed) produce surfaces with gradient distributions that are more heavily weighted on different subsets of the curves satisfying Eq. (2.56). This is illustrated in Figs. 2.14 (a) and (b), which are gradient distributions obtained from two surfaces produced by simulations with different values of κ_2 but the same parameter values $\kappa_1 = \lambda_1 = \lambda_2 = -0.5$, $B = 1$, $\gamma_1 = 1$ and $\gamma_2 = 0$. Equation (2.56) also works well if γ_2 is nonzero, as can be seen in Fig. 2.14 (c), which was obtained from a simulation with coefficient values $\kappa_1 = 0$, $\kappa_2 = -0.5$, $\lambda_1 = \lambda_2 = -0.5$, $B = 1$, $\gamma_1 = 1$ and $\gamma_2 = -1$. The values of s and μ used to produce the red curves in these figures were determined directly from the simulations. The method we employed to compute s was introduced in Section 2.2.1. We calculated an average s by comparing the surface at each of the final 10 time steps with the surface at its previous time step. The values of μ were determined by the slope of a linear fit of the average value of u versus time during the last 10 time steps.

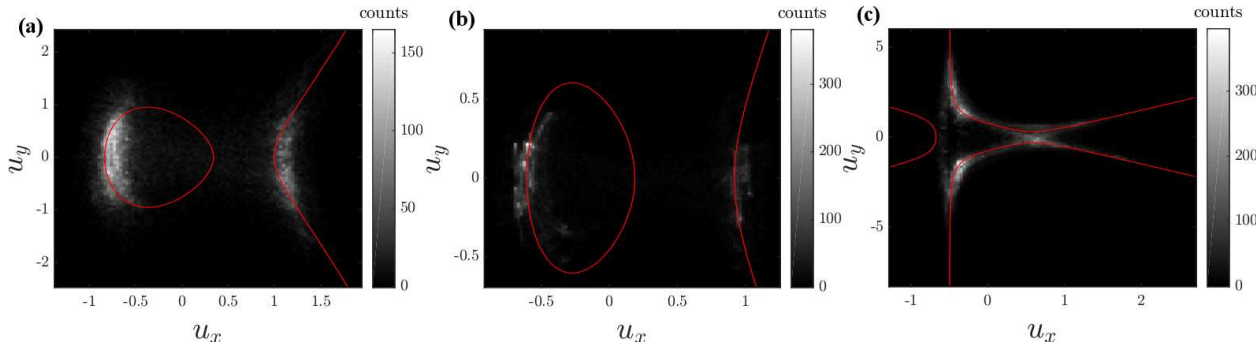

Figure 2.14: The gradient distributions of three surfaces obtained from a simulation of Eq. (2.2) integrated up to time $t = 750$ with the solutions to Eq. (2.56) plotted as red curves. The parameter values used in the simulations were (a) $\kappa_1 = -0.5$, $\kappa_2 = -0.5$, $\lambda_1 = -0.5$, $\lambda_2 = -0.5$, $B = 1$, $\gamma_1 = 1$ and $\gamma_2 = 0$; (b) $\kappa_1 = -0.5$, $\kappa_2 = 0.5$, $\lambda_1 = -0.5$, $\lambda_2 = -0.5$, $B = 1$, $\gamma_1 = 1$ and $\gamma_2 = 0$; (c) $\kappa_1 = -0.5$, $\kappa_2 = 0.5$, $\lambda_1 = -0.5$, $\lambda_2 = -0.5$, $B = 1$, $\gamma_1 = 1$ and $\gamma_2 = -1$.

2.5.3 Comparison with the predictions of the one-dimensional theory

We now investigate how well the predictions made in Section 2.3 for the 1D case apply to simulations in 2D, with a focus on the case in which there is smoothing in the transverse direction. Figure 2.15 shows a line scan along the x axis of a surface obtained by integrating Eq. (2.2) with the parameter values $\kappa_1 = -0.5$, $\kappa_2 = 1$, $\lambda_1 = -5$, $\lambda_2 = -5$, $B = 1$, $\gamma_1 = 100$ and $\gamma_2 = 0$. From this figure, it is evident that terraces have formed. Moreover, the line scan is quite similar to surfaces obtained in simulations in 1D (see Fig. 2.3).

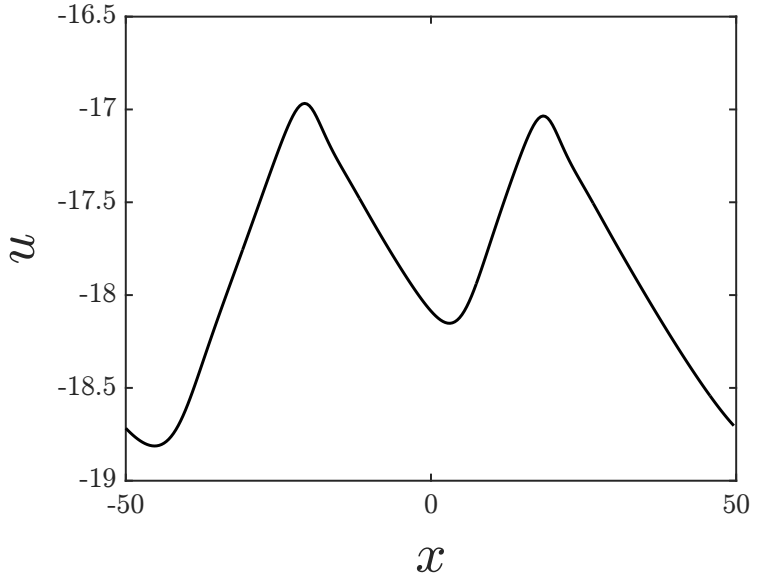

Figure 2.15: A line scan along the x axis slice of a surface with transverse smoothing at time $t = 2000$. Note that the vertical scale has been enlarged by a factor of 40 to make the pattern easily discernible; the magnitude of the surface slope nowhere exceeds 0.1. The parameter values used were $\kappa_1 = -0.5$, $\kappa_2 = 1$, $\lambda_1 = -5$, $\lambda_2 = -5$, $B = 1$, $\gamma_1 = 100$ and $\gamma_2 = 0$.

In Section 2.3, we derived formulas for the propagation velocity, downward drift speed and selected slopes of the terraces that form on a surface governed by Eq. (2.11), i.e., a surface that has no transverse variations in height. In Figure 2.16, we compare the selected slopes $\phi_\pm$, the propagation velocity s and the downward drift speed μ as given by Eqs. (2.47), (2.38) and (2.45) with the values obtained from numerical integrations of Eq. (2.2) as $\gamma \equiv 6\gamma_1$ is varied while the other coefficients are held fixed at the values $\kappa_1 = -1$, $\kappa_2 = 20$, $B = 0$, $\lambda_1 = -0.5$, $\lambda_2 = -0.5$

and $\gamma_2 = 0$. (Note the large positive value of κ_2 we selected.) We used a smaller domain for these simulations so that an approximate steady state would be reached at an earlier time than it was in the figures previously shown. The methods of determining the values of s and μ from the simulations were the same as we discussed earlier in this section. The error bars for s are obtained from the standard deviation of the 10 values averaged to give s. The error bars on μ were calculated from the R-squared value of the linear fit using $\mu_{\text{err}} = (1 - R^2)\mu_{\text{value}}$. We used the same method as in 2.4 to calculate $\phi_{\pm}$ from the simulations. The results from the simulations in 2D with strong smoothing in the transverse direction are in excellent agreement with predictions of the 1D theory given by Eqs. (2.47), (2.38) and (2.45).

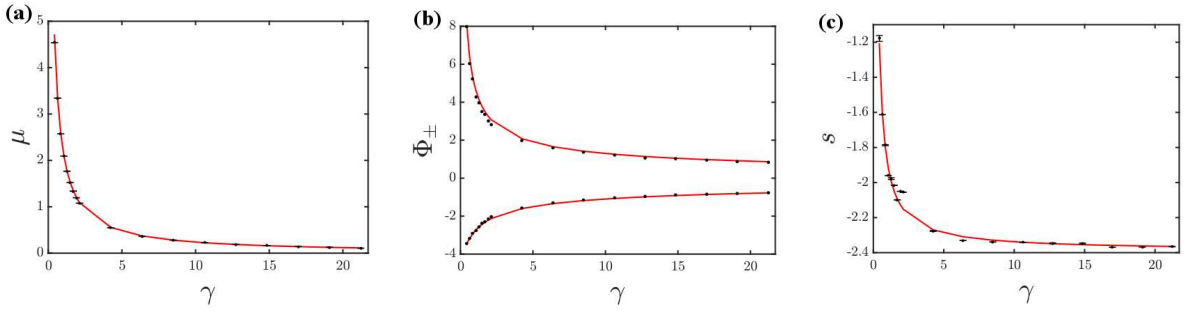

Figure 2.16: (a) Downward drift speeds μ, (b) selected slopes $\phi_{\pm}$ and (c) propagation velocities s. The data points are values obtained from simulations of Eq. (2.2). The red curves are predictions from the 1D theory: (a) μ as given by Eq. (2.45), (b) $\phi_{\pm}$ as given by Eq. (2.47) and (c) s as given by Eq. (2.38). The surfaces were simulated to time $t = 500$ and the parameter values used were $\kappa_1 = -0.5$, $\kappa_2 = 10$, $\lambda_1 = -0.5$, $\lambda_2 = -0.5$ and $\gamma_2 = 0$.

Our simulations in two dimensions exhibit interrupted coarsening. Evidence for this is seen in Fig. 2.17, which is a plot of the surface width (i.e., the standard deviation of the surface height) versus time for the simulation that produced the surface seen in Fig. 2.10. The surface width grows for some time and then appears to asymptote to a finite value. Furthermore, inspection of Fig. 2.10 itself shows that both the lateral and vertical scales of the surface grow from (a) to (b) but are not substantially changed from (b) to (c). We observed interrupted coarsening in all of our simulations that yielded terraced topographies.

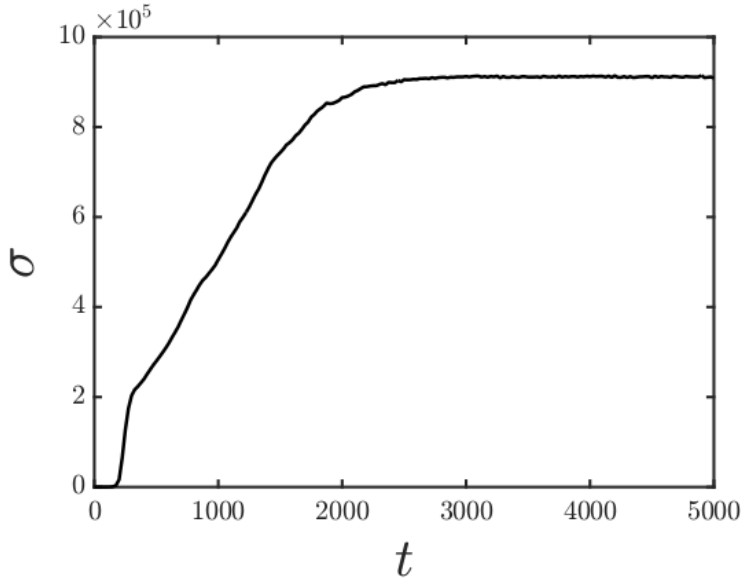

Figure 2.17: The surface width σ versus time obtained from a simulation of Eq. (2.2). The figure shown is produced from the same simulation that yielded Fig. 2.10.

2.5.4 Elongated pyramidal structures

Next we present simulation results that resemble the topography seen in Fig. 2.18, which shows images from experiments performed by Carter *et al.* at high angles of incidence [10]. Both the experimental surfaces and our simulated surfaces exhibit pyramidal structures that protrude from the surface and that are elongated in the projected ion beam direction. We see these structures form in our numerical integrations of Eq. (2.2) when there is a linear instability in the transverse direction (i.e., $\kappa_2 < 0$) and the magnitudes of both γ_1 and γ_2 are sufficiently large. Since the pyramidal structures only form in simulations with nonzero values of γ_2, the term $u_x u_y^2$ plays an critical role in their formation. One such simulation result is shown in Fig. 2.19. Notice that the pyramidal structures that form in our simulation have ends that tend to line up, just as is seen in Fig. 2.18. The gradient distribution for Fig. 2.19 is shown in Fig. 2.20. Clearly, there is a strongly selected negative value of u_x in this simulation. Furthermore, the gradient distribution demonstrates that the elongated portion of the pyramidal structures have $u_x > 0$ and the ends of the elongated pyramids have $u_x < 0$; i.e., these pyramidal structures protrude from the surface with their ends facing the ion source. This is again consistent with Carter *et al.'s* experimental

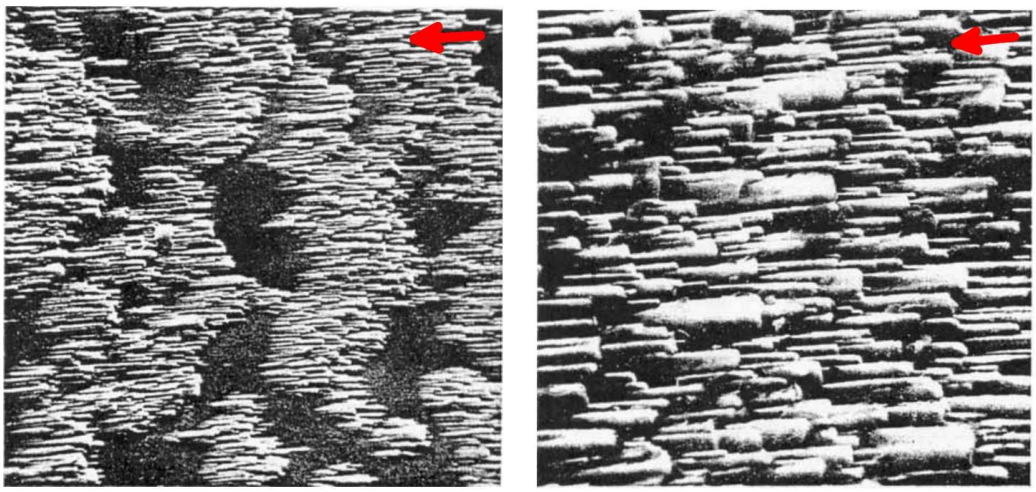

Figure 2.18: SEM images of a silicon surface produced by Carter in Ref. [10] by bombarding silicon with 40 keV argon ions at an angle of incidence of 70°. The surface shown on the right is a magnification of the surface on the left. The red arrows indicate the ion beam direction projected onto the surface. There are elongated pyramidal structures that are protruding out of the surface and facing towards the beam. The ends of the structures appear to have a tendency to line up.

observations. The mean curvature of the surface — which is shown in Fig. 2.21 — shows that shocks that are elongated in the longitudinal direction can form. These shocks are close to being aligned with the x-axis but are not parallel to it. To see this, note that if we consider a surface that has no longitudinal variations, then Eq. (2.2) reduces to

$$u_t = \kappa_2 u_{yy} - B u_{yyyy} + \lambda_2 u_y^2. \tag{2.57}$$

This is the KS equation and it does not lead to shock formation.

In the simulation we just discussed, perpendicular-mode ripples formed at early times. However, elongated pyramidal structures can also form when parallel-mode ripples are present for low fluences. Figure 2.23 demonstrates this with two snapshots of a surface obtained by simulating Eq. (2.2): (a) shows the surface at time $t = 150$ and (b) shows the same surface at a later time ($t = 850$). Our simulation results are remarkably similar to the topographies obtained by Datta *et al.* when they irradiated a germanium surface with 100 keV krypton ions at a 60° angle of incidence: see Fig. 2.22. Datta *et al.* found that the parallel-mode ripples that developed at early times ultimately evolved into elongated pyramidal structures, just as in our simulations.

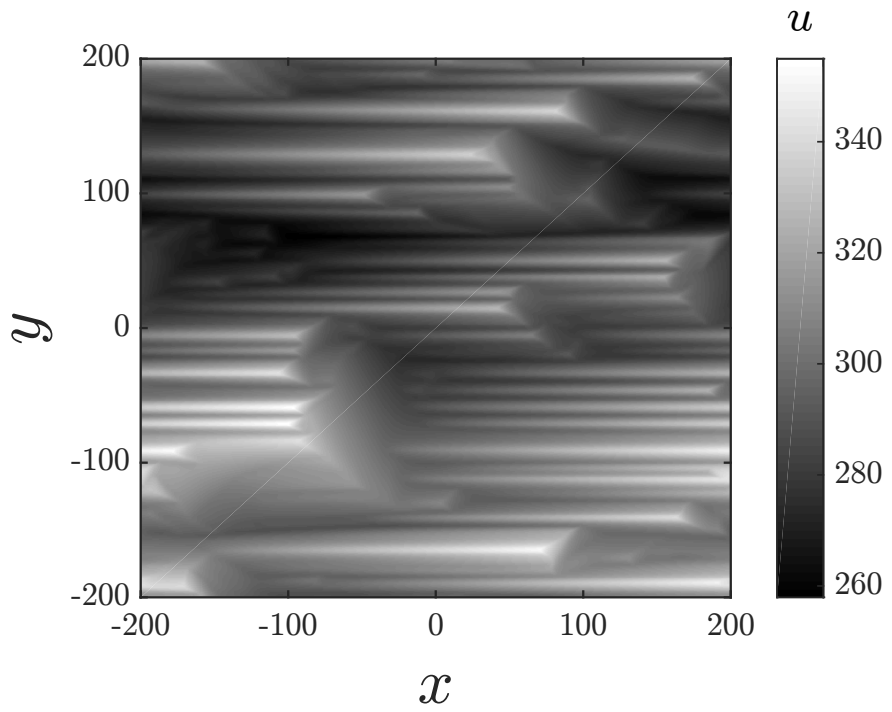

Figure 2.19: A surface obtained by integrating Eq. (2.2) up to time $t = 1800$, starting from a low amplitude white noise initial condition. The surface is still evolving at the time shown. At early times, perpendicular-mode ripples formed. Later, these ripples evolved into the elongated pyramidal structures seen in the figure. The parameter values used were $\kappa_1 = 0$, $\kappa_2 = -0.6$, $B = 1$, $\lambda_1 = 0.5$, $\lambda_2 = 0.5$, $\gamma_1 = 1$ and $\gamma_2 = -3$.

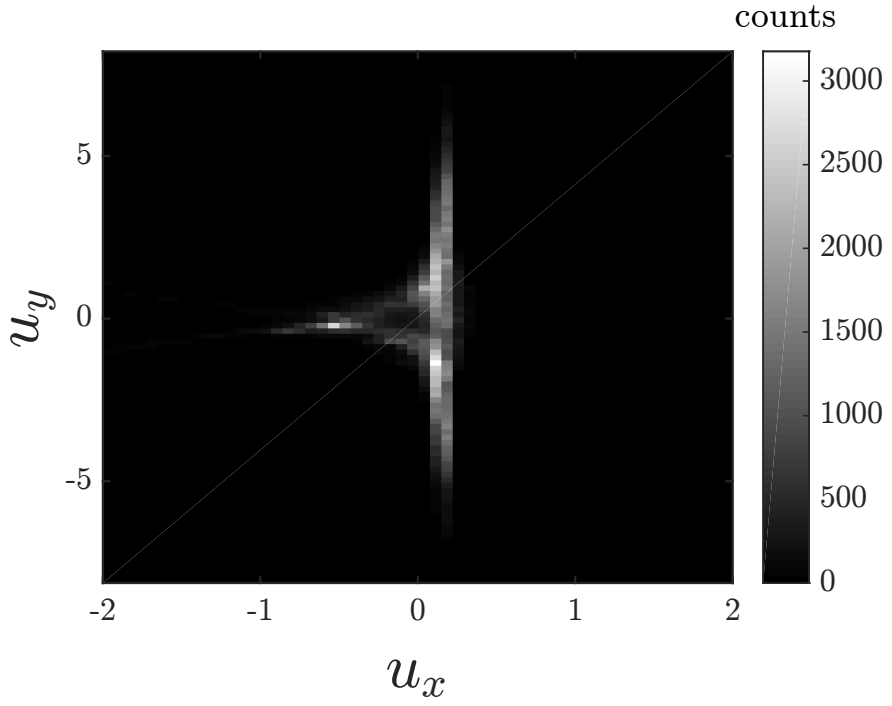

Figure 2.20: The gradient distribution of the surface obtained from a simulation of Eq. (2.2), integrated up to time $t = 1800$. The figure was obtained from the surface seen in Fig. 2.19.

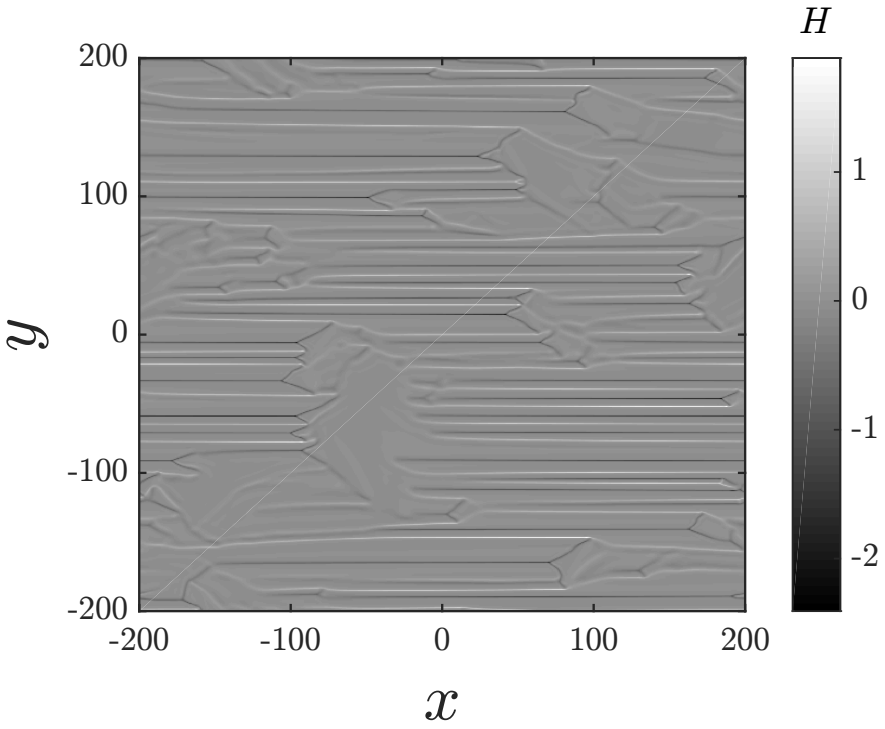

Figure 2.21: The mean curvature H of the surface shown in Fig. 2.19. Shocks that are elongated in the longitudinal direction are evident.

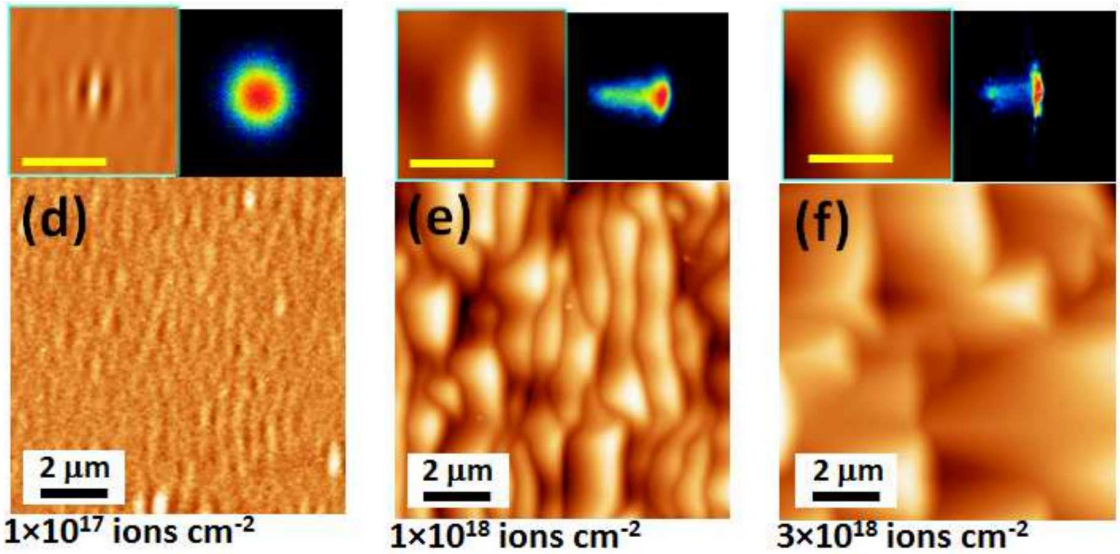

Figure 2.22: AFM images that show the evolution of a germanium surface bombarded by 100 keV kryton ions at an angle of incidence of 60°, obtained in an experiment by Datta *et al*. The height scales are (d) 20.7 nm, (e) 315.7 nm, and (f) 2 nm. The top left of each image shows the 2D autocorrelations of the surface. The top right shows its 2D slope distributions. The direction of the incident beam projected onto the surface was from right to left, and so the ripples in the leftmost image are parallel-mode ripples. This figure is from Ref. [11].

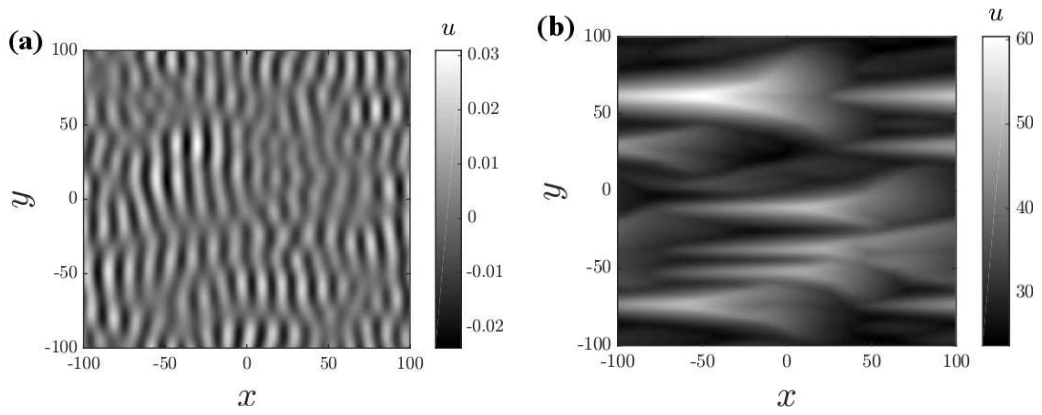

Figure 2.23: (a) A surface obtained by integrating Eq. (2.2) up to time $t = 150$, starting from a low amplitude white noise initial condition. Parallel-mode ripples are evident. (b) At time $t = 850$, the surface exhibits elongated pyramidal structures. The parameter values used in this simulation were $\kappa_1 = -0.5$, $\kappa_2 = -0.3$, $B = 1$, $\lambda_1 = -0.05$, $\lambda_2 = -0.5$, $\gamma_1 = 1$ and $\gamma_2 = -3$.

2.5.5 Lenticular Depressions

Lenticular depressions are another interesting topographical feature that have been observed in experiments. These lens-shaped depressions are prominent, for instance, in Fig. 2.24, in which silicon was bombarded with a 1.2 keV xenon ion beam with a 75° angle of incidence. We have also seen lenticular depressions in some simulations of Eq. (2.2) in which the initial condition was low amplitude spatial white noise — see Fig. 2.25 (a) for an example. The mean curvature of that surface is shown in Fig. 2.25 (b). This figure shows that the pit's edge is a shock and there is a complicated cellular structure outside of the pit. There is also a shock that crosses the bottom of the pit. In the experiments, the outlines of the lenticular depressions appear to be shocks and shocks traverse the base of the pits, just as in our simulations.

Lenticular features arise in our simulations if the value of γ_1 is slightly larger than the threshold value for terrace formation. They are transient structures that appear when the surface is transitioning from KS-like behavior to a terraced topography. In fact, in this simulation, the emergence of the depression corresponds to the emergence of the first undercompressive shock. Since $\gamma_2 = 0$ in the simulation that produced Fig. 2.25, it is clear that the term $u_x u_y^2$ is not necessary for the formation of lenticular depressions. However, its inclusion can modify their shape.

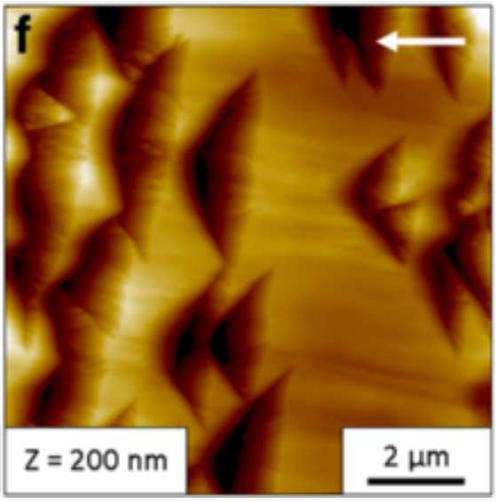

Figure 2.24: A silicon surface obtained in an experiment by Teichmann *et al.* after bombarding it with 1.2 keV xenons ions at an angle of incidence of 75°. The value of z indicates the difference between the maximum and minimum values of the surface height. The darker color indicates lower surface heights. The ion fluence was 1.35×10^{19} ions/cm^2. The arrow indicates the direction of the ion beam projected onto the surface. This figure is from Ref. [12].

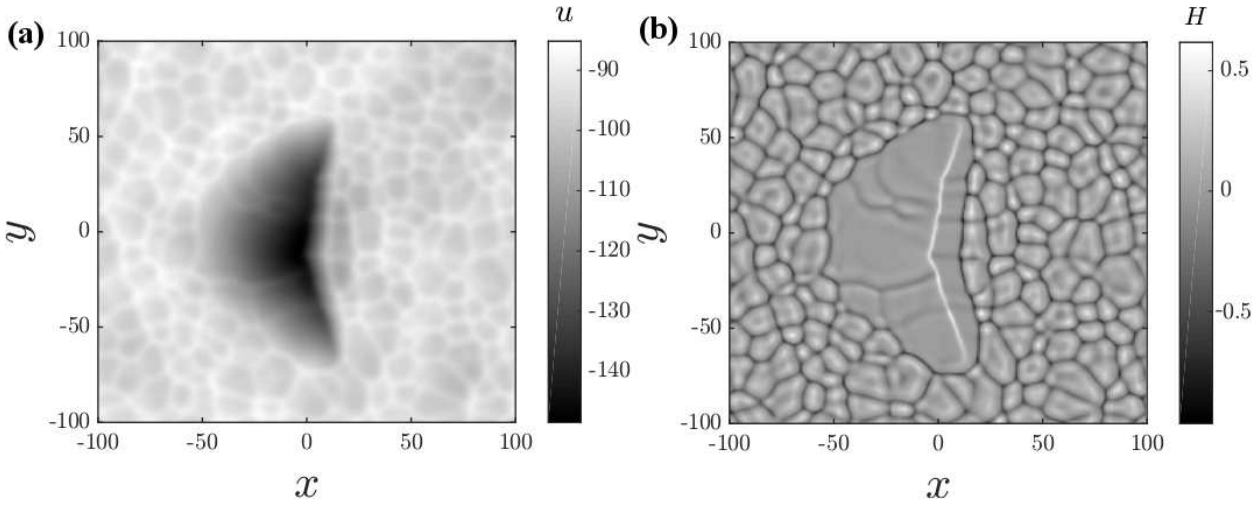

Figure 2.25: (a) A surface obtained by integrating Eq. (2.2) up to time $t = 465$, starting from a low amplitude spatial white noise initial condition. A lenticular depression is shown, surrounded by a region of the surface that looks very much like what would be seen in simulations of the isotropic KS equation. (b) The mean curvature H of the surface in (a). The parameters were $\kappa_1 = -0.5$, $\kappa_2 = -0.5$, $B = 1$, $\lambda_1 = -0.5$, $\lambda_2 = -0.5$, $\gamma_1 = 0.11$ and $\gamma_2 = 0$.

2.6 Discussion

Terraced topographies are frequently observed in experiments in which a solid surface is bombarded at high angles of incidence [2, 4, 9, 10, 24–31]. The terraced structures are also found to coarsen as time passes.

In 1976, Hauffe suggested that terraced structures coarsen as a result of sputtering by reflected ions [24]. He did not derive or study an equation of motion for the solid surface, and offered no explanation for the formation of the terraces themselves. Hauffe also neglected the effect of redeposition, which would tend to counteract the coarsening caused by ion reflection. In contrast, the equation of motion we studied in this thesis produces ripples as a result of curvature dependent sputtering and/or mass redistribution. As nonlinear effects grow in importance, terraces emerge because undercompressive shocks form. The terraced surfaces that result from our model coarsen with time even though it does not include the effects of ion reflection and re-impingement on the solid surface. Therefore, the so-called “Hauffe mechanism" does not appear to be needed for terrace coarsening to occur.

In obtaining our equation of motion, we assumed that the surface height is slowly varying, and retained terms up to third order in the surface slope h_x. This represents an improvement to the approximation that has almost universally been employed; in that approximation terms of third order and higher in h_x are neglected [22, 40].

It is typically found in experiments that the selected terrace slopes are of order of magnitude unity. The faces of the terraces are often nearly parallel and perpendicular to the ion beam, although there are exceptions to this rule of thumb [2, 29, 30]. The approximate equation of motion we studied in this thesis does not apply if the surface slope is not small. However, our work shows how higher order nonlinearities in the equation of motion can lead naturally to terraced surfaces that coarsen in time. Our equation of motion is also quite generic, and, as we showed, by applying appropriate transformations it can be reduced to a parameter-free form. In contrast, including terms of order u_x^4 and higher would introduce additional parameters into the model. The values of these

parameters would depend upon the detailed angular dependence of the sputter yield, and so the generality of the model would be reduced.

The linear BH theory predicts that if the angle of incidence θ is less than a critical angle θ_2, then $\kappa_1 < \kappa_2$ and $\kappa_1 < 0$. This means that parallel-mode ripples (i.e., ripples with their wave vector parallel to the projected ion direction) will form. If θ is also less than θ_1, then $A > 0$ and hence the ripples propagate into the ion beam. Thus, the BH theory predicts that if parallel-mode ripples develop, they propagate in the direction opposite to the incoming ions, except possibly for high angles of incidence.

In most experiments carried out to date, the ripples have been observed to propagate in the direction opposite to that predicted by the BH theory [3, 5, 27, 34–36], although there is an exception [70]. In this thesis, we analyzed the propagation velocity in the nonlinear regime and our results provide a possible explanation for this discrepancy. During the early stages of the time evolution in which the linear BH theory applies, the ripple amplitude is small and hence measurements of the ripple velocity would be difficult. Most (if not all) experimental observations have likely been carried out in the late-time, nonlinear regime as a consequence. As we have seen, the ripples can propagate in the projected ion direction in this regime. It should be noted that we neglected the u_{xxx} term in our equation of motion (2.11) and this term affects the propagation velocity at early times; in fact, this term itself could lead to ripples propagating in the projected ion direction. However, including this term does not affect our aforementioned conclusion that the propagation direction could switch as time progresses.

One of the key findings of this thesis is that terraced surfaces develop with two special selected slopes because undercompressive shocks form. The formation of undercompressive shocks during the ion bombardment of a solid surface has already been observed experimentally in a different context. Chen *et al.* etched a cylindrical pit into an initially planar silicon surface and then subjected the entire sample to normal-incidence ion bombardment [13, 71, 72]. As shown in Fig. 2.26, the pit radius increased, but its sidewalls remained quite steep. Undercompressive shocks formed between a portion of the sidewall with a selected slope and the flat surface outside the pit.

In the theory that Chen *et al.* advanced to account for their experimental observations, the form of the sputter yield valid for arbitrary angles of incidence was employed. The destabilizing effect of the curvature dependence of the sputter yield was omitted, however. The undercompressive shocks that formed connected a region of slope zero to a region with a selected slope. Thus, there is a single selected slope in the model of Chen *et al.* In contrast, there are *two* selected slopes in our model and the terraced structure develops from a surface that is nominally flat initially.

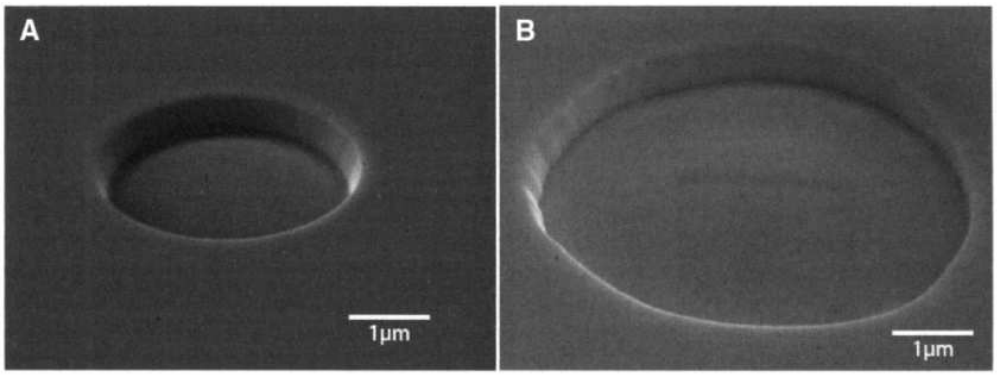

Figure 2.26: An initial circular pit is etched and is shown in (a). After bombarding at normal incidence, the pit radius has increased but the slopes of the pit walls are unchanged, seen in (b). This experiment was carried out by Chen *et al.* , see Ref. [13].

2.7 Conclusions

When the nominally flat surface of an elemental solid is bombarded with a broad ion beam at oblique incidence, parallel-mode nanoscale ripples can develop on the surface. These ripples often evolve into terraces as time passes.

In this thesis, we appended the third order nonlinear term $c_3 u_x^3/6$ to the usual one-dimensional Kuramoto-Sivashinsky equation for the surface height. This term appears in the equation of motion when an improved approximation for the slope dependence of the sputter yield is adopted. Our numerical integrations of this equation of motion revealed that a terraced topography with two distinct selected slopes emerges at long times for a range of values of the parameter c_3. Adjacent regions of nearly constant surface slope are connected by an undercompressive shock; within a

shock, the slope varies rapidly. Once the heteroclinic cycle had been constructed numerically for the transformed equation of motion, we were able to predict how the selected slopes, the terrace propagation velocity and the net erosion rate depend on c_3. These predictions are in excellent agreement with our numerical integrations of the untransformed equation of motion.

Simulations of our model show that the terraces coarsen as time passes, as observed in many experiments. We also established that for a range of parameter values, the ripple propagation direction reverses as the ripple amplitude grows and nonlinear effects become important. This may explain why most experiments indicate that the ripple propagation direction is opposite to the direction predicted by the linear Bradley-Harper theory. Experiments in which the ripple propagation velocity is measured from the early-time, linear regime to the long-time, nonlinear regime would be very valuable.

We also studied an equation of motion that generalizes the PB equation to the case in which the surface height depends on both the longitudinal and transverse coordinates. This equation differs from the usual equation of motion (the anisotropic two-dimensional Kuramoto-Sivashinsky equation) by the inclusion of the cubic nonlinearities u_x^3 and $u_x u_y^2$. Although it is not the most general equation of motion that includes terms up to cubic order in u, the generalized PB equation captures many of the features that are observed in experiments in which the angle of ion incidence is relatively high. For example, for a range of parameter values, it yields parallel-mode ripples at early times. These ripples then evolve into a terraced structure that coarsens with time. For other ranges of the parameters, the surface develops other morphologies reminiscent of those seen in experiments, such as isolated lenticular depressions and elongated pyramidal structures that tilt up out of the surface and towards the beam.

The strong similarities between the surfaces produced by our model and those observed in experiments indicates that the cubic nonlinearities u_x^3 and $u_x u_y^2$ play a crucial role in the dynamics for sufficiently high angles of ion incidence. These nonlinearities could be eliminated in an experiment by bombarding the surface with identical, diametrically opposed beams, or by periodically and rapidly rotating the sample through 180° increments about its surface normal. In experiments

of this kind, the equation of motion is invariant under the transformation $x \rightarrow -x$ and the morphologies produced should differ markedly from those that develop when the sample is stationary and a single, near glancing incidence ion beam is employed.

Chapter 3

Patterning Surfaces Before Ion Sputtering can Yield Nanodot Arrays with Improved Hexagonal Order

The primary obstacle to the widespread adoption of ion-induced pattern formation as a nanoscale fabrication tool has been the presence of numerous defects in the patterns that are typically produced. In the case of surface ripples, some ripples terminate, while others fuse with their neighbors. In contrast, penta- and hepta-defects are found in hexagonal arrays of nanodots produced by ion bombardment of binary materials.

A promising concrete strategy for producing more highly ordered patterns is to bombard a topographically templated surface rather than an initially flat surface [73]. The template should have a regular structure on a length scale that is longer than the natural spacing of the patterns formed by ion sputtering, so that it can be fabricated by, e.g., optical lithography with a mask or optical standing-wave lithography. The purpose of the template is to guide the ion-induced self-organization that occurs at shorter length scales, leading to a more highly ordered nanostructure than would be formed on an initially flat surface.

Some steps toward utilizing templates in ion-induced ripple formation on elemental materials have been taken. If a silicon surface is prepatterned with parallel trenches with a width equal to a few times the ripple wavelength, for example, the ripples that form in the trenches tend to align with the trench walls, and the number of defects in the ripple patterns is small [73].

An intriguing recent experiment suggests another possible route to enhanced ordering. In the experiment, a silica surface was polished mechanically, producing a set of parallel scratches [74]. This surface was then subjected to normal-incidence bombardment with a beam of 1.8 MeV gold ions. The result was an array of nanodots with a much higher degree of order than would have been present had the surface not been polished before bombardment. In particular, chains of nanodots that were presumably parallel to the scratches were observed. Similar results have been obtained

if scratch-like structures are made by prepatterning the surface using near-grazing-incidence ion bombardment rather than by mechanical polishing [75–77].

In this chapter, we investigate the efficacy of using a template to improve the order in nanodot arrays produced by normal-incidence ion bombardment of binary materials. Using numerical simulations, we explore the degree of order produced by a template with a hexagonal array of nanoholes. The nanohole spacing is chosen to be longer than the linearly selected wavelength λ_T, i.e., the natural spacing of the nanodots. We find that this type of template dramatically improves the order when the nanohole spacing is approximately equal to certain integer multiples of λ_T. Comparable results are obtained for a template with a sinusoidally varying surface height. Finally, we study the effect of an initial condition that is meant to resemble a single, long, straight scratch on an otherwise nominally planar surface. Our simulations show that if the scratch width is appropriately chosen, the degree of hexagonal order is strongly enhanced in its vicinity.

We use three different methods to characterize the degree of hexagonal ordering present in the simulated nanodot arrays. The first is a qualitative method that involves inspection of the peaks in the magnitude of the Fourier transform of the surface height. The other two methods are quantitative. One uses the topological data analysis technique called persistent homology. The second quantitative method involves constructing a Voronoi tessellation for the nanodot peaks and computing its nearest-neighbor number distribution. The details of the two quantitative methods were discussed in Section 1.5.2.

3.1 Equation of Motion and Initial Conditions

In order to study the influence of prepatterning on binary materials subjected to ion bombardment, we will numerically integrate the BS equations (1.27) and (1.28) with periodic boundary conditions. The integrations are performed using the exponential time differencing method discussed in Section 1.5. The choice of coefficients used in our simulations were $a = 0.25$, $b = 0.37$, $c = 1$, $\lambda = 0$, $\nu = 1$ and $\eta = 10$. The coefficients of the linear terms is in region I that was discussed in Section 1.3, and the linearly selected wavelength is $\lambda_T \simeq 10.36$. Since $b \simeq 0.9 b_T$,

there is a narrow band of unstable wave vectors. The coefficient ν was chosen to be equal to unity so that the surface would form nanodots instead of ripples. The analytical work in Ref. [8] made the assumption that η was of order ϵ^{-1}, where ϵ is the distance of b from the threshold value as defined by $b = (1 - \epsilon)b_T$. Thus, we set the parameter η to 10 so that our numerical results can be readily compared with the analytical results of Ref. [8].

Three types of initial conditions will be considered in this thesis: hexagonally ordered arrays of nanoholes, sinusoidal ripples and straight scratches. We superimposed small amplitude spatial white noise on the initial conditions to account for the randomness that would exist on a real prepatterned surface. The initial condition for the composition was small amplitude spatial white noise in all simulations. The noise had an amplitude of 10^{-4} for both the height and composition in all of the simulations.

The hexagonal initial condition was formed by superimposing three sine waves. If a square domain were used for the hexagonal initial condition, there would be an unphysical discontinuity at the boundary. Thus, in order to satisfy the periodic boundary conditions, we chose to do the simulations in the rectangular domain given by $-L \leq x \leq L$ and $-L/\sqrt{3} \leq y \leq L/\sqrt{3}$, where $L = 200$. The functional form used for the hexagonal initial condition was

$$u_{\mathrm{hex},0}(x, y) = 10^{-2}\left[\sin^2(\mathbf{k}_{\mathrm{a}} \cdot \mathbf{r}) + \sin^2(\mathbf{k}_{\mathrm{b}} \cdot \mathbf{r}) + \sin^2(\mathbf{k}_{\mathrm{c}} \cdot \mathbf{r})\right] + \rho(x, y), \tag{3.1}$$

where $\rho(x, y)$ is the low amplitude spatial white noise, $\mathbf{r} \equiv x\hat{\mathbf{x}} + y\hat{\mathbf{y}}$, $\hat{\mathbf{k}}_{\mathrm{a}} \equiv \hat{\mathbf{x}}$, $\hat{\mathbf{k}}_{\mathrm{b}} \equiv \cos(2\pi/3)\hat{\mathbf{x}} + \sin(2\pi/3)\hat{\mathbf{y}}$, $\hat{\mathbf{k}}_{\mathrm{c}} \equiv \cos(4\pi/3)\hat{\mathbf{x}} + \sin(4\pi/3)\hat{\mathbf{y}}$, and k_{a}, k_{b} and k_{c} are set to a common value that we will call k_I. Since each of the sinusoids is squared, $\lambda_1 \equiv \pi/k_I$ is their wavelength. We varied the parameter λ_1 from simulation to simulation while keeping L fixed. For convenience, let $k_1 \equiv 2\pi/\lambda_1 = 2k_I$. The wavelength λ_1 cannot be chosen arbitrarily, since $2L/\lambda_1$ must be a positive integer. If $2L/\lambda_1$ were not an integer, then, because of the periodic boundary conditions, there would be an unphysical discontinuity in the height profile of the initial condition, which would produce unphysical results.

The functional form for the sinusoidal initial condition was

$$u_{\sin,0}(x,y) = A_0 \sin(k_2 x) + \rho(x,y), \tag{3.2}$$

where A_0 is the amplitude of the initial sinusoid, and $k_2 \equiv 2\pi/\lambda_2$ and λ_2 is the wavelength of the initial sinusoid, which we varied between different simulations. The spatial domain was taken to be square: $-L \leq x, y \leq L$. Again, the initial wavelength could not be chosen arbitrarily: $2L/\lambda_2$ must equal a positive integer.

The functional form for the scratch initial condition was motivated by an experiment in which an atomic force microscope was used to scratch a Ni-Fe surface [78]. The scratching process produced ridges on each side of the groove — a feature that we included in our initial condition. The form of the initial condition used for the scratch template was

$$u_{\text{scratch},0}(x,y) = 10^{-2}\left(\frac{x^2}{1.25\sigma^2} - 1\right)\exp\left(-\frac{x^2}{2\sigma^2}\right) + \rho(x,y), \tag{3.3}$$

where σ is a parameter that determines the half-width of the scratch. Varying σ does not affect the scratch's maximum or minimum values. The number 1.25 appears only in order to make the scratch depth several times larger than the ridge height. Its precise value does not have a significant influence on the results we obtain. Since we are using periodic boundary conditions, this single scratch on a finite spatial domain can be thought of as a series of widely-spaced, parallel scratches on an infinitely extended domain. The scratches lie parallel to the y-axis.

3.2 Results

We separate our simulation results into four subsections: (1) nominally flat initial surfaces, (2) hexagonal templates, (3) sinusoidal templates and (4) scratch initial conditions.

3.2.1 Nominally Flat Initial Conditions

First, we present the control case in which the initial condition of the simulations was small amplitude spatial white noise; i.e., there was no templating. In Fig. 3.1 (left), the surface height at time $t = 10^4$ is shown; it is evident that multiple domains of hexagonally ordered nanodots have formed. The magnitude of the Fourier transform of the surface height is plotted in Fig. 3.1 (right). Fig. 3.1 should be compared with the simulation results in Sections 3.2.3 and 3.2.5, since those simulations were performed on square domains. Fig. 3.2 is the analogue of Fig. 3.1 but with the simulation performed on the same rectangular domain that will be used in the hexagonal template simulations described in Section 3.2.2. The Fourier transforms in both Figs. 3.1 and 3.2 exhibit a narrow band of unstable wave vectors as a diffuse annulus with mean radius $2\pi/\lambda_T \simeq 0.61$, where λ_T denotes the linearly selected wavelength. Although there is some structure within the two annuli, it is not very pronounced. This indicates that the hexagonal ordering is only strong locally; globally, there is no preferred orientation for the hexagons.

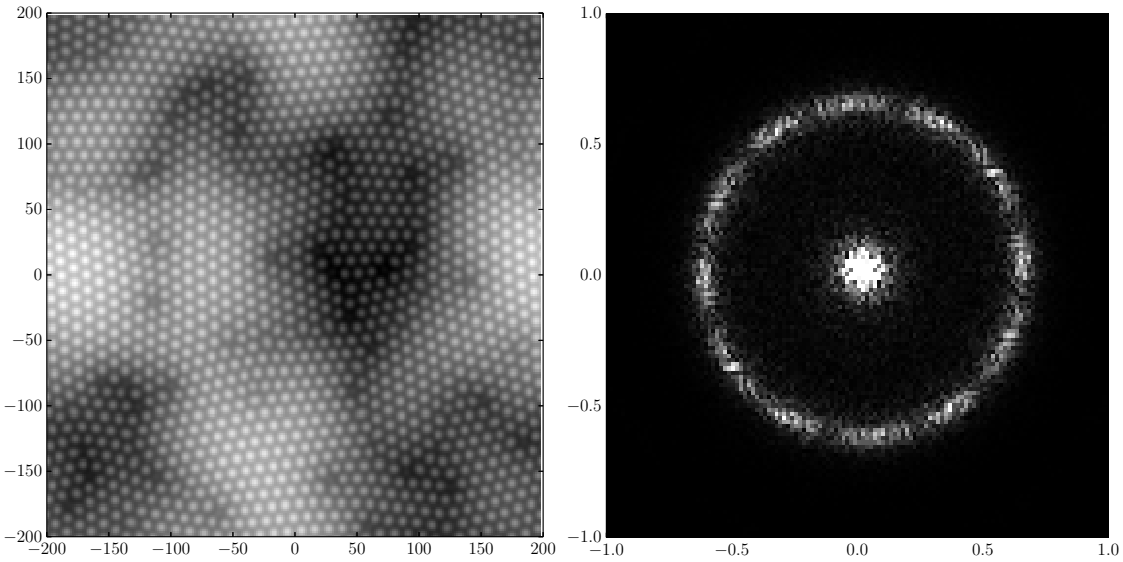

Figure 3.1: The height (left) and the magnitude of the Fourier transform (right) of a non-templated surface after integrating to time $t = 10^4$. White coloring indicates larger values and the black coloring indicates smaller values.

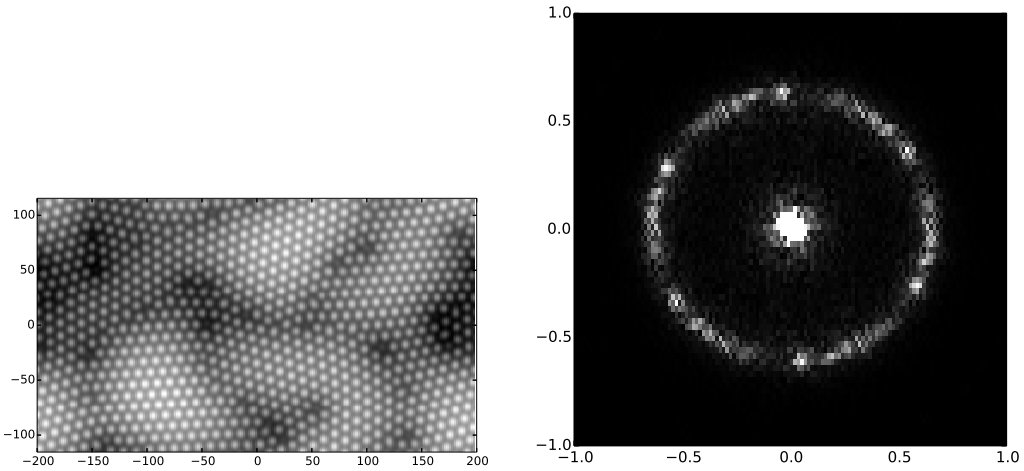

Figure 3.2: The height (left) and the magnitude of the Fourier transform (right) of a non-templated surface after integrating to time $t = 10^4$.

3.2.2 Hexagonal templates

For the simulations using a hexagonal initial condition, we find that there can be either little effect or a dramatic improvement of the global hexagonal order of the nanodots. Dramatic improvement of the hexagonal order was only observed when the wavelength of the initial sine waves was approximately equal to λ_T or $2\lambda_T$. For example, this effect can be seen clearly in Figs. 3.3 and 3.4, which were generated from the simulations with $\lambda_1 \simeq 2\lambda_T$ and $\lambda_1 \simeq \lambda_T$, respectively. The Fourier transforms of these surface heights also demonstrate the strong global hexagonal order by exhibiting six equally spaced peaks in the annulus of unstable wave vectors. On the other hand, if λ_1 was not close to $2\lambda_T$ or λ_T, no strong improvement in order was observed, as in Fig. 3.5.

In order to quantify the dependence of global hexagonal order on the initial wavelength λ_1, we simulated the evolution of the surface for 24 different initial wavelengths. Furthermore, we performed 10 simulations at each of these wavelengths. Using the persistent homology method described in Section 1.5.2, we computed H_1 sums for each of the initial wavelengths, and then averaged the results over the 10 realizations. In all our H_1 sum calculations, we filtered out persistence intervals with lengths less than the one pixel resolution of the local maximum finder. The results are shown in Fig. 3.6. The error bars were obtained from the standard deviations of the 10 trials at each wavelength. The H_1 sum characterizes the hexagonal order in a way that agrees

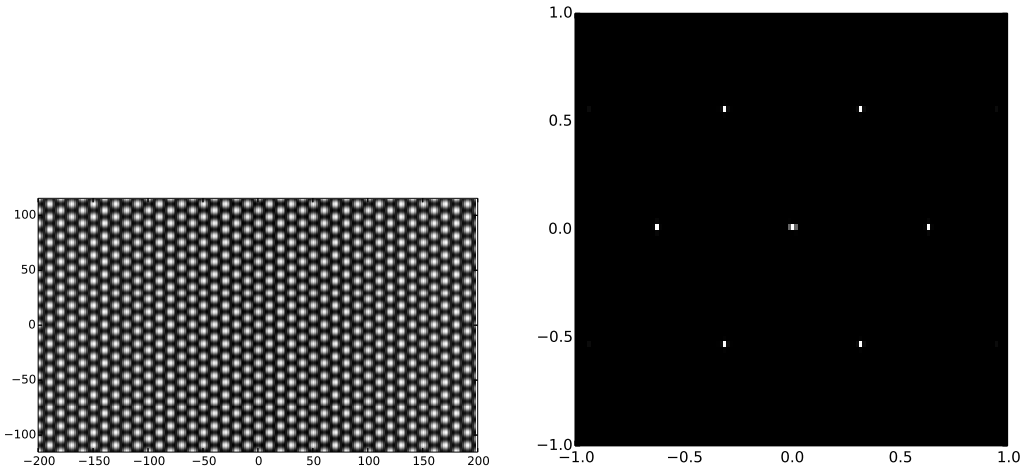

Figure 3.3: The height (left) and the magnitude of the Fourier transform (right) of a hexagonally templated surface after integrating to time $t = 10^4$. The initial wavelength was $\lambda_1 = 20 \simeq 2\lambda_T$. Typical patterns that form in experiments have dots that are about 50 nm in diameter; this template has height variations that would need to be about 100 nm in diameter for an ion beam experiment.

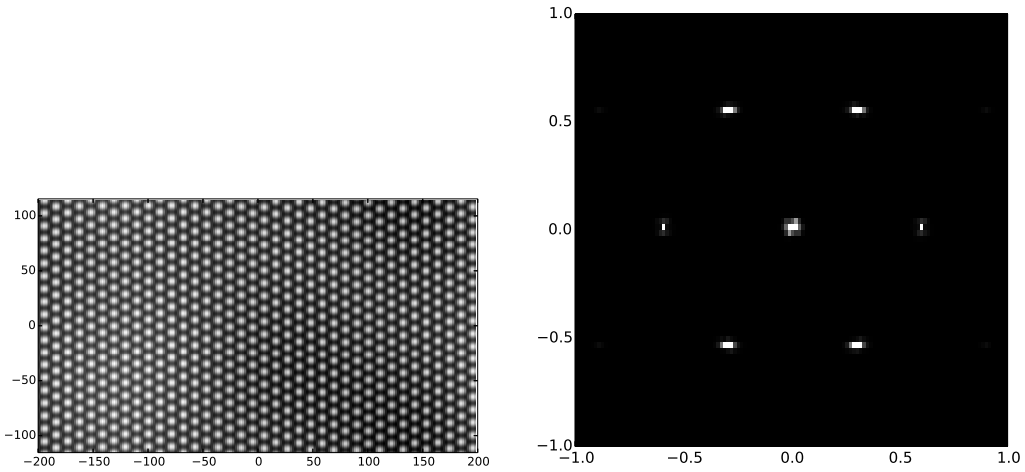

Figure 3.4: The height (left) and the magnitude of the Fourier transform (right) of a hexagonally templated surface after integrating to time $t = 10^4$. The initial wavelength was $\lambda_1 = 400/38 \simeq \lambda_T$.

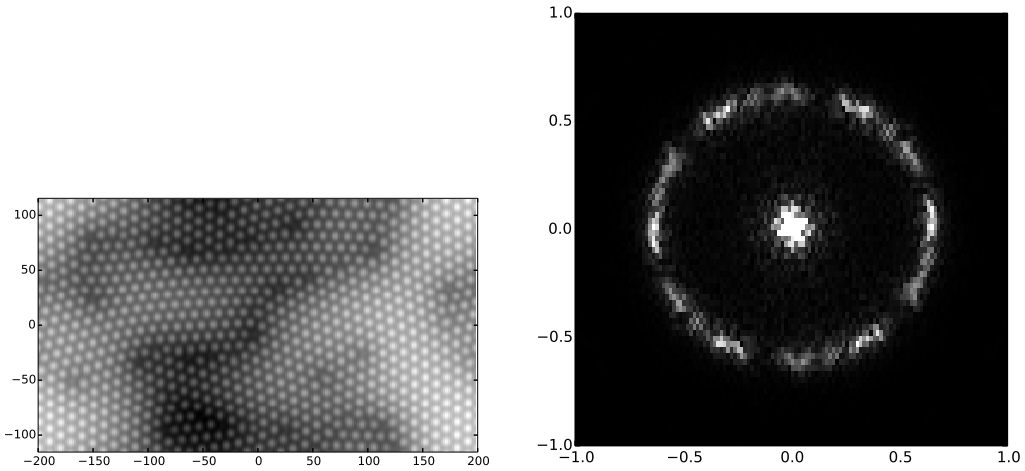

Figure 3.5: The height (left) and the magnitude of the Fourier transform (right) of a hexagonally templated surface after integrating to time $t = 10^4$. The surface is very slowly evolving at the time shown. The initial wavelength was $\lambda_1 = 400/18 \simeq 22.2$.

with how one would qualitatively describe the order based on a visual inspection of the real space results. In particular, it shows the excellent global hexagonal order that occurs for $\lambda_1 \simeq 2\lambda_T$ and $\lambda_1 \simeq \lambda_T$. There is also a much larger H_1 sum for the simulations that had $\lambda_1 \simeq 22.2$, or equivalently $k_1/k_T \simeq 0.46$. One such simulation is shown in Fig. 3.5. A visual inspection corroborates the H_1 sum's indication that the hexagonal ordering of these surfaces is on par with the results of the non-templated surfaces, such as Fig. 3.2. Furthermore, there is improved order for many simulations with initial wavelengths near the linearly selected wavelength. This is also observed in the real space results, such as Fig. 3.4.

We further analyzed the hexagonal templates using the nearest-neighbor number distribution introduced in Section 1.5.2. For the results, see Figs. 3.7 and 3.8. Recall that for a perfectly hexagonal lattice the mean and variance of $\Lambda(n)$ would be 6 and 0, respectively. The results are qualitatively in agreement with those obtained using the H_1 sum. The advantage of the H_1 sum over the Voronoi method is that the H_1 sum plot clearly shows that each of the simulations with $\lambda_1 \simeq 2\lambda_T$ evolved to a perfectly ordered hexagonal array of nanodots, while the Voronoi plots only indicate improved order for those simulations. This occurs despite the fact that the H_1 sum is more sensitive to small perturbations than $\Lambda(n)$. The reason the H_1 sum identifies the perfectly

ordered hexagonal arrays and the Voronoi method does not is that we could filter out noise caused by the finite resolution of the local maximum finder when calculating the H_1 sum but not when calculating $\Lambda(n)$.

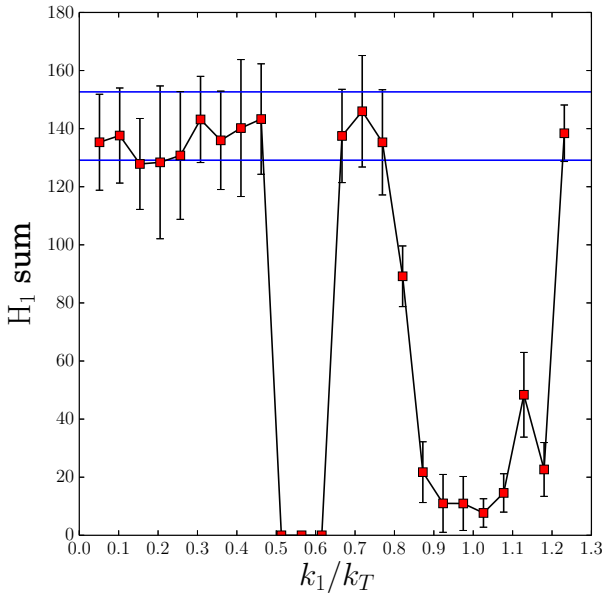

Figure 3.6: The H_1 sum versus the ratio k_1/k_T for the hexagonal templates after integrating to time $t = 10^4$, averaged over 10 realizations. The two horizontal blue lines show the H_1 sum averaged over 10 non-templated initial surfaces after integrating to time $t = 10^4$, plus or minus the standard deviation.

3.2.3 Sinusoidal templates – low amplitude templates

In this section, we continue our analysis of templates with amplitude 10^{-2}, but now with sinusoidal prepatterns instead of hexagonal. Since this is small compared to $\lambda_T \simeq 10.36$, we refer to these prepatterns as low amplitude templates. For the simulations that began with a sinusoidal initial condition, again dramatic improvement of the hexagonal order was only seen when the wavelength of the initial sine wave was approximately equal to λ_T or $2\lambda_T$. For example, this effect can be seen clearly in Figs. 3.9 and 3.10, which were generated from simulations with $\lambda_2 \simeq 2\lambda_T$ and $\lambda_2 \simeq \lambda_T$, respectively. The Fourier transforms of these surface heights also demonstrate the strong global hexagonal order by exhibiting six equally spaced peaks in the annulus of unstable

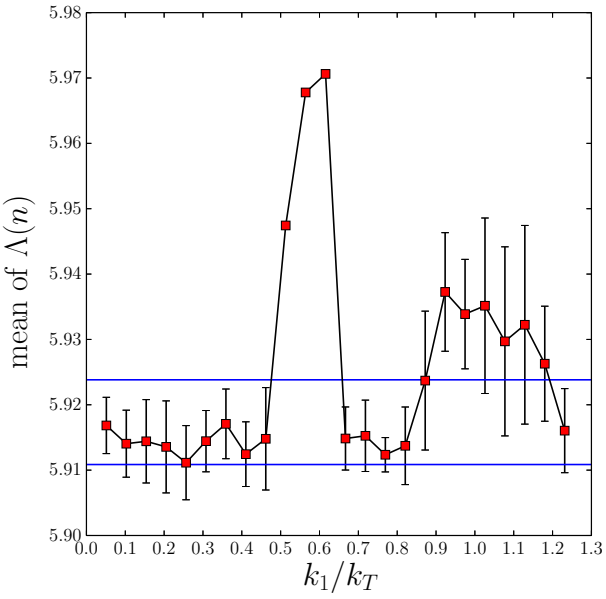

Figure 3.7: The mean of the nearest-neighbor distribution $\Lambda(n)$ versus the ratio k_1/k_T for the hexagonal templates after integrating to time $t = 10^4$, averaged over 10 realizations. The two horizontal blue lines show the mean of $\Lambda(n)$ averaged over 10 non-templated initial surfaces after integrating to time $t = 10^4$, plus or minus the standard deviation.

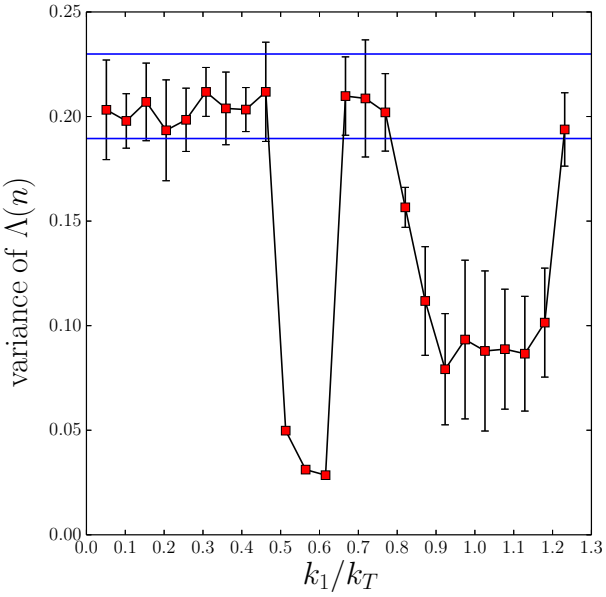

Figure 3.8: The variance of the nearest-neighbor distribution $\Lambda(n)$ versus the ratio k_1/k_T for the hexagonal templates after integrating to time $t = 10^4$, averaged over 10 realizations. The two horizontal blue lines show the variance of $\Lambda(n)$ averaged over 10 non-templated initial surfaces after integrating to time $t = 10^4$, plus or minus the standard deviation.

wave vectors. On the other hand, if λ_2 was not close to $2\lambda_T$ or λ_T, no strong improvement in order was observed. This can be seen in Fig. 3.11, which shows how the H_1 sum varies with k_2/k_T.

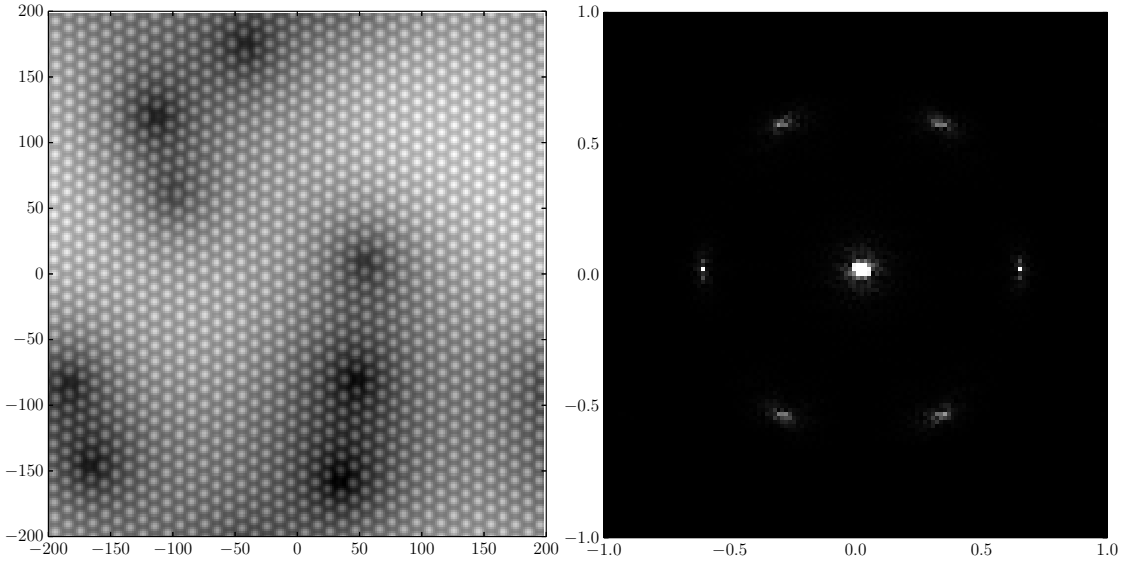

Figure 3.9: The surface height (left) and the magnitude of the Fourier transform (right) after integrating to time $t = 10^4$ for a sinusoidal template with $A_0 = 10^{-2}$ and $\lambda_2 = 20 \simeq 2\lambda_T$.

3.2.4 Sinusoidal templates – larger amplitude templates

Our numerical study of the influence of templating a surface prior to bombardment has so far been limited to low amplitude (10^{-2}) templates. We have seen that the low amplitude templates can dramatically enhance the pattern order at late times only if the template wavelength is approximately equal to or twice the linearly selected wavelength. This motivated us to test whether larger wavelength templates could be effective if the template amplitude was increased. In Fig. 3.12, we show a surface with a high degree of global hexagonal order obtained from integrating Eqs. (1.27) and (1.28) to time $t = 10^4$ starting from a sinusoidal template with $A_0 = 1$ and $\lambda_2 = 40 \simeq 4\lambda_T$. This shows that using higher amplitude templates can allow longer wavelength templates to be effective. We varied the template amplitude while keeping $\lambda_2 \simeq 4\lambda_T$ fixed and calculated the NND variances to produce Fig. 3.13, which shows that the templates with $A_0 \geq 0.4$ lead to a substantial improvement in the global hexagonal order.

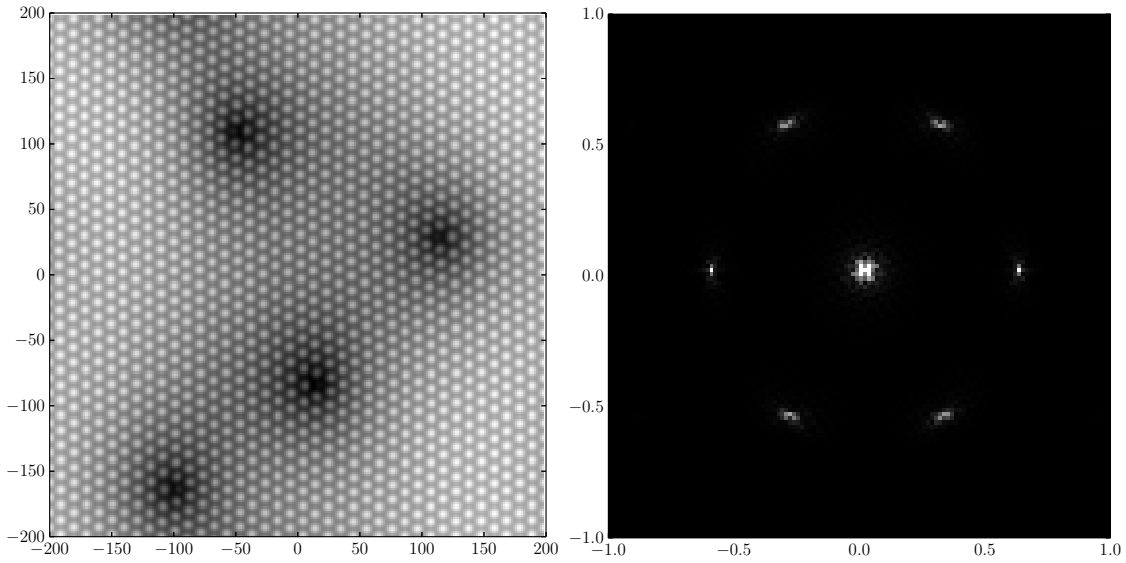

Figure 3.10: The surface height (left) and the magnitude of the Fourier transform (right) after integrating to time $t = 10^4$ for a sinusoidal template with $A_0 = 10^{-2}$ and $\lambda_2 = 400/39 \simeq \lambda_T$.

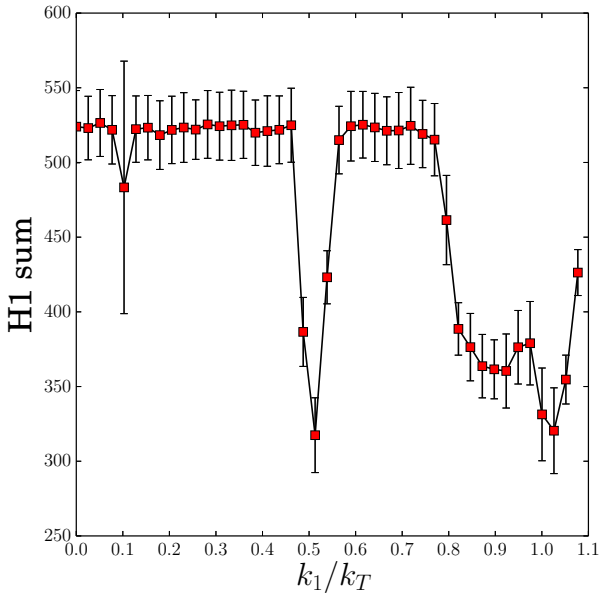

Figure 3.11: The H_1 sum versus the ratio k_1/k_T for the sinusoidal templates with $A_0 = 10^{-2}$ after integrating to time $t = 10^4$, averaged over 150 realizations. The data point at $k_1/k_T = 0$ is from simulations with no templating.

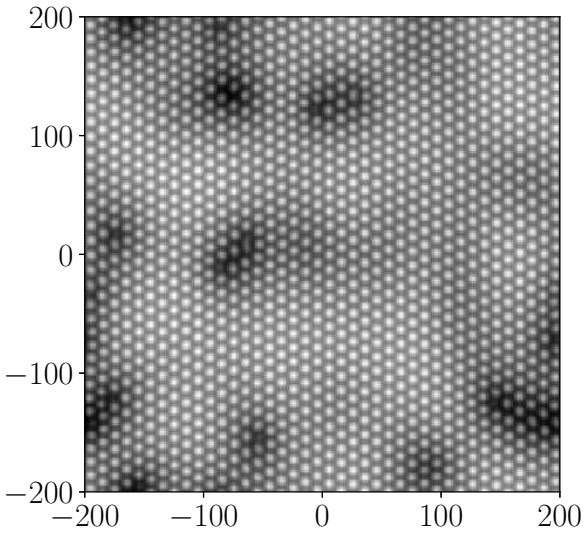

Figure 3.12: The surface obtained after integrating to time $t = 10^4$ for a sinusoidal template with $A_0 = 1$ and $\lambda_2 = 40 \simeq 4\lambda_T$.

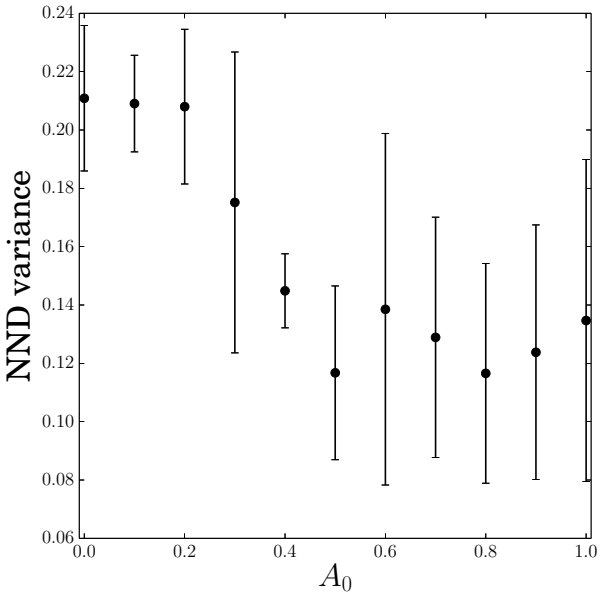

Figure 3.13: The variance of the nearest-neighbor distribution $\Lambda(n)$ versus the template amplitude A_0 for sinusoidal templates with $\lambda_2 \simeq 4\lambda_T$ after integrating to time $t = 10^4$, averaged over 10 realizations.

3.2.5 Scratch prepatterns

If we start with a scratch initial condition, again improved ordering can be observed. In the case of scratch initial conditions, however, the ordering is localized along a strip centered on the initial scratch. This strip is along an elevated region of a long-wavelength roll that is aligned with the y axis. Furthermore, this improved ordering lasts for the full duration of the simulation ($t = 10^4$) only if the width of the scratch 2σ is close to or less than the linearly selected wavelength. The real space surface produced after integrating to $t = 10^4$ starting from a scratch of width $4 \simeq 0.39\lambda_T$ is shown in Fig. 3.14 (left). The corresponding Fourier transform exhibits 6 peaks in the annulus, each separated by 60^{o} as is expected for a surface with global hexagonal order. However, if the initial scratch width is substantially larger than the linearly selected wavelength, as was the case in Fig. 3.15 with $2\sigma = 13.86$, then there is no improvement in the global hexagonal order at time $t = 10^4$. The Fourier transform substantiates this claim since it exhibits a diffuse annulus devoid of any noticeable peaks. Even if the scratch width is chosen to be approximately twice the linearly selected wavelength, there is still no substantial improvement in the global hexagonal order at time $t = 10^4$, as is seen in Fig. 3.16.

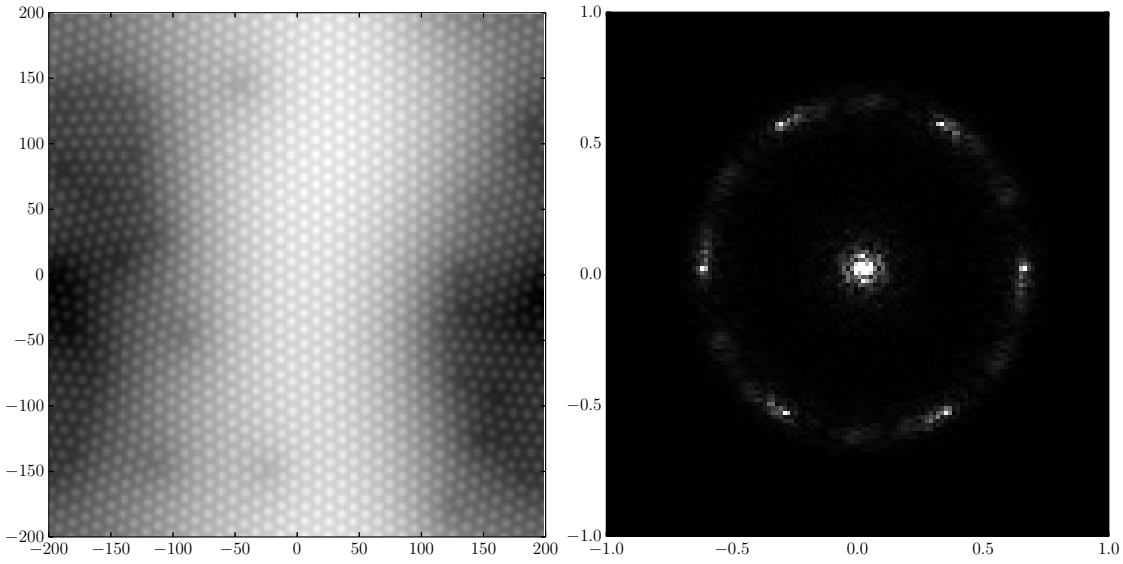

Figure 3.14: Surface height (left) and the magnitude of the Fourier transform (right) after integrating to time $t = 10^4$ with a scratch along $x = 0$ of width $2\sigma = 4$.

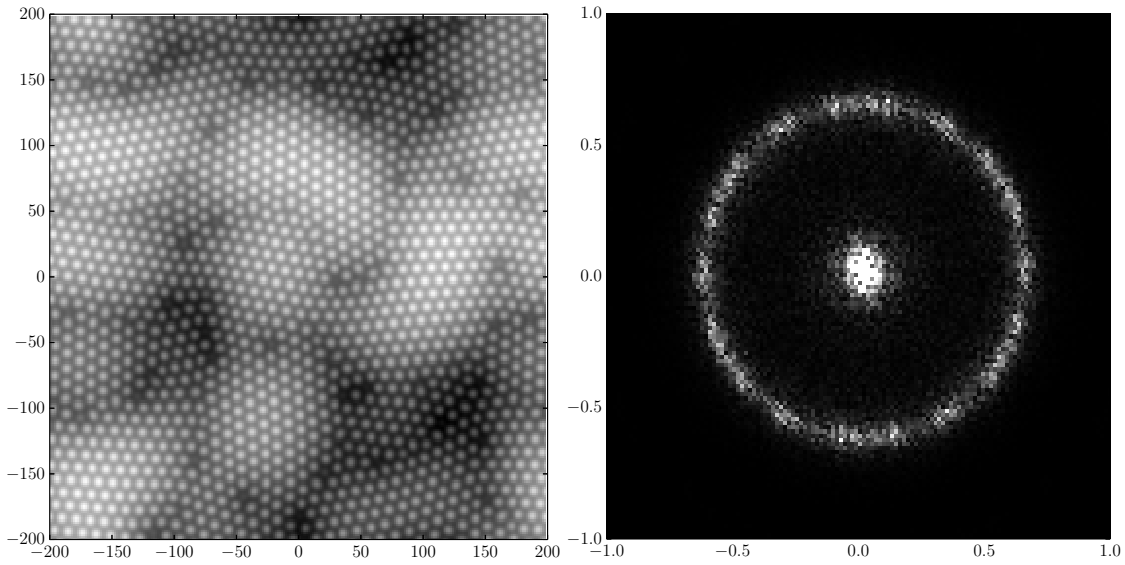

Figure 3.15: Surface height (left) and the magnitude of the Fourier transform (right) after integrating to time $t = 10^4$ with a scratch of width $2\sigma \simeq 13.86$.

From the surface shown in the left panel of Fig. 3.14, it can be seen that, when the improved ordering occurs, it is most dramatic in a strip centered along the initial scratch. To measure this localization of the order quantitatively, we used the persistent homology method of Section 1.5.2 on strips of different widths. The strips were the rectangular regions $(x, y) \in [-w/2, w/2] \times [-L, L]$, where w denotes the strip width. Since changing the strip width also changes the total area over that one is measuring holes, it is more appropriate to calculate the H_1 sum per unit area instead of the raw H_1 sum. The result of this analysis after averaging over 10 simulations each with an initial scratch of width 4 is shown in Fig. 3.17 (left). The result from averaging 10 simulations with scratch width approximately equal to $2\lambda_T$ is shown in Fig. 3.17 (right). Comparing the two plots shows that the scratch of width 4 led to much better order near the initial scratch than when the scratch had the larger width $20.4 \simeq 1.97\lambda_T$. In fact, there is better order for the scratch of width 4 even when the entire domains are compared; this corresponds to the data points for strip width 400.

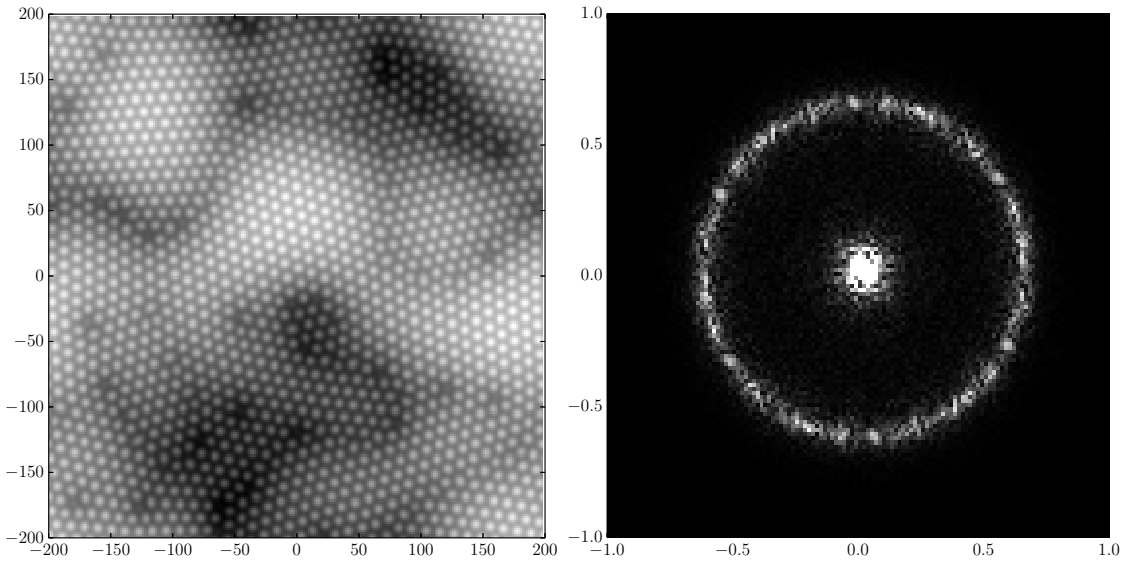

Figure 3.16: Surface height (left) and the magnitude of the Fourier transform (right) after integrating to time $t = 10^4$ with a scratch of width $2\sigma \simeq 20.40$.

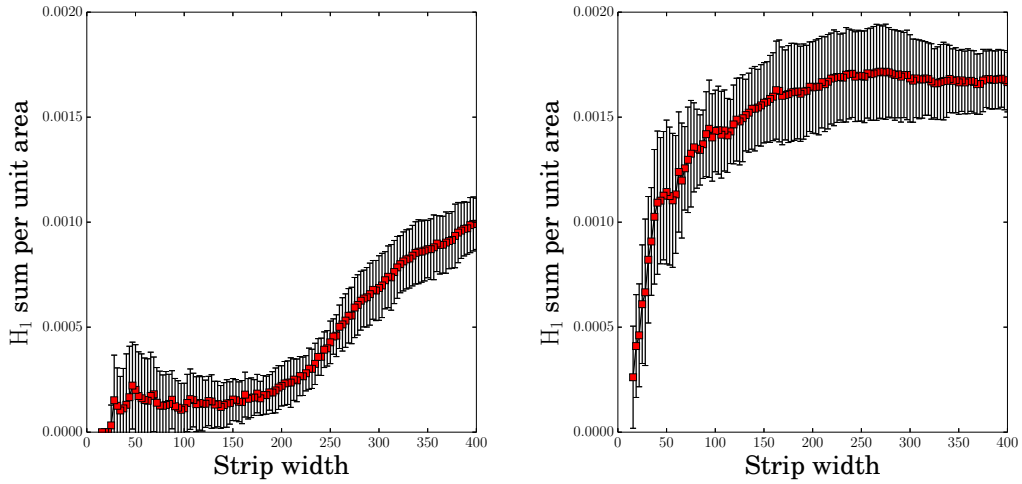

Figure 3.17: The H_1 sum per unit area versus strip width for the initial conditions with a scratch of width 4 (left) and with a scratch of width approximately $2\lambda_T$ (right) after integrating to time $t = 10^4$, averaged over 10 realizations.

3.3 Conclusions

Our simulation results show that templating the surface of a binary material prior to ion bombardment can significantly improve the order of nanoscale patterns produced by sufficiently high ion fluences. When the template amplitude was small (10^{-2}) and the initial wavelengths were approximately one or two times the linearly selected wavelength, the hexagonal and sinusoidal templates both produced dramatically improved global hexagonal order. In particular, the hexagonal templates with initial wavelength approximately double λ_T evolved to a final state that was defect free and nearly perfectly ordered. We demonstrated that longer wavelength sinusoidal templates can lead to substantial improvements in order if the template amplitude is increased. In particular, we showed that sinusoidal templates with wavelength approximately equal to four times the linearly selected wavelength lead to significant enhancements in order if the template amplitude $A_0 \geq 0.4$. Impressive improvements in order were also obtained from the scratched templates when the scratch widths were close to or smaller than the linearly selected wavelength. Moreover, the well-ordered regions of nanodots were centered on the scratches. The results of these simulations with initial scratches demonstrate the potential of using templated samples to produce controllable and localized improvements of the order in nanoscale patterns.

In addition to the positive aspects just discussed, our simulations expose a couple of limitations to the effectiveness of prepatterning. For example, the scratch initial condition has little effect on the surface at long times if the scratch width is significantly larger than the linearly selected wavelength. Additionally, both the templated and scratched surfaces developed an underlying, long-wavelength rolling topography, which could be problematic in some applications.

The prepatterns investigated in this thesis are not just of academic interest; there are also practical methods of producing them. Sinusoidal and hexagonal templates could be produced using standard lithographic methods. Scratches could be produced either by dragging an atomic force microscope tip across a sample [78], or by scanning a laser or focused ion beam across it. These fabrication techniques would not only produce the desired prepatterns, but could produce them at the length scales that our simulations indicate are needed to observe enhanced ordering.

Chapter 4

Summary

In this thesis, we focused on the numerical simulation of two types of topographies that form on solid surfaces subjected to ion bombardment from a broad beam: terraces on elemental surfaces and hexagonally-ordered arrays of nanodots on binary material surfaces. Both of these topographies can be created over large areas on the surface in a single processing step, and so they have considerable potential for applications. For example, terraces can be used to produce both single layer and multilayer diffraction gratings, as was discussed in Refs. [17–19]. On the other hand, the arrays of nanodots with a high degree of hexagonal order could be used for magnetic storage using a technique explored in Refs. [20, 21]. Ion bombardment of binary materials can also lead to the formation of hexagonal arrays of semiconductor quantum dots, as was achieved by Facsko *et al.* – see Ref. [6]

The formation of terraces on elemental solid surfaces exposed to a broad ion beam has been observed in experiments for over four decades [10, 24]. In Chapter 2, we presented the first theory that demonstrates that the combination of sputtering and surface self-diffusion can cause a nominally flat surface evolve into a terraced surface. When we assumed there were no transverse variations in the surface, our equation of motion was the 1+1 dimensional KS equation plus an additional term that was proportional to the slope cubed, see Eq. (2.11). We found that this cubic nonlinearity can lead to terrace formation. We were able to seek traveling wave solutions and transform the equation of motion into an system of three first order ODEs with a single unknown real parameter $s_{\rm tr}$. For a single value $s_{\rm tr} \simeq 2.388$, we numerically found a solution that was a heteroclinic trajectory that connected the selected slopes of the transformed surface. Undoing the transformations allowed us to relate the numerically-determined $s_{\rm tr}$ to the selected slopes, propagation velocity, and overall erosion rate of surface at late times for all values of the coefficients in the equation of motion. In our theory, we found that the abrupt change in the slope in a spatial region connecting the selected terrace slopes is due to the formation of an undercompressive shock. These

undercompressive shocks are nonclassical shocks because they violate the Lax entropy condition Eq. (1.39).

We next extended the numerical analysis of our theory to include transverse variations. The equation of motion we used was the anisotropic KS equation with additional cubic terms, see Eq. (2.2). First, we demonstrated that if the equation of motion was strongly smoothing in the transverse direction, the predictions of the analysis in 1+1 dimensions were still accurate for the terraces that developed. When a transverse instability was present, we found various topographies that are also observed in experiments. For example, we numerically obtained parallel mode terraces that were very similar to those seen by Datta *et al.* [9]. Furthermore, we found elongated pyramidal structures that protrude out of the surface are aligned with the ion beam direction projected onto the surface. These simulated pyramidal structures strongly resemble those seen in experiments by Carter *et al.* [10] and Datta *et al.* [11]. Our simulations also produced lenticular depressions like those seen by Teichmann *et al.* in Ref. [12]. The terraces that formed in our simulations exhibited interrupted coarsening, in agreement with experiments. Hauffe had posited in 1976 that ion reflection was the cause of the coarsening [24]. However, coarsening occurs without any ion reflection in our model. Finally, our theory of terracing is consistent with the experimental observation that terraces often form when the angle of incidence is near grazing.

In Chapter 3, we investigated a practical method of improving the quality of the order of the hexagonal arrays of nanodots that can form on binary material surfaces when ion bombarded at normal incidence. The method was to prepattern the surface with either a sinusoidal template, a hexagonal template, or scratches. We studied the influence of prepatterning by using them as initial conditions for the Bradley-Shipman equations (1.27) and (1.28). The degree of hexagonal order was quantified using a standard method known as the nearest-neighbor number distribution and different method that used persistent homology, an approach in topological data analysis. Using persistent homology, we were able to compute a quantity called the H_1 sum that is zero for a perfectly hexagonal lattice and increases for each defect in an imperfect lattice. We found that using low amplitude (about 10^{-2} times the final pattern amplitude) sinusoidal and hexagonal templates

resulted in dramatic improvements in the degree of hexagonal order at late times if the template wavelength was close to one or two times the linearly selected wavelength. Then we showed that sinusoidal templates of even longer wavelength could also enhance the pattern order if the template amplitude was made larger. Specifically, we demonstrated that sinusoidal templates with amplitudes greater than or equal to 0.4 and wavelength equal to four times the linearly selected wavelength produce hexagonal arrays of nanodots with significantly improved order at late times. We also demonstrated that scratching the surface can produce improved hexagonal order in the vicinity of the scratch if the scratch's width is less than the linearly selected wavelength.

In conclusion, we hope that our theory of terracing and our study of improving the hexagonal order of arrays of nanodots will be useful for understanding and controlling these topographies produced by ion bombardment. It would be exciting to see our results on terracing and prepatterning explored in experiments.

Bibliography

[1] S. Habenicht, W. Bolse, K. P. Lieb, K. Riemann, and U. Geyer, "Nanometer ripple formation and self-affine roughening of ion-beam-eroded graphite surfaces," Phys. Rev. B **60**, R2200 (1999).

[2] D. P. Adams, T. M. Mayer, M. J. Vasile, and K. Archuleta, "Effects of evolving surface morphology on yield during focused ion beam milling of carbon," Appl. Surf. Sci. **252**, 2432 (2006).

[3] P. F. A. Alkemade, "Propulsion of ripples on glass by ion bombardment," Phys. Rev. Lett. **96**, 107602 (2006).

[4] T. Basu, D. P. Datta, and T. Som, "Transition from ripples to faceted structures under low-energy argon ion bombardment of silicon: understanding the role of shadowing and sputtering," Nanoscale Res. Lett. **8**, 289 (2013).

[5] H. Gnaser, "Nanostructures on surfaces by ion irradiation," Pure Appl. Chem. **83**, 2003 (2011).

[6] S. Facsko, T. Dekorsy, C. Koerdt, C. Trappe, H. Kurz, A. Vogt, and H. L. Hartnagel, "Formation of ordered nanoscale semiconductor dots by ion sputtering," Science **285**, 1551 (1999).

[7] F. Frost, A. Schindler, and F. Bigl, "Roughness evolution of ion sputtered rotating inp surfaces: pattern formation and scaling laws," Phys. Rev. Lett. **85**, 4116 (2000).

[8] P. D. Shipman and R. M. Bradley, "Theory of nanoscale pattern formation induced by normal-incidence ion bombardment of binary compounds," Phys. Rev. B **84**, 085420 (2011).

[9] D. P. Datta and T. K. Chini, "Atomic force microscopy study of ar-ion-induced ripple patterns on si(100)," Phys. Rev. B **69**, 235313 (2004).

[10] G. Carter, M. J. Nobes, F. Paton, J. S. Williams, and J. L. Whitton, "Ion bombardment induced ripple topography on amorphous solids," Radiation Effects and Defects in Solids **33**, 65 (1976).

[11] D. P. Datta, S. K. Garg, T. Basu, B. Satpati, H. Höfsass, D. Kanjilal, and T. Som, "Temporal evolution of ge surface topography under kev ion irradiation: Combined effects of curvature-dependent sputter erosion and atomic redistribution," Appl. Surf. Sci. **360**, 131 (2016).

[12] M. Teichmann, J. Lorbeer, F. Frost, and B. Rauschenbach, "Ripple coarsening on ion beam-eroded surfaces," Nanoscale Research Letters **9**, 439 (2014).

[13] H. H. Chen, O. A. Urquidez, S. Ichim, L. H. Rodriquez, M. P. Brenner, and M. J. Aziz, "Shocks in ion sputtering sharpen steep surface features," Science **310**, 294 (2005).

[14] J. Muñoz-García, L. Vázquez, M. Castro, R. Gago, A. Redondo-Cubero, A. Moreno-Barrado, and R. Cuerno, "Self-organized nanopatterning of silicon surfaces by ion beam sputtering," Mater. Sci. Eng. R-Rep. **86**, 224025 (2014).

[15] R. M. Bradley and P. D. Shipman, "Spontaneous pattern formation induced by ion bombardment of binary compounds," Phys. Rev. Lett. **105**, 145501 (2010).

[16] R. M. Bradley and P. D. Shipman, "A surface layer of altered composition can play a key role in nanoscale pattern formation induced by ion bombardment," Appl. Surf. Sci. **258**, 4161 (2012).

[17] M. P. Harrison and R. M. Bradley, "Blazed diffraction gratings produced by ion bombardment of pre-patterned solid surfaces," J. Appl. Phys. **121**, 054308 (2017).

[18] M. P. Harrison and R. M. Bradley, "Fabrication of high quality multilayer blazed gratings using ion beam assisted deposition," J. Appl. Phys. **121**, 225304 (2017).

[19] X. Ou, K.-H. Heinig, R. Hübner, J. Grenzer, a Xi Wang, M. Helm, J. Fassbender, and S. Facsko, "Faceted nanostructure arrays with extreme regularity by self-assembly of vacancies," Nanoscale **7**, 18928 (2015).

[20] T. Bobek, N. Mikuszeit, J. Camarero, S. Kyrsta, L. Yang, M. A. Niño, C. Hofer, L. Gridneva, D. Arvanitis, R. Miranda, J. J. de Miguel, C. Teichert, and H. Kurz, "Self-organized hexagonal patterns of independent magnetic nanodots," Adv. Mater. **19**, 4375 (2007).

[21] C. Teichert, J. J. de Miguel, and T. Bobek, "Ion beam sputtered nanostructured semiconductor surfaces as templates for nanomagnet arrays," J. Phys.: Cond. Matt. **21**, 224025 (2009).

[22] M. A. Makeev, R. Cuerno, and A.-L. Barabási, "Morphology of ion-sputtered surfaces," Nucl. Instrum. Methods Phys. Res., Sect. B **197**, 185 (2002).

[23] M. Navez and C. Sella, "Etude de l'attaque du verre par bombardement ionique," in *Electron Microscopy*, Fifth International Congress for Electron Microscopy, Vol. 2, edited by S. S. B. Jr (Academic Press Inc, New York, USA, 1962) paper C5.

[24] W. Hauffe, "Faceting mechanism in the sputtering process," Phys. Stat. Sol. A **35**, K93 (1976).

[25] D. Flamm, F. Frost, and D. Hirsch, "Evolution of surface topography of fused silica by ion beam sputtering," Appl. Surf. Sci. **179**, 96 (2001).

[26] P. Karmakar and D. Ghose, "Nanoscale periodic and faceted structures formation on si (100) by oblique angle oxygen ion sputtering," Nucl. Inst. Meth. Phys. Res. B **230**, 539 (2005).

[27] Q. Wei, J. Lian, L. A. Boatner, L. M. Wang, and R. C. Ewing, "Propagation of ripples on pyrochlore induced by ion beam bombardment," Phys. Rev. B **80**, 085413 (2009).

[28] P. Mishra and D. Ghose, "Effect of initial target surface roughness on the evolution of ripple topography induced by oxygen sputtering of al films," J. Appl. Phys. **105**, 014304 (2009).

[29] V. J, Z. B, F. F, and Rauschenbach, "Topography evolution mechanism on fused silica during low-energy ion beam sputtering," J. Appl. Phys. **109**, 043501 (2011).

[30] A. Metya, D. Ghose, S. A. Mollick, and A. Majumdar, "Nanopatterning of mica surface under low energy ion beam sputtering," J. Appl. Phys. **111**, 074306 (2012).

[31] M. Teichmann, J. Lorbeer, B. Ziberi, F. Frost, and B. Rauschenbach, "Pattern formation on ge by low energy ion beam erosion," New J. Phys. **15**, 103029 (2013).

[32] D. A. Pearson and R. M. Bradley, "Theory of terraced topographies produced by oblique-incidence ion bombardment of solid surfaces," J. Phys.: Cond. Matt. **27**, 015010 (2015).

[33] R. M. Bradley and J. M. E. Harper, "Theory of ripple topography induced by ion bombardment," J. Vac. Sci. Technol. A **6**, 2390 (1988).

[34] S. Habenicht, K. P. Lieb, J. Koch, and A. D. Wieck, "Ripple propagation and velocity dispersion on ion-beam-eroded silicon surfaces," Phys. Rev. B **65**, 115327 (2002).

[35] W. J. MoberlyChan, "Dual-beam focused ion beam/electron microscopy processing and metrology of redeposition during ionâĂŞsurface 3d interactions, from micromachining to self-organized picostructures," J. Phys.: Condens. Matter **21**, 224013 (2009).

[36] D. Kramczynski, B. Reuscher, and H. Gnaser, "Wavelength-dependent ripple propagation on ion-irradiated prepatterned surfaces driven by viscous flow corroborates two-field continuum model," Phys. Rev. B **89**, 205422 (2014).

[37] P. Sigmund, "Sputtering yield of amorphous and polycrystalline targets," Phys. Rev. **184**, 383 (1969).

[38] G. Hobler, R. M. Bradley, and H. M. Urbassek, "Probing the limitations of sigmund's model of spatially resolved sputtering using monte carlo simulations," Phys. Rev. B **93**, 205443 (2016).

[39] G. Carter, B. Navinsek, and J. L. Whitton, *Sputtering by Particle Bombardment I*, Topics in Applied Physics, Vol. 47 (Springer, Berlin, Germany, 1981) p. 231.

[40] R. Cuerno and A.-L.Barabási, "Dynamic scaling of ion-sputtered surfaces," Phys. Rev. Lett. **74**, 4746 (1995).

[41] W. W. Mullins, "Theory of thermal grooving," Journal of Applied Physics **28**, 333 (1957).

[42] M. Castro, R. Cuerno, L. Vázquez, and R. Gago, "Self-organized ordering of nanostructures produced by ion-beam sputtering," Phys. Rev. Lett. **94**, 016102 (2005).

[43] J. Muñoz-García, M. Castro, and R. Cuerno, "Nonlinear ripple dynamics on amorphous surfaces patterned by ion beam sputtering," Phys. Rev. Lett. **96**, 086101 (2006).

[44] J. Muñoz-García, R. Cuerno, and M. Castro, "Coupling of morphology to surface transport in ion-beam irradiated surfaces: oblique incidence," Phys. Rev. B **78**, 205408 (2008).

[45] V. B. Shenoy, W. L. Chan, and E. Chason, "Compositionally modulated ripples induced by sputtering of alloy surfaces," Phys. Rev. Lett. **98**, 256101 (2007).

[46] M. Cross and H. Greenside, *Pattern Formation and Dynamics in Nonequilibrium Systems* (Cambridge University Press, Cambridge, England, 2009).

[47] R. Hoyle, *Pattern Formation: An Introduction to Methods* (Cambridge University Press, Cambridge, England, 2007).

[48] F. C. Motta, P. D. Shipman, and R. M. Bradley, "Theory of nanoscale pattern formation produced by oblique-incidence ion bombardment of binary compounds," Phys. Rev. B **90**, 085428 (2014).

[49] J. Zhang, Q. Wei, J. Lian, W. Jiang, W. J. Weber, and R. C. Ewing, "Self-assembly of well-aligned 3c-sic ripples by focused ion beam," Appl. Phys. Lett. **92**, 193107 (2008).

[50] G. B. Whitham, *Linear and Nonlinear Waves* (John Wiley & Sons, New York, USA, 1974).

[51] P. G. LeFloch, *Hyperbolic Systems of Conservation Laws: The Theory of Classical and Non-classical Shock Waves* (Birkhäuser, Basel, Switzerland, 2012).

[52] P. Brown, G. Byrne, and A. Hindmarsh, "Vode: a variable-coefficient ode solver," J. Sci. Stat. Comput. **10**, 1038 (1989).

[53] S. M. Cox and P. C. Matthews, "Exponential time differencing for stiff systems," J. Comput. Phys. **176**, 430 (2002).

[54] A.-K. Kassam and L. N. Trefethen, "Fourth-order time-stepping for stiff pdes," J. Sci. Comput. **26**, 1214 (2005).

[55] V. I. Arnold, *Ordinary Differential Equations* (MIT Press, Massachusetts, USA, 1973).

[56] H. Edelsbrunner and J. L. Harer, "Persistent homology – a survey," in *Contemporary Mathematics*, Fifth International Congress for Electron Microscopy, Vol. 453, edited by J. E. Goodman, J. Pach, and R. Pollack (American Mathematical Society, Rhode Island, USA, 2008).

[57] F. C. Motta, R. Neville, P. D. Shipman, D. A. Pearson, and R. M. Bradley, Physica D , (submitted) (2018).

[58] A. Tausz, "phom: Persistent homology in r," https://github.com/cran/phom (2012), gitHub Repository.

[59] M. Engler, S. Macko, F. Frost, and T. Michely, "Evolution of ion beam induced patterns on si (001)," Phys. Rev. B **89**, 245412 (2014).

[60] M. Rost and J. Krug, "Anisotropic kuramoto-sivashinsky equation for surface growth and erosion," Phys. Rev. Lett. **75**, 3894 (1995).

[61] G. Carter and V. Vishnyakov, "Roughening and ripple instabilities on ion-bombarded si," Phys. Rev. B **54**, 17647 (1996).

[62] M. Moseler, P. Gumbsch, C. Casiraghi, A. C. Ferrari, and J. Robertson, "The ultrasmoothness of diamond-like carbon surfaces," Science **309**, 1545 (2005).

[63] B. Davidovitch, M. J. Aziz, and M. P. Brenner, "On the stabilization of ion sputtered surfaces," Phys. Rev. B **76**, 205420 (2007).

[64] C. C. Umbach, R. L. Headrick, and K. C. Chang, "Spontaneous nanoscale corrugation of ion-eroded sio2: The role of ion-irradiation-enhanced viscous flow," Phys. Rev. Lett. **87**, 246104 (2001).

[65] R. M. Bradley and H. Hofsáss, "Nanoscale patterns produced by self-sputtering of solid surfaces: The effect of ion implantation," J. Appl. Phys. **120**, 074302 (2016).

[66] T. Kawahara, "Formation of saturated solitons in a nonlinear dispersive system with instability and dissipation," Phys. Rev. Lett. **51**, 381 (1983).

[67] M. P. Gelfand and R. M. Bradley, "One dimensional conservative surface dynamics with broken parity: Arrested collapse versus coarsening," J. Appl. Phys. **379**, 199 (2015).

[68] C. S. Madi, E. Anzenberg, K. F. L. Jr., and M. J. Aziz, Phys. Rev. Lett. **106**, 066101 (2011).

[69] E. Burman and A. Ern, "Discrete maximum principle for galerkin approximations of the laplace operator on arbitrary meshes," C. R. Acad. Sci. Paris **338**, 641 (2004).

[70] H. Hofsäss, K. Zhang, H. G. Gehrke, and C. Brüsewitz, "Propagation of ripple patterns on si during ion bombardment," Phys. Rev. B **88**, 075426 (2013).

[71] M. Holmes-Cerfon, W. Zhou, A. L. Bertozzi, M. P. Brenner, and M. J. Aziz, "Development of knife-edge ridges on ion-bombarded surfaces," Appl. Phys. Lett. **101**, 143109 (2012).

[72] M. Holmes-Cerfon, M. J. Aziz, and M. P. Brenner, "Creating sharp features by colliding shocks on uniformly irradiated surfaces," Phys. Rev. B **85**, 165441 (2012).

[73] A. Cuenat, B. H. George, K.-C. Chang, J. M. Blakely, and M. J. Aziz, "Lateral templating for guided self-organization of sputter morphologies," Adv. Materials **17**, 2845 (2005).

[74] P. S. Raman, K. Nair, M. Kamruddin, A. Tyagi, A. Rath, P. Satyam, B. Panigrahi, and V. Ravichandran, "Mev au^{2+} ions induced surface patterning in silica," Appl. Surf. Sci. **258**, 4156 (2012).

[75] M. Joe, J.-H. Kim, C. Choi, B. Kahng, and J.-S. Kim, "Nanopatterning by multiple-ion-beam sputtering," J. Phys.: Condens. Matter **21**, 224011 (2009).

[76] J.-H. Kim, N.-B. Ha, J.-S. Kim, M. Joe, K.-R. Lee, and R. Cuerno, "One-dimensional pattern of au nanodots by ion-beam sputtering: formation and mechanism," Nanotechnology **22**, 285301 (2011).

[77] J.-H. Kim, J.-S. Kim, J. Muñoz-García, and R. Cuerno, "Role of nonlinearities and initial prepatterned surfaces in nanobead formation by ion-beam bombardment of au (001): Experiments and theory," Phys. Rev. B **87**, 085438 (2013).

[78] A. A. Tseng, C.-F. J. Kuo, S. Jou, S. Nishimura, and J. Shirakashi, "Scratch direction and threshold force in nanoscale scratching using atomic force microscopes," Appl. Surf. Sci. **257**, 9243 (2011).